

## A DETAILED STUDY OF THE LOBES OF ELEVEN POWERFUL RADIO GALAXIES

RUTH A. DALY<sup>1</sup>, PREETI KHARB<sup>2</sup>, CHRISTOPHER P. O’DEA<sup>2</sup>, STEFI A. BAUM<sup>3</sup>, MATTHEW P. MORY<sup>1</sup>, JUSTIN MCKANE<sup>1</sup>,  
CHRISTOPHER ALTENDERFER<sup>1</sup>, AND MICHAEL BEURY<sup>1</sup>

<sup>1</sup> Department of Physics, Penn State University, Berks Campus, Reading, PA, USA

<sup>2</sup> Department of Physics, Rochester Institute of Technology, Rochester, NY, USA

<sup>3</sup> Center for Imaging Science, Rochester Institute of Technology, Rochester, NY, USA

Received 2009 September 18; accepted 2009 December 18; published 2010 February 19

### ABSTRACT

Radio lobes of a sample of 11 very powerful classical double radio galaxies were studied. Each source was rotated so that the symmetry axis of the source was horizontal, and vertical cross-sectional cuts were taken across the source at intervals of one beam size. These were used to study the cross-sectional surface brightness profiles, the width of each slice, radio emissivity as a function of position across each slice, the first and second moments, and the average surface brightness, minimum-energy magnetic field strength, and pressure of each slice. Typically, a Gaussian provides a good description of the surface brightness profile of cross-sectional slices. The Gaussian full width at half-maximum (FWHM) as a function of distance from the hot spot first increases and then decreases with increasing distance from the hot spot. The width as a function of distance from the hot spot is generally highly symmetric on each side of the source. The radio emissivity is often close to flat across a slice, indicating a roughly constant emissivity and pressure for that slice. Some slices show variations in radio emissivity that indicate an “edge-peaked” pressure profile for that slice. When this occurs, it is generally found in slices near the local maxima of the bridge width. The emissivity does not exhibit any signature of emission from a jet. The first moment is generally quite close to zero indicating only small excursions of the ridgeline from the symmetry axis of the source. The second moment indicates the same source shape as is found using the Gaussian FWHM. The average surface brightness is peaked at the hot spot, and is fairly flat across most of the radio lobes. The average magnetic field strength and pressure peak at the hot spot and gradually decrease with increasing distance from the hot spot, reaching a roughly constant value at a location that is typically just before the location of a local maximum of the bridge width. These results are interpreted in terms of a heuristic model for the radio lobes.

*Key words:* galaxies: active – galaxies: general – galaxies: jets – radio continuum: galaxies

### 1. INTRODUCTION

Physical processes in powerful active galactic nuclei (AGNs) with radio jets that appear to be transporting plasma from the galactic nucleus to the intergalactic medium are not completely understood. An understanding of these processes can provide powerful insights into galactic nuclei and the medium through which the jets traverse. Comprehensive spectral studies of the Fanaroff–Riley-type-II (FR II) radio galaxies (Fanaroff & Riley 1974), have indicated that the charged particles/electrons are injected into the terminal regions of the jets called hot spots, which expand to form radio lobes consistent with the spectral index steepening that is observed in the FR II radio lobes (for example, Myers & Spangler 1985; Alexander 1987; Alexander & Leahy 1987; Leahy et al. 1989; Carilli et al. 1991; Liu et al. 1992; Mack et al. 1998; Parma et al. 1999; Murgia et al. 1999; Blundell et al. 1999; Kaiser 2000; Guerra et al. 2000; Goodlet et al. 2004; Machalski et al. 2007; Jamrozny et al. 2008; Kharb et al. 2008; Konar et al. 2009).

A detailed study of the radio bridge in the nearby powerful FR II radio galaxy, Cygnus A, was presented by Carvalho et al. (2005). This study showed that the observed surface brightness distribution perpendicular to the source axis is well characterized by a Gaussian function over most of the length of the source. The first moment of the cross-sectional surface brightness profiles traces the wobbling of the ridgeline, which could be the result of the wobbling of the outflow axis, while the Gaussian full width at half-maximum (FWHM) provides a reasonable estimate of the bridge width. The ratio of

the Gaussian FWHM to the second moment is fairly constant along the source, with an average value of about 2.5, indicating that both these parameters give a consistent measure of the bridge width. The observed surface brightness, estimated minimum pressure, and magnetic field strength decrease with distance from the hot spot. In this paper, we present a similar study on a sample of 11 large and powerful FR II radio galaxies.

The 11 sources studied here are part of a sample of 13 FR II radio galaxies which were observed with multiple configurations of the Very Large Array (VLA) at 330 MHz, 1.4, 5, and 8 GHz. The first results from this sample were presented by Kharb et al. (2008). The sources had arm-length ratios close to unity, small misalignment angles, and weak or no radio jets, all of which are consistent with the sources lying close to the plane of the sky. The results from the spectral aging analysis of this radio galaxy sample are presented by O’Dea et al. (2009), while the cosmological results are presented by Daly et al. (2008, 2009). The 11 sources of interest here are the ones that showed extended lobe emission. Extended radio lobes were not detected for the two most distant sources, 3C13 and 3C470. The 11 FR II radio galaxies studied here have radio luminosities at 178 MHz greater than  $10^{28}$  W Hz<sup>-1</sup>, angular sizes larger than 27”, and span a redshift range of  $z \simeq 0.4$ –1.3. A spatially flat cosmological model with current normalized mean mass density  $\Omega_m = 0.3$ , cosmological constant  $\Omega_\Lambda = 0.7$ , and Hubble constant  $H_0 = 70$  km s<sup>-1</sup> Mpc<sup>-1</sup> are assumed throughout. The analysis and results are presented in Section 2, and a summary and conclusions are given in Section 3.

**Table 1**  
Normalizations for Figures

(1)	(2)	(3)	(4)	(5)	(6)	(7)	(8)	(9)
Source	$\theta_{\text{FWHM}}$ (arcsec)	$z$	( $a_0 r$ ) (Gpc)	$K_\epsilon$ ( $10^{-34} \text{ erg s}^{-1} \text{ cm}^{-3} \text{ Hz}^{-1}$ )	$K_B(1.4)$ ( $10^{-6} \text{ G}$ )	$K_B(5)$ ( $10^{-6} \text{ G}$ )	$K_P(1.4)$ ( $10^{-11} \text{ erg cm}^{-3}$ )	$K_P(5)$ ( $10^{-11} \text{ erg cm}^{-3}$ )
3C6.1	2	0.8404	2.896	3.14	107	138	35.2	58.5
3C34	2	0.69	2.476	2.61	99.5	128	30.6	50.9
3C41	2	0.794	2.771	2.96	104	135	33.7	56.0
3C44	2.5	0.66	2.388	1.61	86.4	111	23.1	38.4
3C54	2.5	0.8274	2.862	1.97	93.3	120	26.9	44.8
3C114	2.5	0.815	2.828	1.94	92.8	120	26.6	44.3
3C142.1	2	0.4061	1.573	1.97	88.5	114	24.2	40.3
3C169.1	2.5	0.633	2.307	1.56	85.4	110	22.5	37.5
3C172	2.5	0.5191	1.951	1.38	81.3	105	20.4	34.0
3C441	2.5	0.707	2.526	1.70	88.3	114	24.1	40.1
3C469.1	2.5	1.336	4.047	3.73	118	152	42.7	71.1

**Notes.** Column 1: source name; Column 2: FWHM of the Gaussian observing beam; Column 3: source redshift; Column 4: coordinate distance to the source in Gigaparsecs; Column 5: normalization to the emissivities  $\epsilon_M$  shown in figures when  $\epsilon_M$  is in units of  $\text{Jy} (\text{beam arcsec})^{-1}$ , as is the case for all of the sources shown here; Column 6: normalization to the 1.4 GHz magnetic field strengths shown in the figures; Column 7: normalization to the 5 GHz magnetic field strengths shown in the figures; Column 8: normalization to the 1.4 GHz pressures shown in the figures; Column 9: normalization to the 5 GHz pressures shown in the figures.

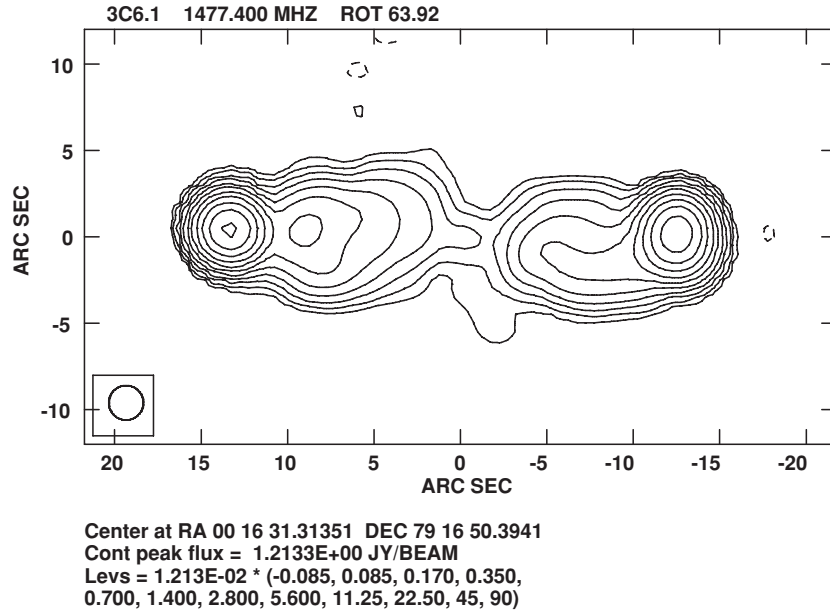


**Figure 1.** 3C6.1 at 1.4 GHz and  $2''$  resolution rotated by  $63^\circ 92'$  counterclockwise so that the centroids of the two hot spots lie on a horizontal line. The location of the core of the source, identified as described in Kharb et al. (2008), has  $x$  and  $y$  coordinates of  $0''$ . Only data with SN greater than  $(\text{mean} + 3 \times \text{rms})$  noise level of the map were included in the source analysis; all of the results presented here were obtained from this image and a similar image at 5 GHz.

## 2. DATA ANALYSIS AND RESULTS

The very powerful FR II radio galaxies were observed with the A-, B-, C-, and D-array configurations of the VLA (Napier et al. 1983) between 2002 November and 2003 November at 330 MHz, 1.4, 4.8, and 8.4 GHz. Details of the data reduction and analysis are presented by Kharb et al. (2008).

The Astronomical Image Processing System (AIPS) along with auxiliary programs were used to obtain and study cross-sectional slices of the radio surface brightness at evenly spaced intervals along the symmetry axis of each radio bridge. The FITS files of the final 1.4 GHz and 5 GHz maps convolved with a  $2''$  or  $2''.5$  beam were rotated so that the hot spots identified using the 8.4 GHz data lay on a horizontal line. The axis joining the two primary hot spots, with each hot spot located at the extremity of each side of the source, was taken to be the symmetry axis of the

source. This seemed a good choice since the sources have very small misalignment angles (Kharb et al. 2008), and is confirmed by the fact that the first moment shows very mild departures from zero across most sources. The data were clipped so as to include only data with an intensity greater than the  $(\text{mean} + 3 \times \text{rms})$  noise level of each map. Cross-sectional slices of the source, separated by one FWHM of the beam, were obtained for each side of each source with the requirement that one of the slices intersect the middle of the primary hot spot on that side of the source. The center of the source was taken to be the core position identified by Kharb et al. (2008). The properties of the cross-sectional slices were used to study the cross-sectional shape of the surface brightness profile (see Section 2.1), the radio emissivity profile of the slice (see Section 2.2), the first and second moments of the slice and a comparison of the second moment with the Gaussian FWHM (see Sections 2.3 and 2.4),

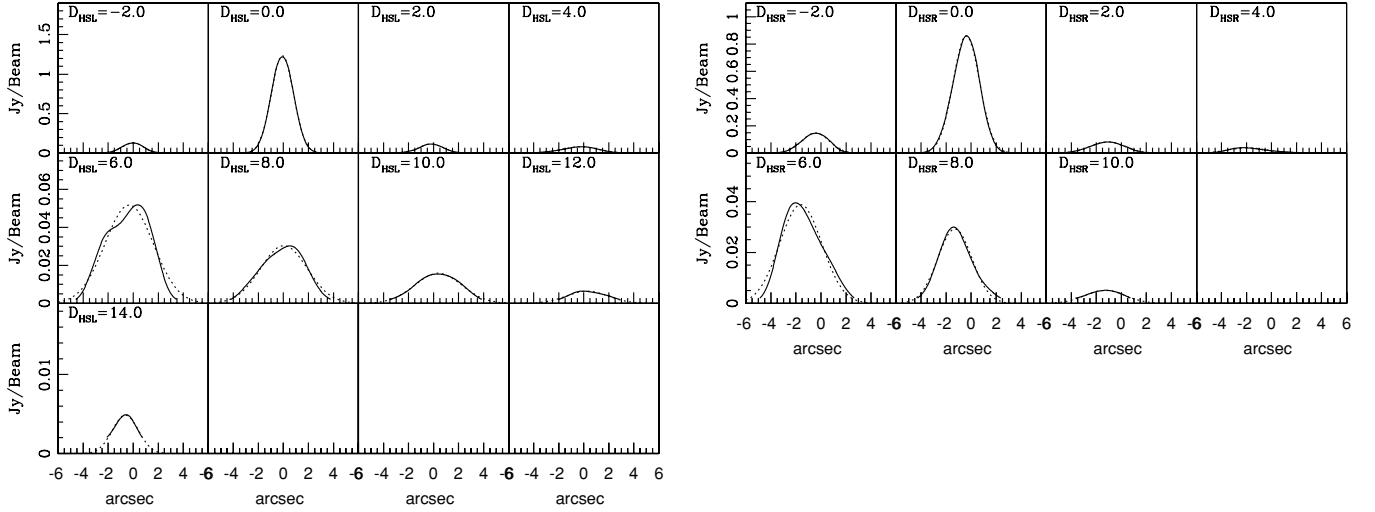


**Figure 2.** 3C6.1 surface brightness (solid line) and best-fit Gaussian (dotted line) for each cross-sectional slice of the radio bridge at 1.4 GHz for the left-hand side of the source (left panel) and the right-hand side of the source (right panel). The distance from the hot spot is indicated in the top left-hand corner of each slide;  $D_{\text{HSL}}$  indicates the distance from the left hot spot, and  $D_{\text{HSR}}$  indicates the distance from the right hot spot, where the left- and right-hand sides of the source are identified relative to the core (see Figure 1). The results indicate that a Gaussian provides an excellent description of the surface brightness profile of each cross-sectional slice. Note that the surface brightness scale of each row is different.

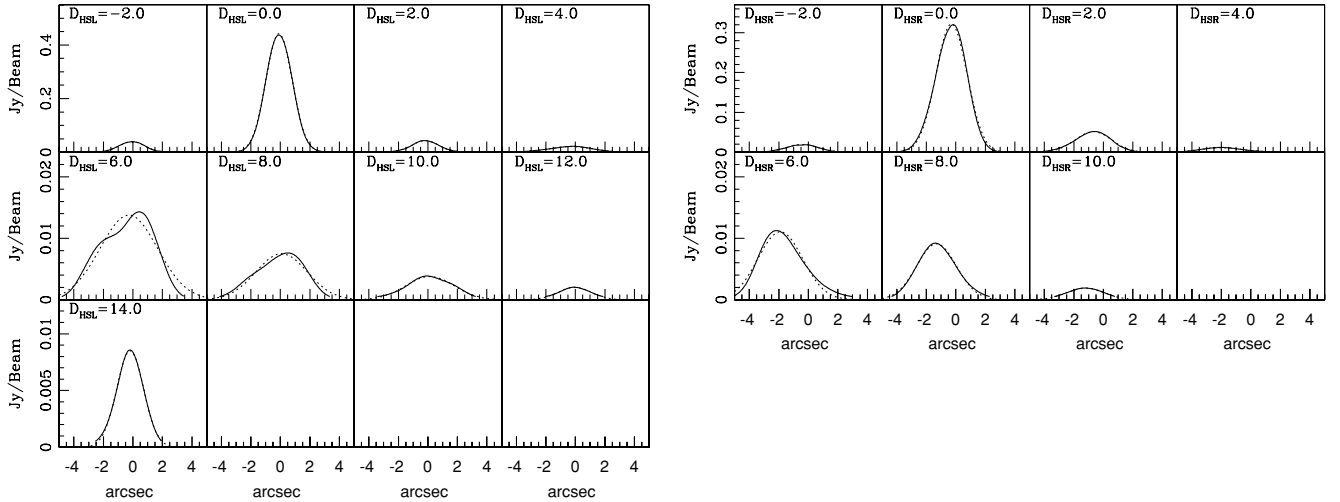


**Figure 3.** 3C6.1 surface brightness (solid line) and best-fit Gaussian (dotted line) for each cross-sectional slice of the radio bridge at 5 GHz for the left-hand side of the source (left panel) and the right-hand side of the source (right panel), as in Figure 2 but at 5 GHz. The results are very similar to those obtained at 1.4 GHz.

and the average surface brightness, minimum-energy magnetic field strength, and average minimum-energy pressure of the plasma in each slice (see Section 2.5).

### 2.1. Cross-sectional Slices and Gaussian Fits

The rotated 1.4 GHz map is shown for each source (see Figures 1–136). Each side of each source is studied separately, and is sliced in the vertical direction, perpendicular to the symmetry axis of the source. Distances (in arcseconds) are measured relative to the hot spot;  $D_{\text{HSL}}$  refers to the distance along the symmetry axis of the source from the left hot spot going toward the center of the source, and  $D_{\text{HSR}}$  refers to that from the right hot spot of the rotated map toward the center of the source.

Each of the cross-sectional surface brightness profiles is fit with a Gaussian. These profiles and the best-fit Gaussian for each is shown in the figures. The FWHM of the best-fit Gaussian,  $W_{\text{Gauss}}$ , is also shown for each slice of each source. These are obtained by subtracting the FWHM of the observing beam in

quadrature:  $W_{\text{Gauss}} = [(W_{\text{G,M}})^2 - (\theta_{\text{FW}})^2]^{1/2}$ , where  $W_{\text{G,M}}$  is the measured FWHM of the Gaussian and  $\theta_{\text{FW}}$  is the FWHM of the observing beam.

Considering the regions of the source with widths indicating a size larger than the beam size, a Gaussian typically provides a very good fit to the cross-sectional surface brightness profiles. The 1.4 and 5 GHz Gaussian widths are in very good agreement. The degree of symmetry of the source width as a function of position is noted in the figure captions. Many of the sources show a remarkable degree of symmetry of source width as a function of distance from the hot spot between the right- and left-hand sides of the source. This suggests that the properties of the ambient medium vary in the same way with distance from the center of the source on each side of the source, and that the beam power of the twin jets is similar at any given time. The widths obtained at 1.4 and 5 GHz are very similar, as expected.

In many of the sources, the bridge width initially increases with distance from the hot spot, and then decreases. Considering

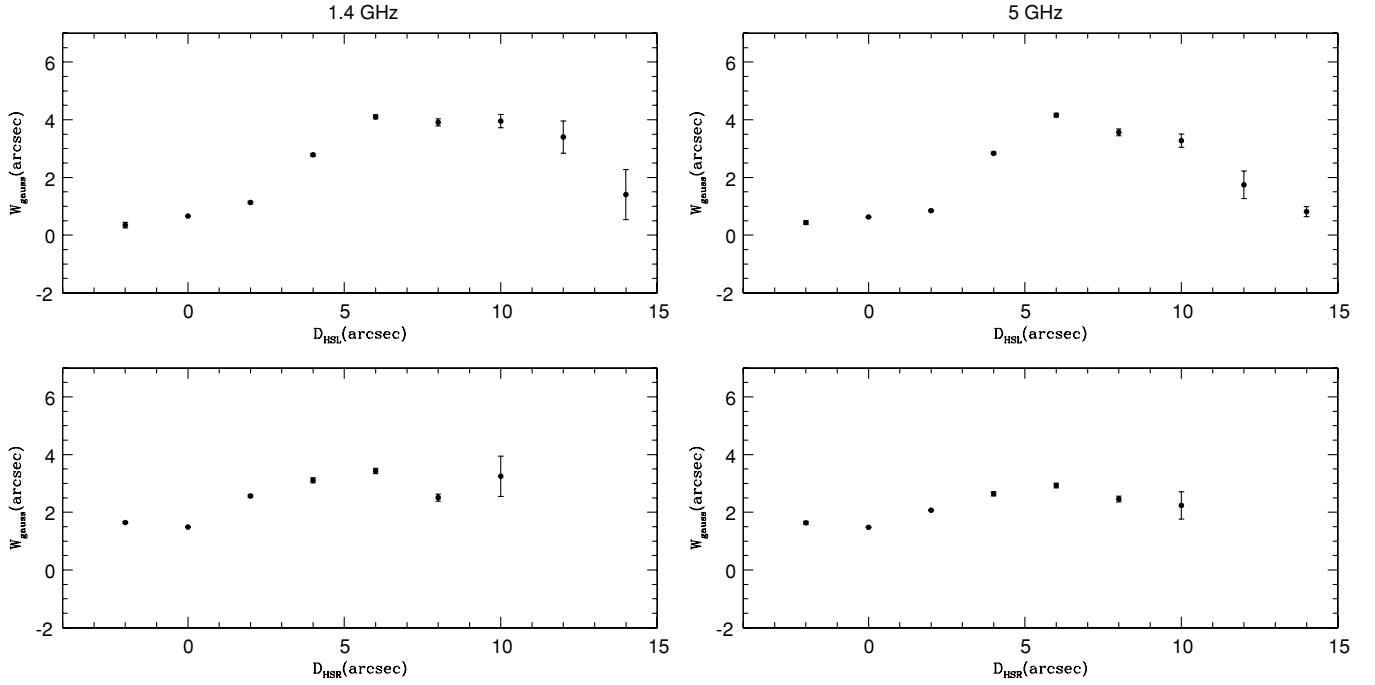


**Figure 4.** 3C6.1 Gaussian FWHM as a function of distance from the hot spot at 1.4 GHz and 5 GHz (left and right panels, respectively) for the left- and right-hand sides of the source (top and bottom panels, respectively) with one measurement shown per  $2''$  resolution element; angular distances are measured from the centroid of the hot spot. This measure of the source width indicates that the right- and left-hand sides of the source are highly symmetric in terms of width as a function of distance from the hot spot. Very similar results are obtained at 1.4 and 5 GHz.

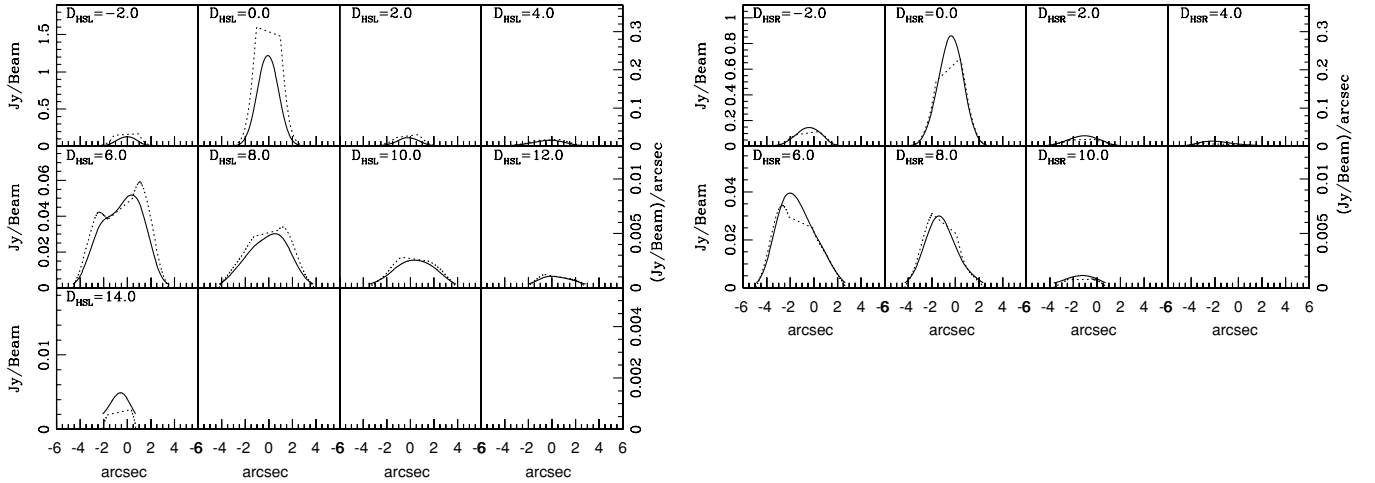


**Figure 5.** 3C6.1 emissivity (dotted line) and surface brightness (solid line) for each cross-sectional slice of the radio bridge at 1.4 GHz for the left-hand side of the source (left panel) and the right-hand side of the source (right panel). The distance from the hot spot is indicated in the top left-hand corner of each slide;  $D_{HSL}$  indicates the distance from the left hot spot, and  $D_{HSR}$  indicates the distance from the right hot spot, where the left- and right-hand sides of the source are identified relative to the core (see Figure 1). The units of surface brightness are shown on the left-hand side of each figure, while those for the emissivity are shown on the right-hand side of each figure. The normalization of the emissivity is given in Table 1. The results indicate that a constant emissivity per slice provides a reasonable description of the source. Note that the surface brightness and emissivity scales of each row are different.

the 22 radio bridges studied here (two for each of the 11 sources), this behavior is clearly seen in 16 bridges (the left side of 3C6.1; 3C34; the 5 GHz data of 3C44; 3C54; the right side of 3C114; 3C142.1; 3C172; 3C441; and 3C469.1), and is consistent with the properties of four more bridges (the right side of 3C6.1; the left side of 3C114; and 3C169.1). Interestingly, the similarity of the source width as a function of distance from the hot spot for the right and left sides of a source typically includes the location of the local maxima of the bridge width. There is only one source, 3C41, that has a width as a function of position that seems to level off. One possible explanation for the turnover of

the bridge width as a function of distance from the hot spot is discussed in Section 2.2.

## 2.2. Radio Emissivity

The emissivity, or energy emitted per unit volume per unit time per unit frequency, can be obtained from the surface brightness profiles, as described in detail in Section 2.5 of Carvalho et al. (2005). For a given surface brightness profile, the emissivity can be obtained as a function of distance from the symmetry axis of the source assuming only that the emissivity is semi-cylindrically symmetric, that is, it is cylindrically

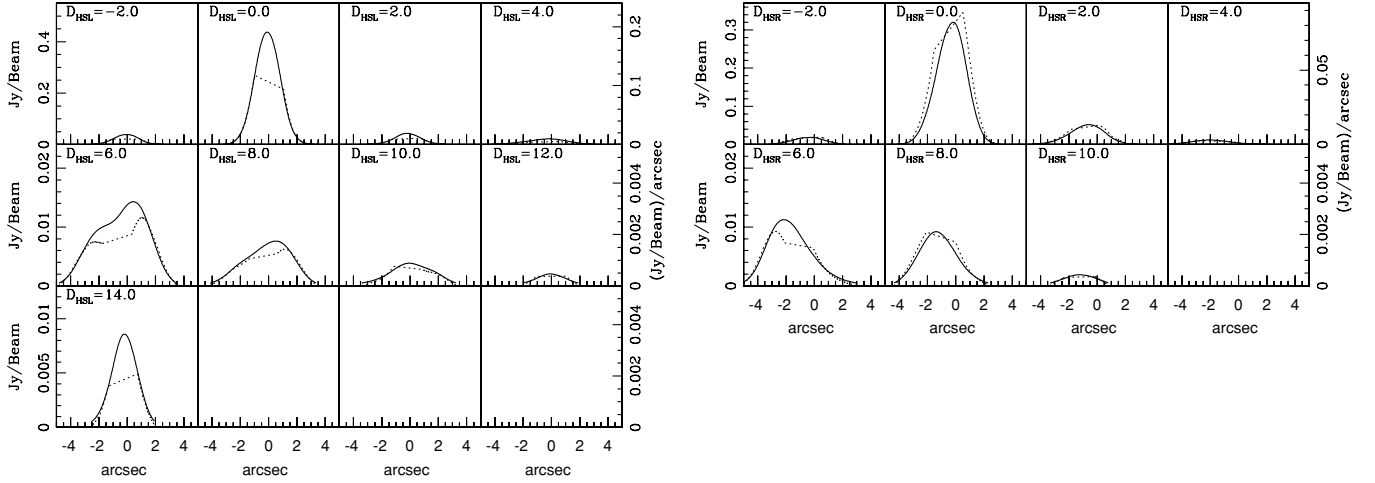


**Figure 6.** 3C6.1 emissivity (dotted line) and surface brightness (solid line) for each cross-sectional slice of the radio bridge at 5 GHz for the left-hand side of the source (left panel) and the right-hand side of the source (right panel), as in Figure 5 but at 5 GHz. The results are very similar to those obtained at 1.4 GHz.

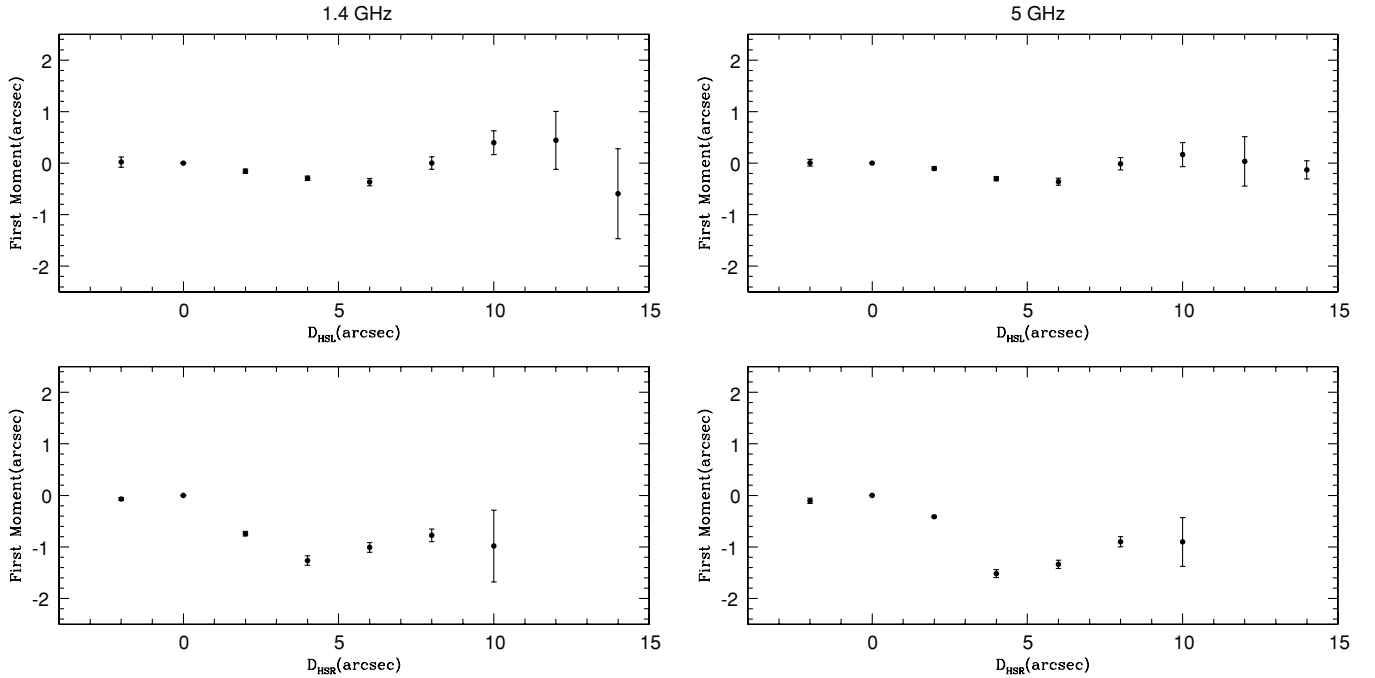


**Figure 7.** 3C6.1 first moment as a function of distance from the hot spot for 1.4 and 5 GHz (left and right panels, respectively) for the left- and right-hand sides of the source (top and bottom panels, respectively), as in Figure 4. The first moment is measured relative to the horizontal line that connects the two hot spot centroids; a value of zero for the first moment means that the first moment lies along the horizontal line connecting the two hot spots. Results obtained at 1.4 and 5 GHz are nearly identical. The left-hand side of the source has a first moment that remains close to zero, while the first moment of the right-hand side of the source falls slightly below this line by about  $1''$ – $2''$  (see Figure 1).

symmetric over each half of the slice (that above the symmetry axis, and that below the symmetry axis) separately. So the emissivity is a free function of distance from the symmetry axis of the source but the emissivity at a given distance  $r$  is assumed to be cylindrically symmetric at that distance  $r$  over that half of the slice (see Figure 14 of Carvalho et al. 2005). The emissivities thus obtained are shown with the surface brightness profiles from which they are obtained in the figures. The emissivities are computed from the outside of the slice toward the slice center, starting from each of the two extremities of the cross-sectional slice. When the emissivity obtained at the center of the slice is continuous, it indicates that the emissivity computed by stepping in from one side of the slice matches that obtained by stepping in from the other side of the slice, suggesting that

in these cases the assumption of semi-cylindrical symmetry is a valid assumption.

The emissivity  $\epsilon_\nu \equiv dE/(dV dt d\nu)$  is related to that measured directly from the radio map, referred to as  $\epsilon_M$ , and a normalization factor  $K_\epsilon$ :  $\epsilon_\nu = K_\epsilon \epsilon_M$ . When the measured value,  $\epsilon_M$ , has units of  $\text{Jy} (\text{beam arcsec})^{-1}$ , as it does for the sources studied here, the normalization factor is  $K_\epsilon = 3.17(1+z)^4 [(a_0 r)/\text{Gpc}]^{-1} (\theta_{\text{FW}}/\text{arcsec})^{-2} 10^{-34} \text{erg cm}^{-3} \text{s}^{-1} \text{Hz}^{-1}$ , where  $a_0 r$  is the coordinate distance to the source, and  $\theta_{\text{FW}}$  is the FWHM of the observing beam. This follows from the following considerations: the emission coefficient  $j_\nu = \epsilon_\nu/(4\pi)$  and the specific intensity produced over a path length  $\Delta y$  is  $I_\nu = j_\nu \Delta y$ , where  $I_\nu = dE/(dA dt d\nu d\Omega)$ , where  $d\Omega$  is a differential solid angle. The observed specific intensity is  $I_{\nu_0} = I_\nu (1+z)^{-3}$

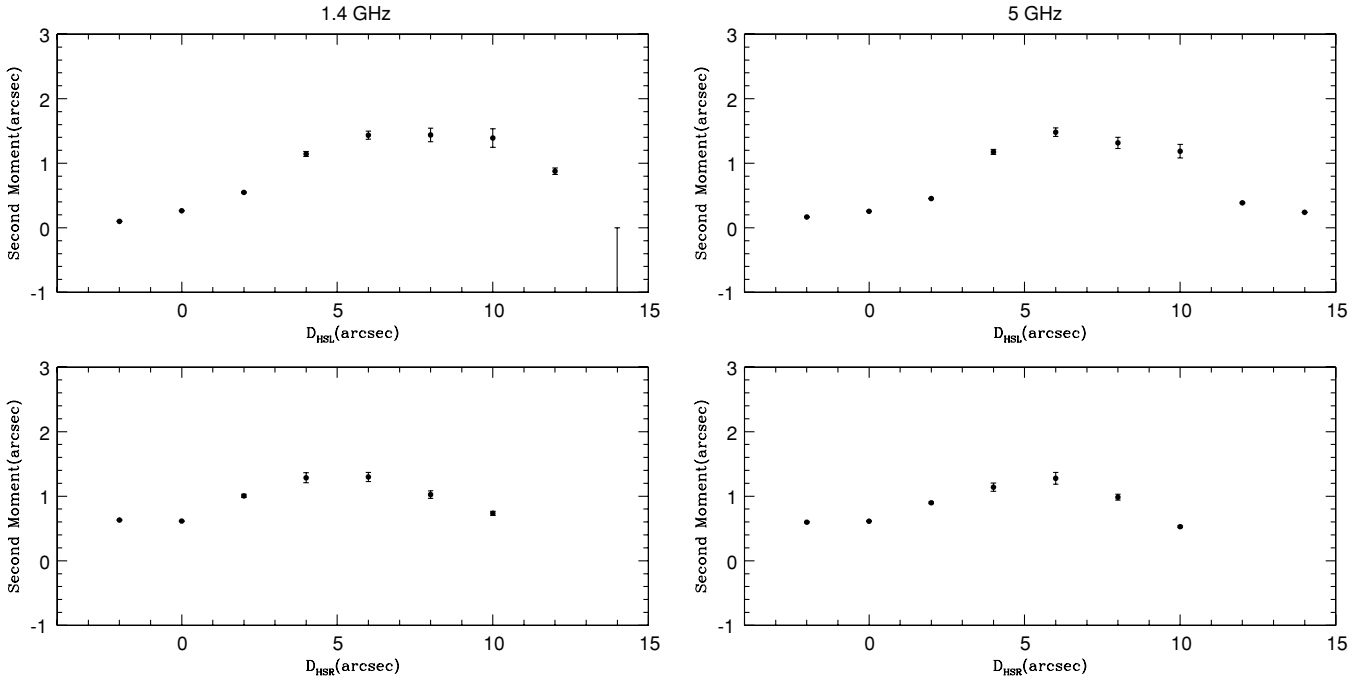


**Figure 8.** 3C6.1 second moment as a function of distance from the hot spot at 1.4 and 5 GHz (left and right panels, respectively) for the left- and right-hand sides of the source (top and bottom panels, respectively), as in Figure 4. Comparing the two panels on the left, it is clear that the source is highly symmetric in terms of the source width as a function of distance from the hot spot. Results obtained at 1.4 and 5 GHz are nearly identical.

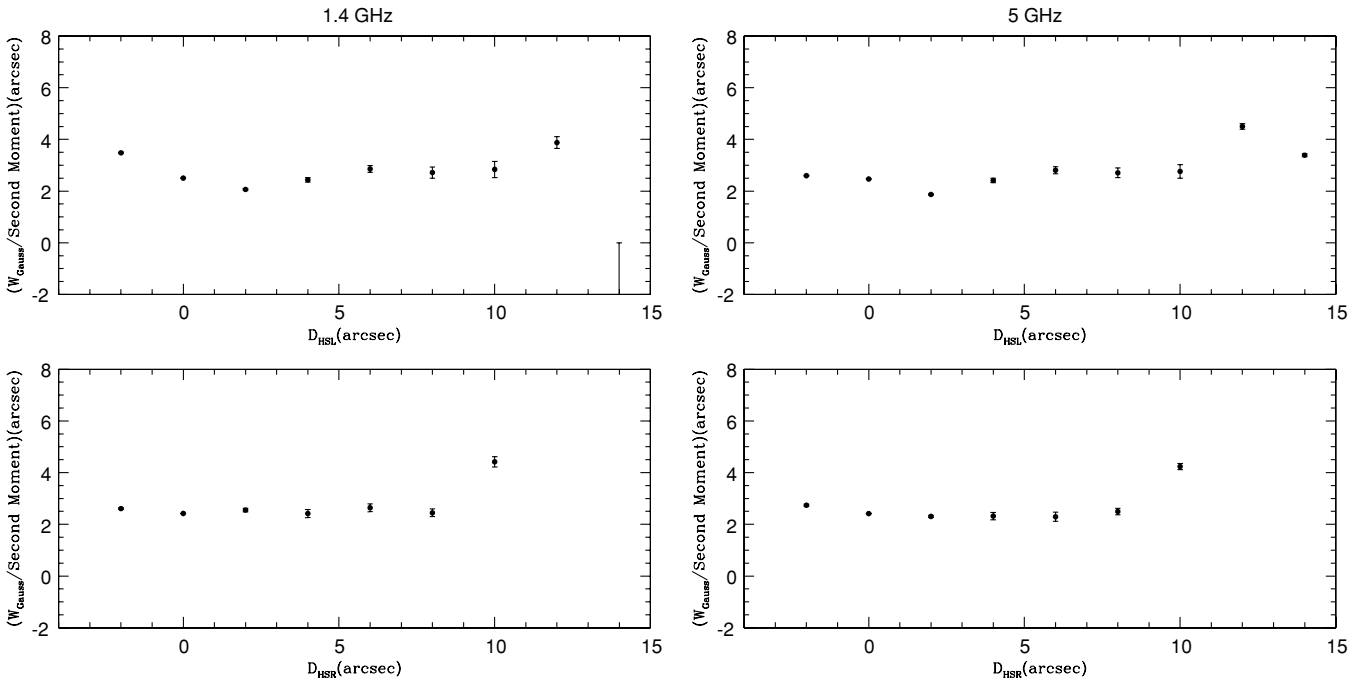


**Figure 9.** 3C6.1 ratio of the Gaussian FWHM to the second moment as a function of distance from the hot spot at 1.4 and 5 GHz (left and right panels, respectively) for the left- and right-hand sides of the source (top and bottom panels, respectively), as in Figure 4. The value of this ratio is fairly constant for each side of the source, and has a value of about 2.5–3. Similar results are obtained at 1.4 and 5 GHz.

and in this study is measured in  $\text{Jy beam}^{-1}$ . To convert this to Jy per steradian it must be multiplied by  $(\pi\theta_b^2)^{-1}$ , where  $\theta_b = \theta_{\text{FW}}/[2\sqrt{\ln 2}]$ .

Each emissivity figure lists the surface brightness units on the left-hand side of the figure, and the emissivity units,  $\epsilon_M$  in  $\text{Jy (beam arcsec)}^{-1}$ , on the right-hand side of the figure. The value of the normalization  $K_\epsilon$  for each source is listed in Table 1 for  $\epsilon_M$  in units of  $\text{Jy (beam arcsec)}^{-1}$ , and the value of  $\epsilon_\nu$  is obtained

using the expression  $\epsilon_\nu = K_\epsilon \epsilon_M$ . Because the resolution for each source is the same at the two frequencies considered, the normalization factor is frequency independent.

The sources have emissivity profiles that are consistent with a roughly constant emissivity in each cross-sectional slice for most slices of a source, that is, the emissivity across the slice is fairly flat. In addition, in most slices of most sources, the emissivity obtained near the center of the slice is continuous.

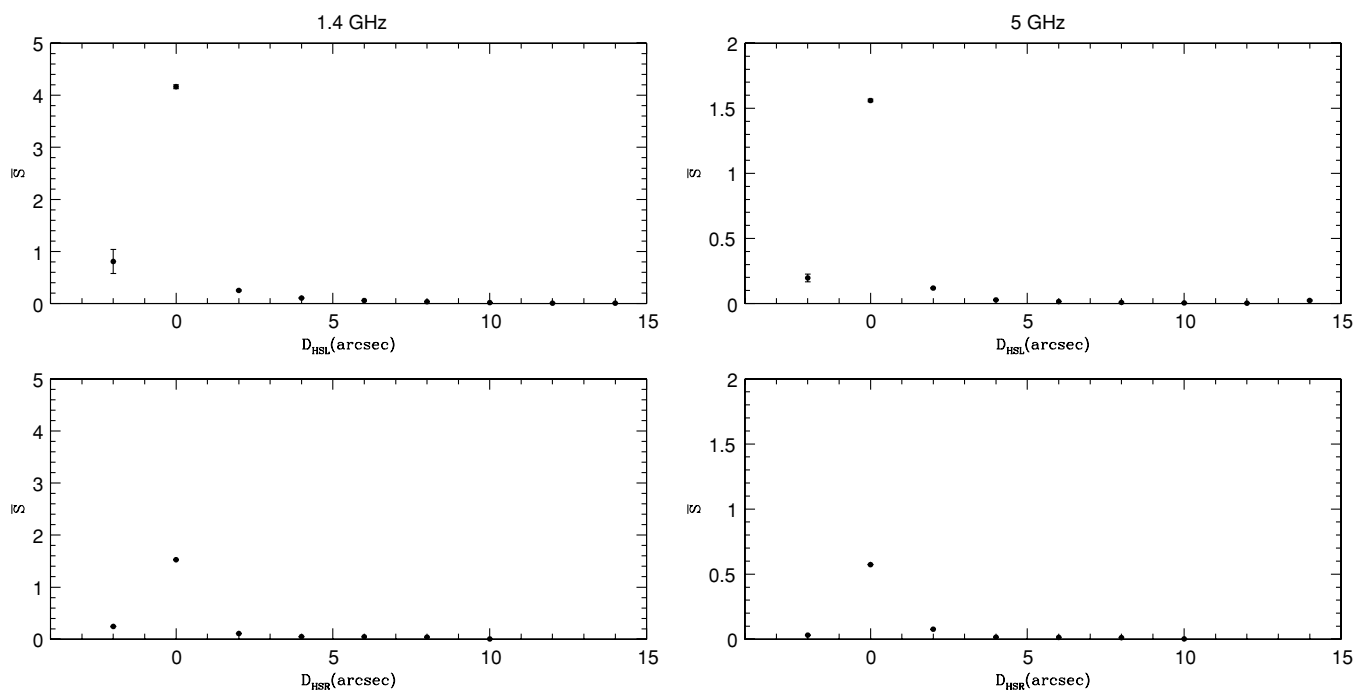


**Figure 10.** 3C6.1 average surface brightness in  $\text{Jy beam}^{-1}$  as a function of distance from the hot spot at 1.4 and 5 GHz (left and right panels, respectively) for the left- and right-hand sides of the source (top and bottom panels, respectively), as in Figure 4. The brightness peak at each hot spot is clearly visible. There is excellent agreement between results obtained at 1.4 GHz and 5 GHz.

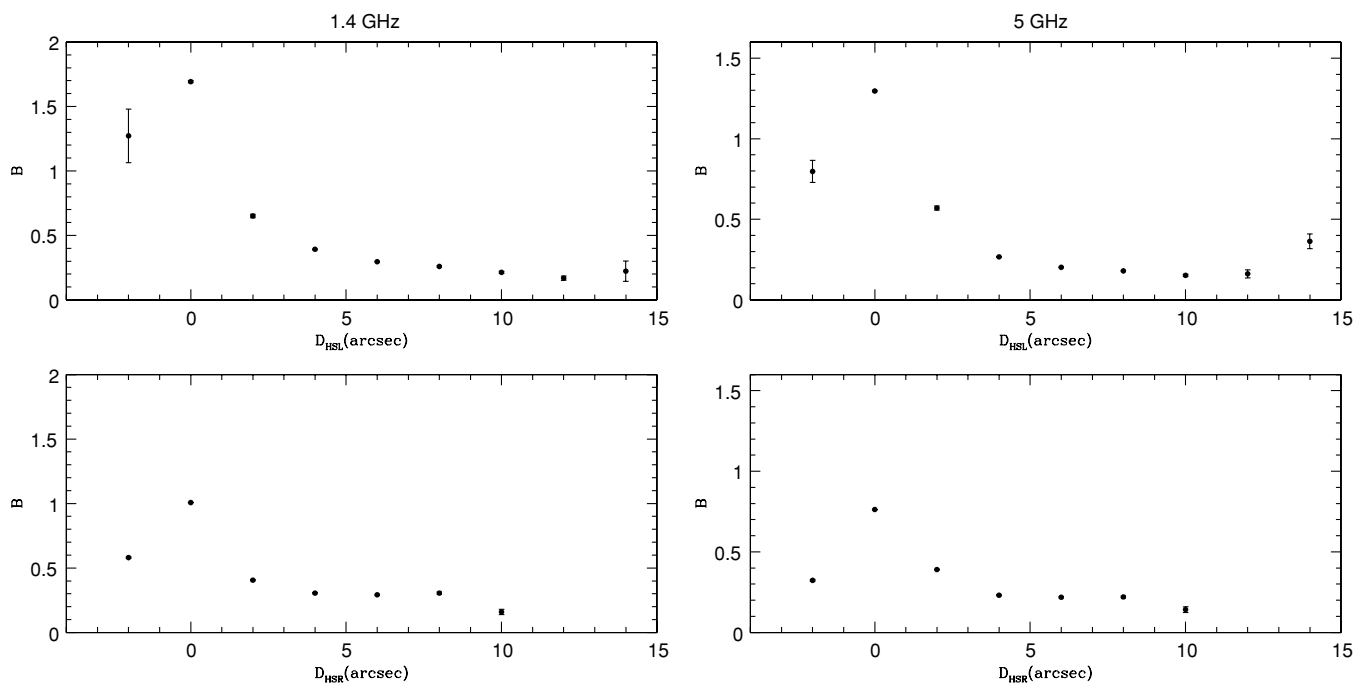


**Figure 11.** 3C6.1 minimum-energy magnetic field strength as a function of distance from the hot spot at 1.4 and 5 GHz (left and right panels, respectively) for the left- and right-hand sides of the source (top and bottom panels, respectively), as in Figure 4. Nearly identical results are obtained at 1.4 and 5 GHz. The normalization of the magnetic field strength is given in Table 1.

This indicates good agreement of the emissivity near the center of the slice obtained independently by stepping in from each of the two sides of the slice. Continuity of the emissivity near the center of a slice suggests that the assumption of semi-cylindrical symmetry is valid for that slice.

There are some very interesting deviations from a flat emissivity profile for a given slice. Some of the emissivity profiles suggest that the emissivity is largest near the edges of the slice,

and the emissivity has a minimum near the center of the slice. In most of the instances in which this occurs, the emissivity is continuous near the center of the slice, suggesting that the assumption of semi-cylindrical symmetry is valid for that slice. Interestingly, slices with emissivities that peak near the edge of the slice occur when the bridge width is close to a maximum. That is, the behavior of the emissivity profile is related to the bridge width as a function of distance from the hot spot. An

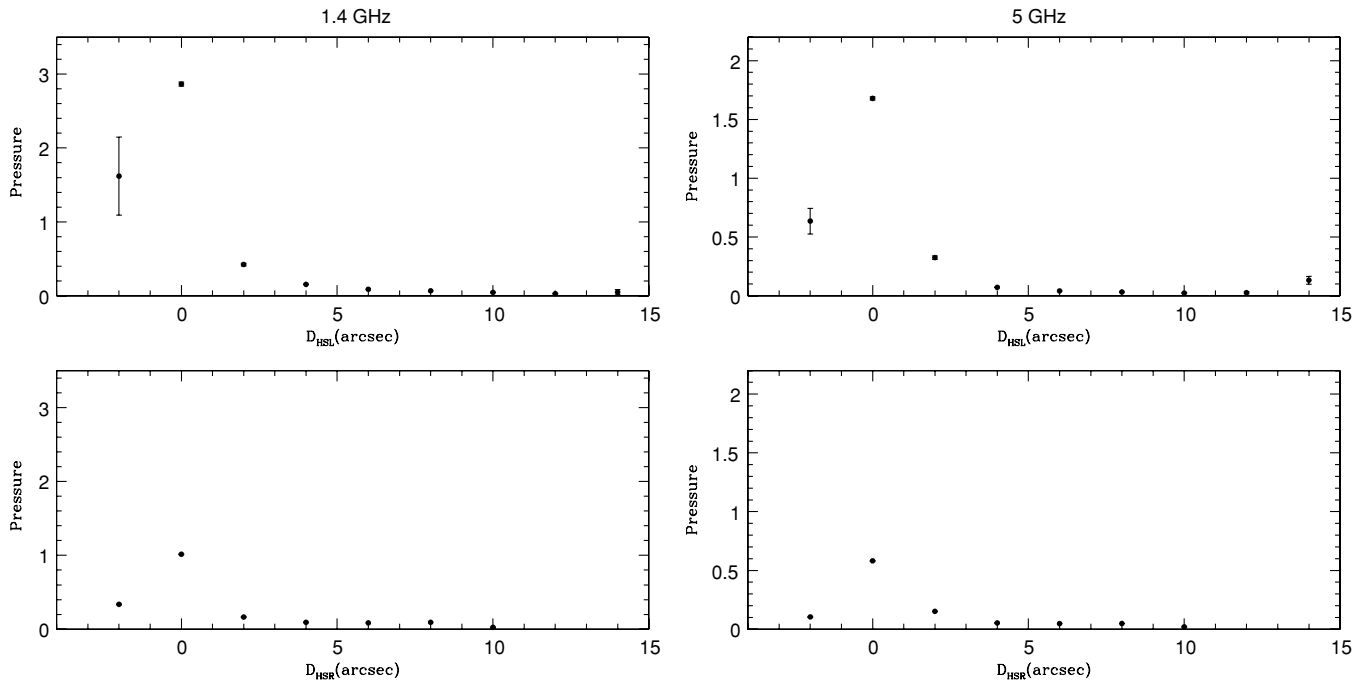


**Figure 12.** 3C6.1 minimum-energy pressure as a function of distance from the hot spot at 1.4 and 5 GHz (left and right panels, respectively) for the left- and right-hand sides of the source (top and bottom panels, respectively), as in Figure 11. Nearly identical results are obtained at 1.4 and 5 GHz. The normalization of the pressure is given in Table 1.

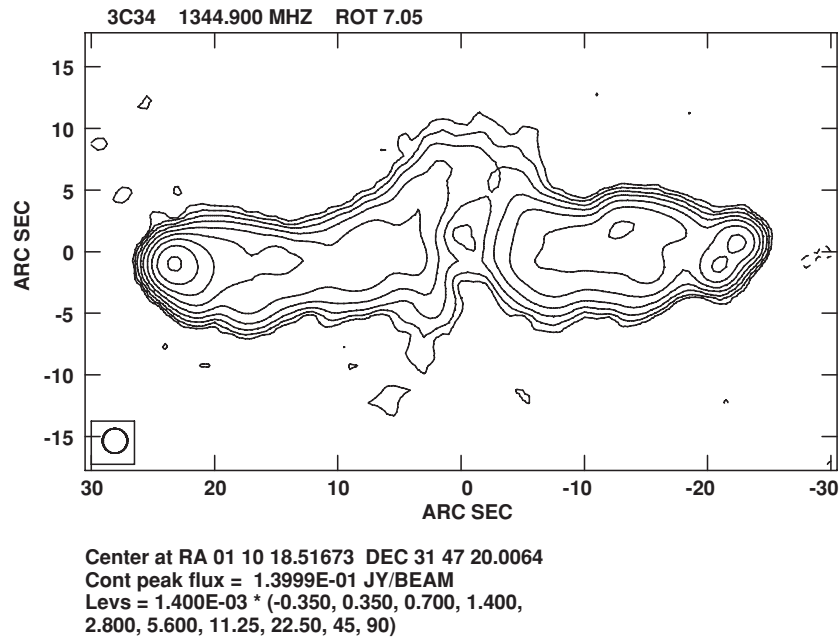


**Figure 13.** 3C34 at 1.4 GHz and 2'' resolution rotated by 7:05 counterclockwise, as in Figure 1.

emissivity profile that is “edge-peaked” is often found at the locations of the source where the bridge width is close to a maximum, discussed in Section 2.1. This can be seen on the left side of 3C6.1 (and perhaps also the right side of that source), 3C34, 3C142.1, 3C169.1, 3C172, 3C441, and perhaps the right side of 3C44 (see the 5 GHz results).

The emissivity of synchrotron radiation is related to the pressure of the relativistic fluid producing the radio emission. This follows because the minimum-energy pressure  $P \propto \epsilon_v^{4/7}$  introduced by Burbidge (1956), and the pressure can be obtained

from the minimum-energy pressure allowing for offsets from minimum-energy conditions, as discussed by Carvalho et al. (2005). So the pressure of the relativistic fluid is roughly proportional to the square root of the emissivity. Slices with the emissivity peaked away from the slice center, and with an emissivity minimum near the slice center, have a pressure profile with similar properties: the pressure is larger near the edge of the slice than it is near the center of the slice. And, slice to slice variations in the local emissivity and hence pressure are also apparent in the figures even though the average pressure of

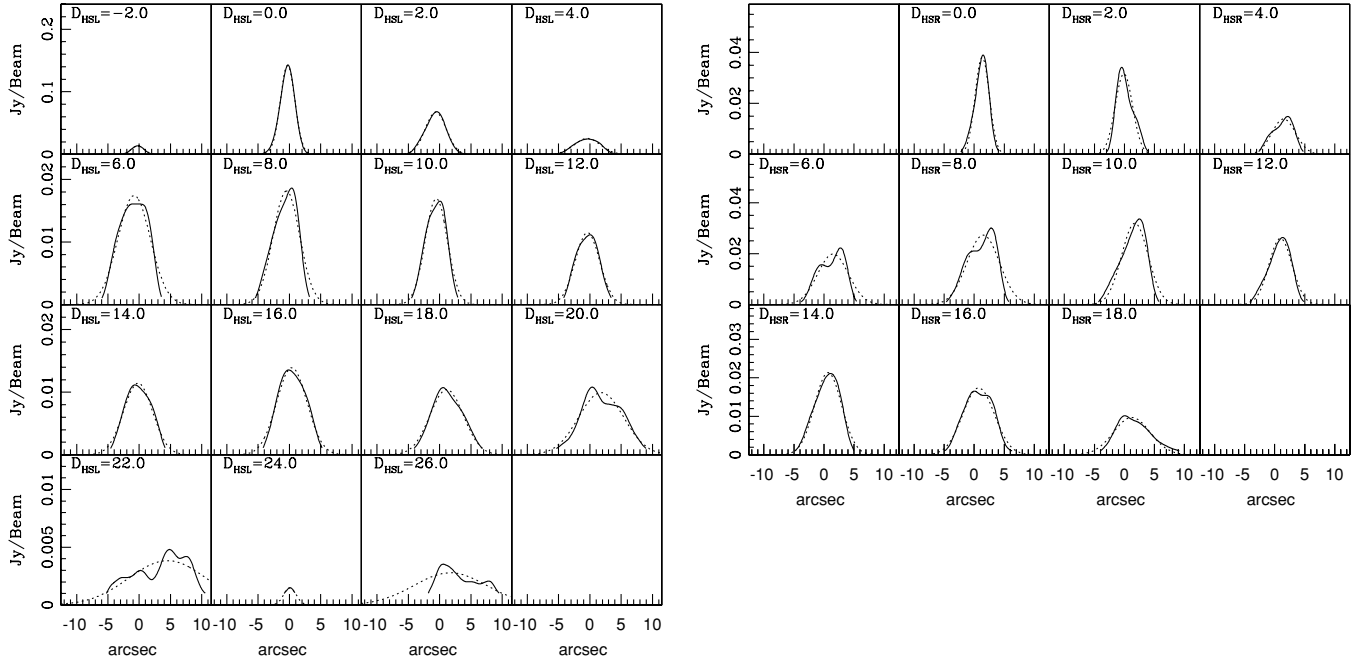


**Figure 14.** 3C34 surface brightness (solid line) and best-fit Gaussian (dotted line) for each cross-sectional slice of the radio bridge at 1.4 GHz, as in Figure 2. A Gaussian provides an excellent description of the surface brightness profile of each cross-sectional slice.

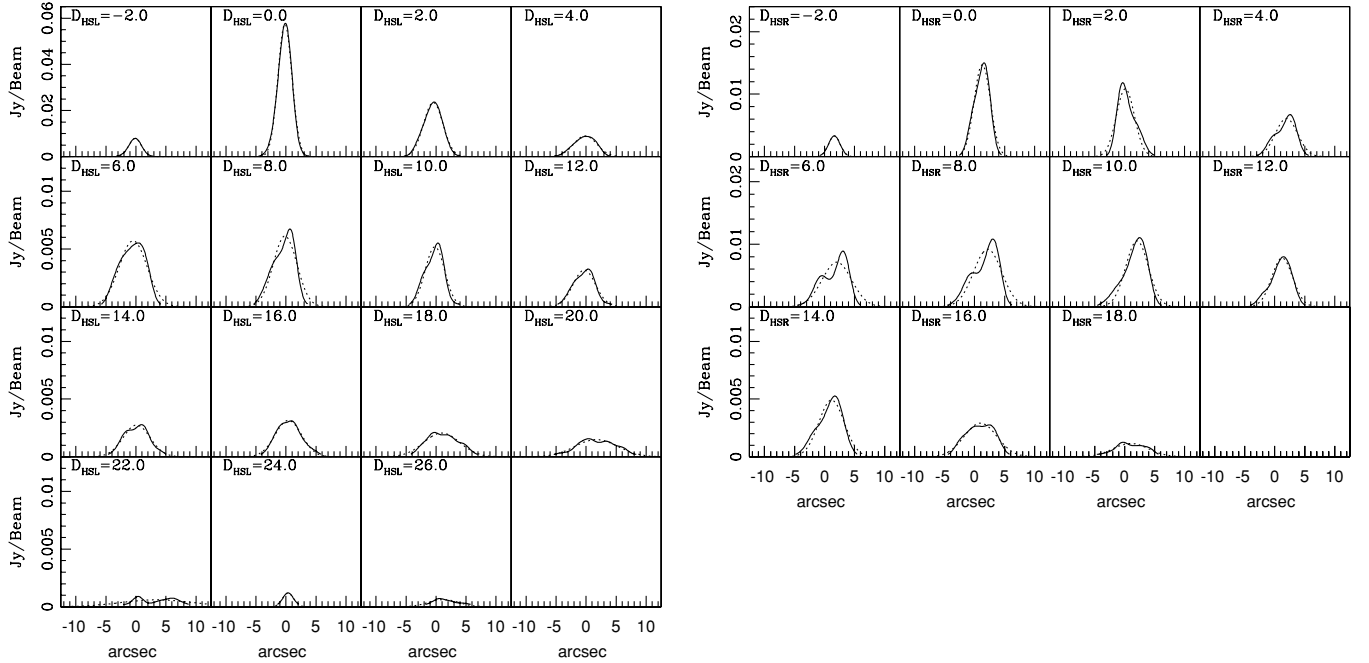


**Figure 15.** 3C34 surface brightness (solid line) and best-fit Gaussian (dotted line) for each cross-sectional slice of the radio bridge at 5 GHz, as in Figure 14 but at 5 GHz. Results obtained at 5 GHz are nearly identical to those obtained at 1.4 GHz.

slices tend to become fairly flat some distance from the hot spot for many sources, as discussed in Section 2.5.

Both the behavior of the source width as a function of distance from the hot spot and the existence of “edge-peaked” pressure profiles for slices near local maxima in the source width are reminiscent of the response of an outflow to a sudden drop in external pressure such as is experienced by an outflow passing through a nozzle (e.g., Courant & Friedrichs 1948; Owczarek 1964; Königl 1980; Daly & Marscher 1988). This suggests that, in the rest frame of the hot spot, the hot spot is somewhat

like the opening of a nozzle through which a relativistic fluid flows. In response to the series of waves that carry information about the pressure of the external medium to the relativistic fluid, the system overexpands in some regions and contracts in others causing the width to have a local maxima (much like those described in Section 2.1), and, for slices near those with maximum widths, causing the pressure near the edge of the slice to exceed that near the center.

Another possibility is that the fluctuations of the minimum-energy pressure could be due to changes in the magnetic field

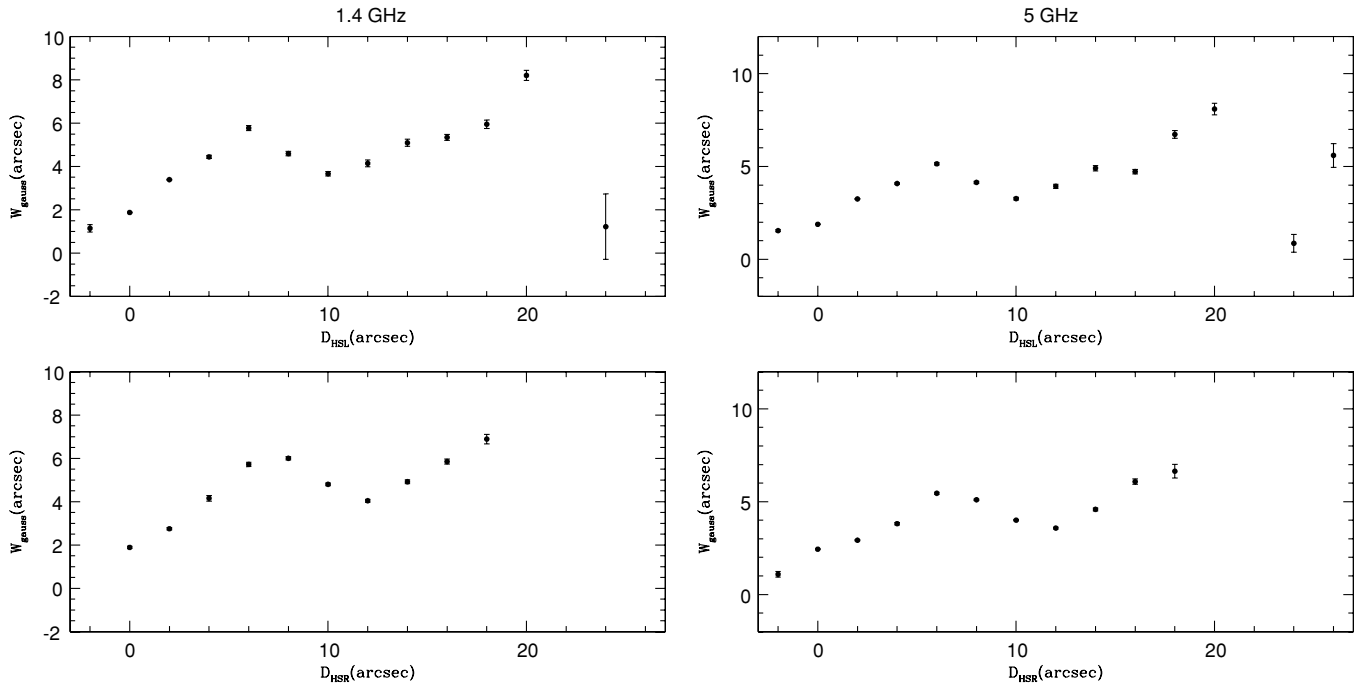


**Figure 16.** 3C34 Gaussian FWHM as a function of distance from the hot spot at 1.4 and 5 GHz (left and right panels, respectively) for the left- and right-hand sides of the source (top and bottom panels, respectively), as in Figure 4. The right- and left-hand sides of the source are almost perfectly symmetric. Similar results are obtained at 1.4 and 5 GHz.

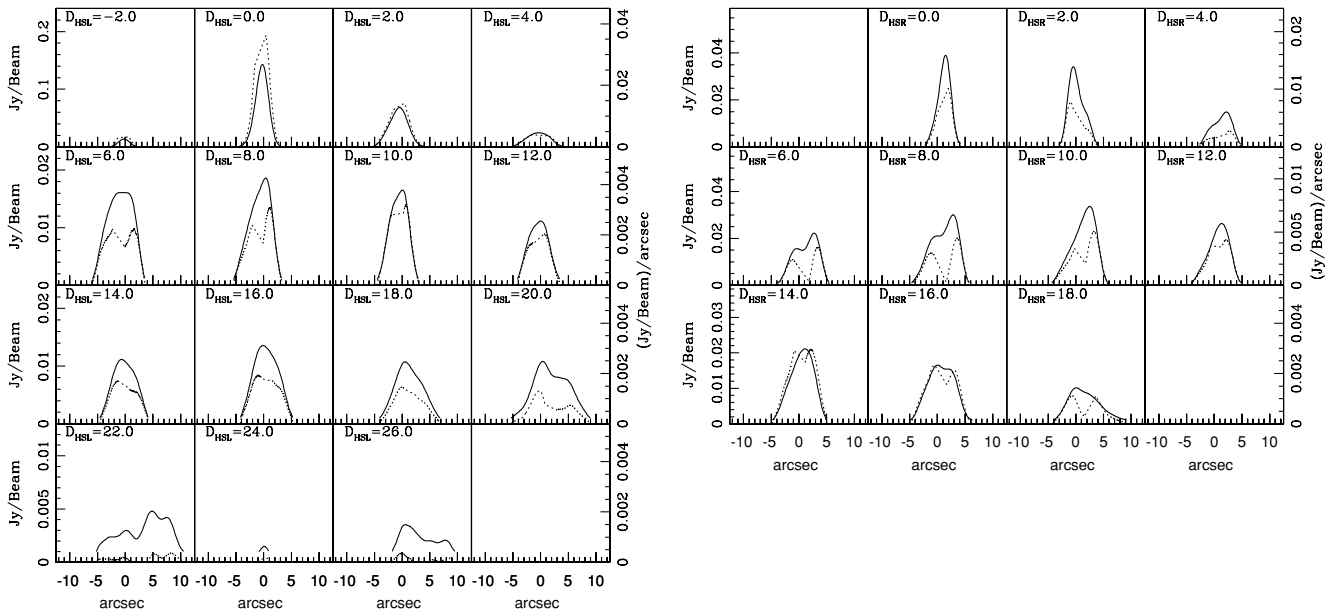


**Figure 17.** 3C34 emissivity (dotted line) and surface brightness (solid line) for each cross-sectional slice of the radio bridge at 1.4 GHz, as in Figure 5. A constant volume emissivity per slice provides a reasonable description of the data over most of the source.

structure that would result in changes in the offset of the field strength from the minimum-energy value, such as the field structures discussed by Eilek et al. (1997) and Tregillis et al. (2004). The fluctuations could also be an artifact of non-semi-cylindrical symmetry in a particular slice. This is signaled when the emissivity near the center of the slice is discontinuous or zero, as discussed earlier.

There are some slices with pressures that are both “edge-peaked” and “center-peaked,” having three pressure maxima with pressure minima between the slice center and edge. These can be seen, for example, in 3C44, 3C142.1, and 3C441. These types of features are also observed in the

emissivity and pressure slices of Cygnus A (Carvalho et al. 2005).

### 2.3. The First Moment

The first moment is a measure of the location of the surface brightness-weighted central axis of the source. This is obtained for each cross-sectional slice using the expression  $\bar{x} = \sum x_i S_i / \sum S_i$ , where  $S_i$  is the surface brightness at the position  $x_i$ . In obtaining the moments, each slice is treated independently. The locations  $x_i$  for each slice are evenly spaced with separations that are very small compared with the beam size. The first moment can be affected by the presence of the radio jet,

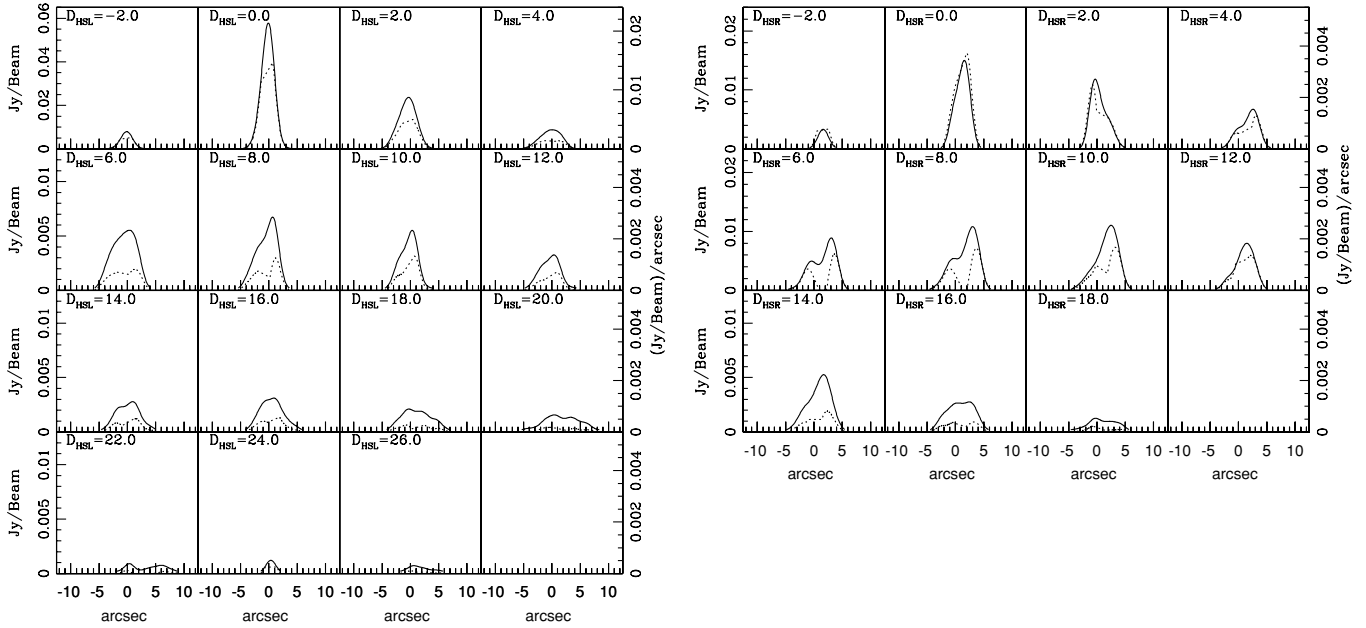


**Figure 18.** 3C34 emissivity (dotted line) and surface brightness (solid line) for each cross-sectional slice of the radio bridge at 5 GHz, as in Figure 17 but at 5 GHz. Results obtained at 5 GHz are nearly identical to those obtained at 1.4 GHz.

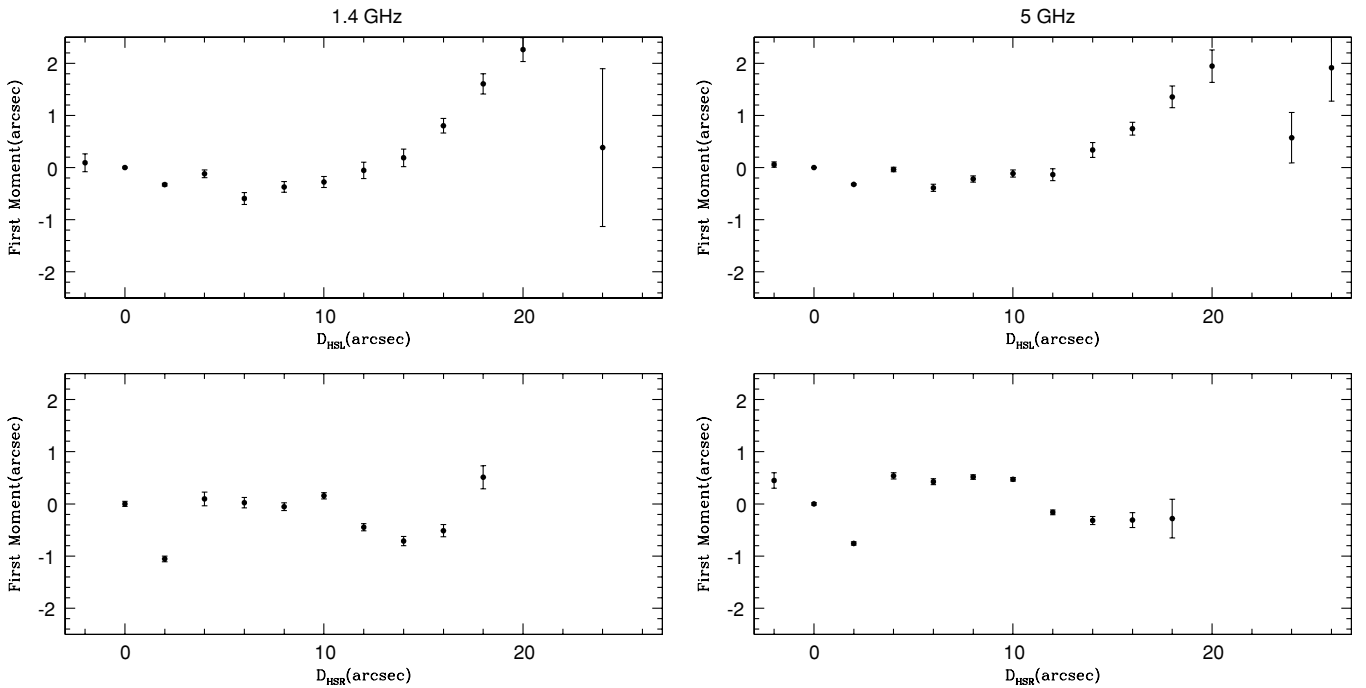


**Figure 19.** 3C34 first moment as a function of distance from the hot spot at 1.4 GHz and 5 GHz (left and right panels, respectively) for the left- and right-hand sides of the source (top and bottom, respectively), as in Figure 7. A side flow with an angular size of a few arcseconds is seen on the left-hand side of the source near the location of the AGN. This represents the “oldest” radio emitting plasma in the source, and could be due to the motion of the source relative to the ambient gas, or a back flow of plasma into the ambient gas, as discussed, for example, by Leahy & Williams (1984) and Leahy et al. (1989). Similar results are obtained at 1.4 and 5 GHz.

or a bulk sideways motion of the source. “Wiggles” in the first moment could be suggestive of a wobble of the outflow axis. Precession of the jet axes could give wiggles in the opposite sense on the two sides of the source. The wiggles could also be due to the wandering of the hot spot, as the plasma beam moves about along the cavity walls of the cocoon as in the “dentist’s drill” model (Scheuer 1982). The basic underlying assumption is that the ridgeline is due to the location of the hot spot when

that material was laid down, though it could later be affected by some other process, for example, by turbulence or instabilities in the cocoon or interaction with the jet.

The first moment as a function of the slice distance from the hot spot is shown in the figures. We observe wiggles in the first moment with a typical amplitude of 1”–2” over scales of 10”–20”. This tracks the wiggles of the source ridgeline, which can be seen in the contour plots.

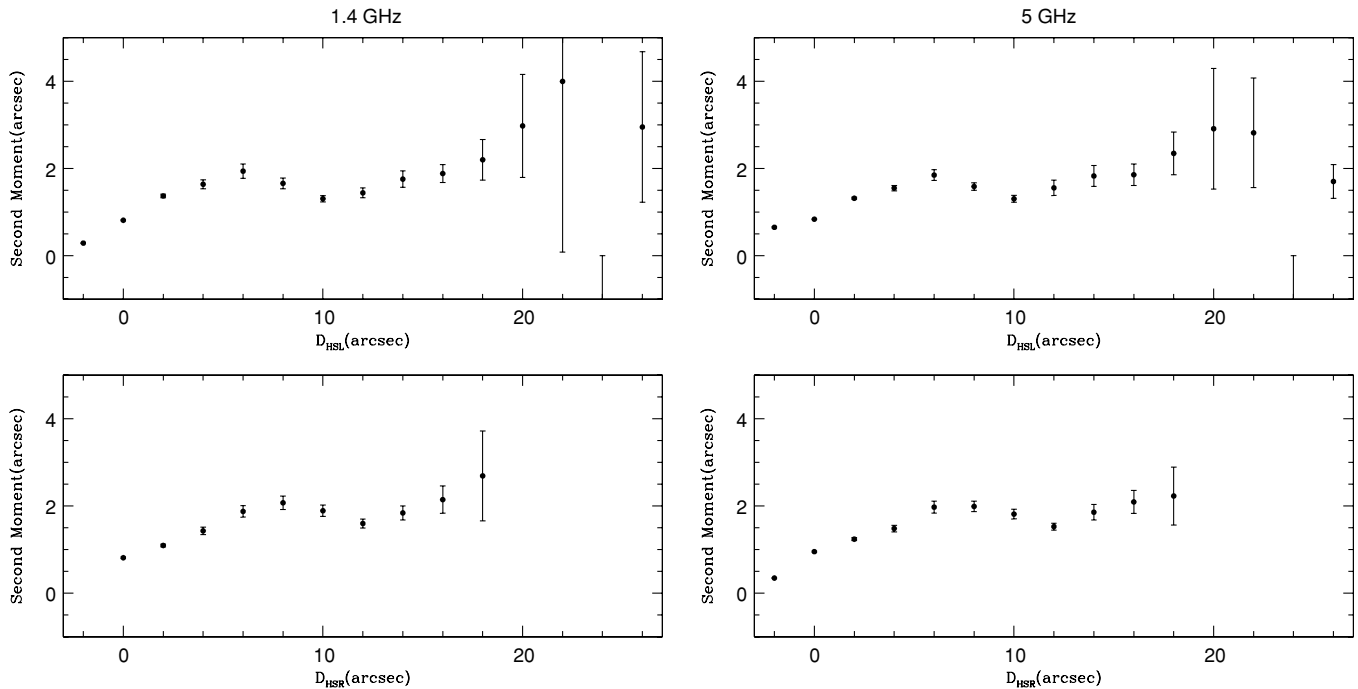


**Figure 20.** 3C34 second moment as a function of distance from the hot spot at 1.4 GHz and 5 GHz (left and right panels, respectively) for the left and right sides of the source (top and bottom panels, respectively), as in Figure 8. The right- and left-hand sides of the source are highly symmetric, as seen in Figure 16. Similar results are obtained at 1.4 and 5 GHz.

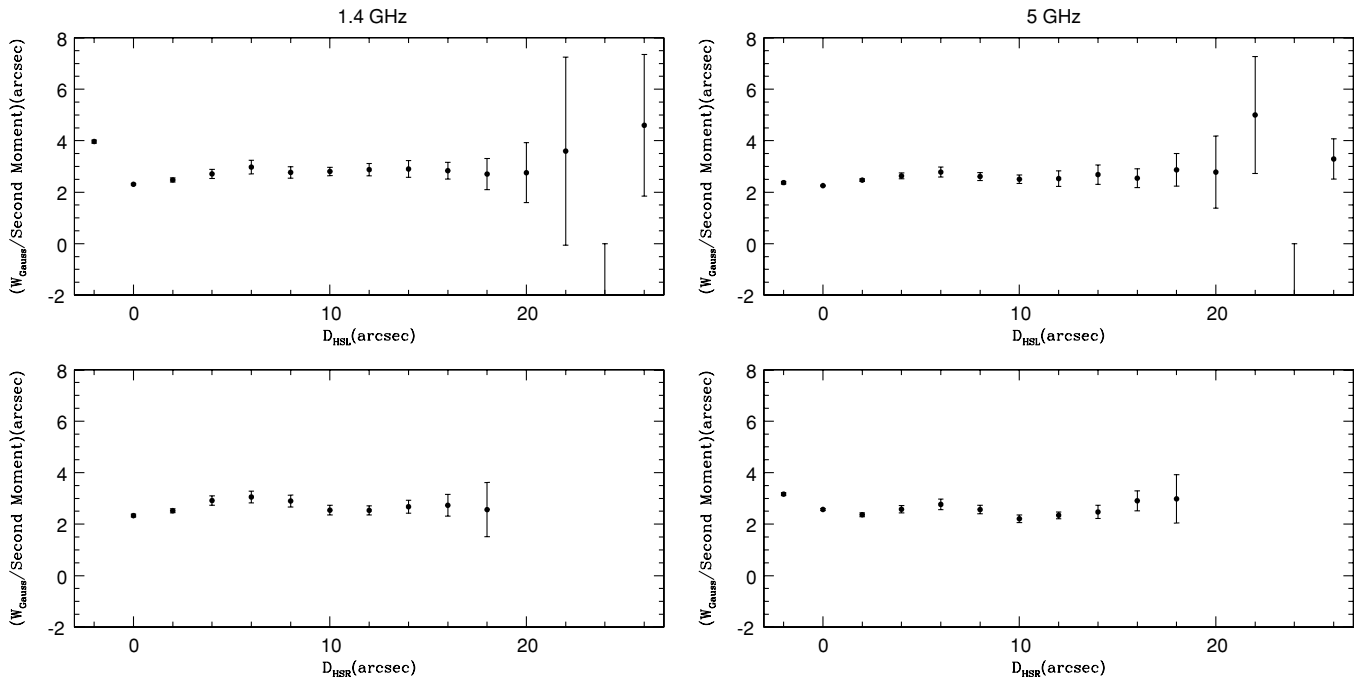


**Figure 21.** 3C34 ratio of the Gaussian FWHM to the second moment as a function of distance from the hot spot at 1.4 and 5 GHz (left and right panels, respectively) for the left- and right-hand sides of the source (top and bottom panels, respectively), as in Figure 9. The value of this ratio is fairly constant for each side of the source, and has a value of about 2. Similar results are obtained at 1.4 and 5 GHz.

Two obvious processes that could cause the first moment to deviate systematically from zero are a linear motion of the source relative to the ambient gas in a direction perpendicular to the source symmetry axis, and a twisting of the direction of the outflow axis of the AGN. The former would cause the first moment of both the right- and left-hand sides of the source to deviate from zero in the same sense. This is seen in the first moments of 3C44, 3C114, 3C142.1, 3C169.1, 3C172, and

perhaps in the 5 GHz data of 3C469.1. For these sources, it is possible to estimate the magnitude of the velocity of the source in the perpendicular direction,  $v_{\perp}$ , relative to the rate of growth of the source  $v_L$  along the directions of the hot spots. The deviation of the first moment from zero,  $\Delta(\text{FM})$ , divided by the distance over which this occurs,  $D_{\text{FM}}$ , is related to the source velocities:  $v_{\perp} = (\Delta(\text{FM})/D_{\text{FM}})v_L$ . For 3C44, the first moment varies by about  $1''$  over a distance of about

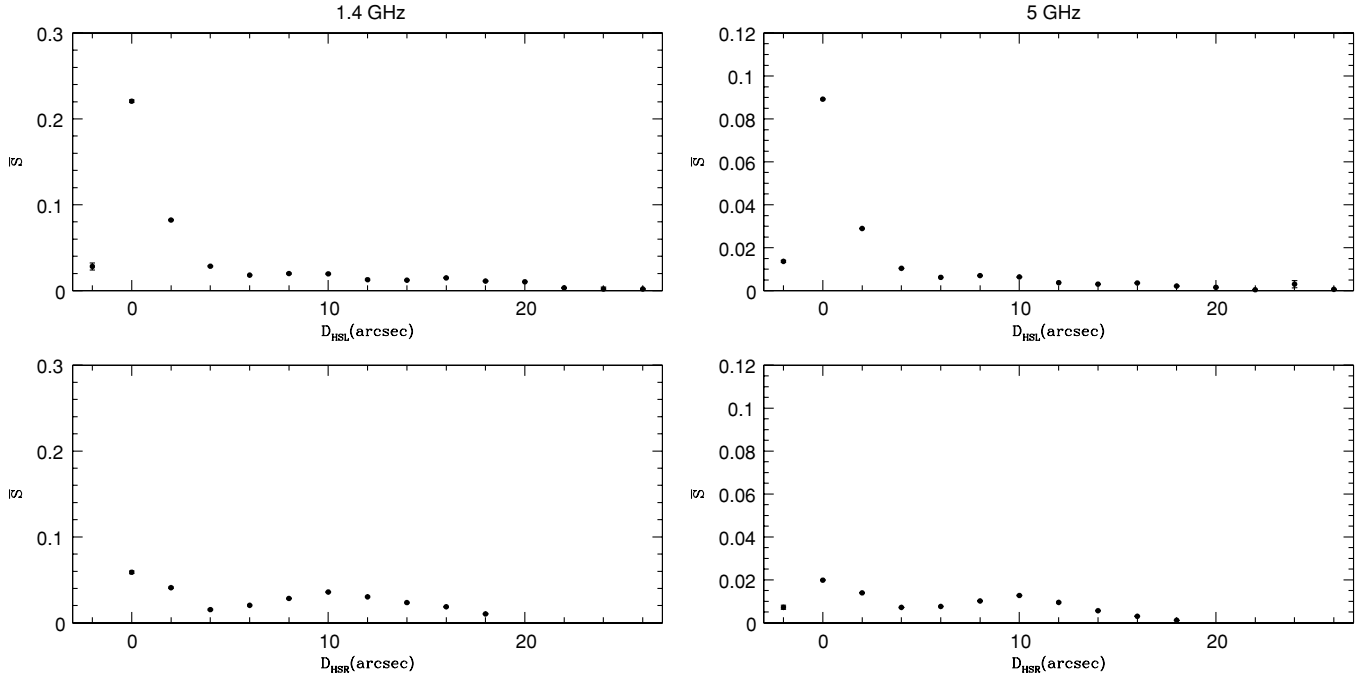


**Figure 22.** 3C34 average surface brightness in units of  $\text{Jy beam}^{-1}$  as a function of distance from the hot spot at 1.4 and 5 GHz (left and right panels, respectively) for the left- and right-hand sides of the source (top and bottom panels, respectively), as in Figure 10.

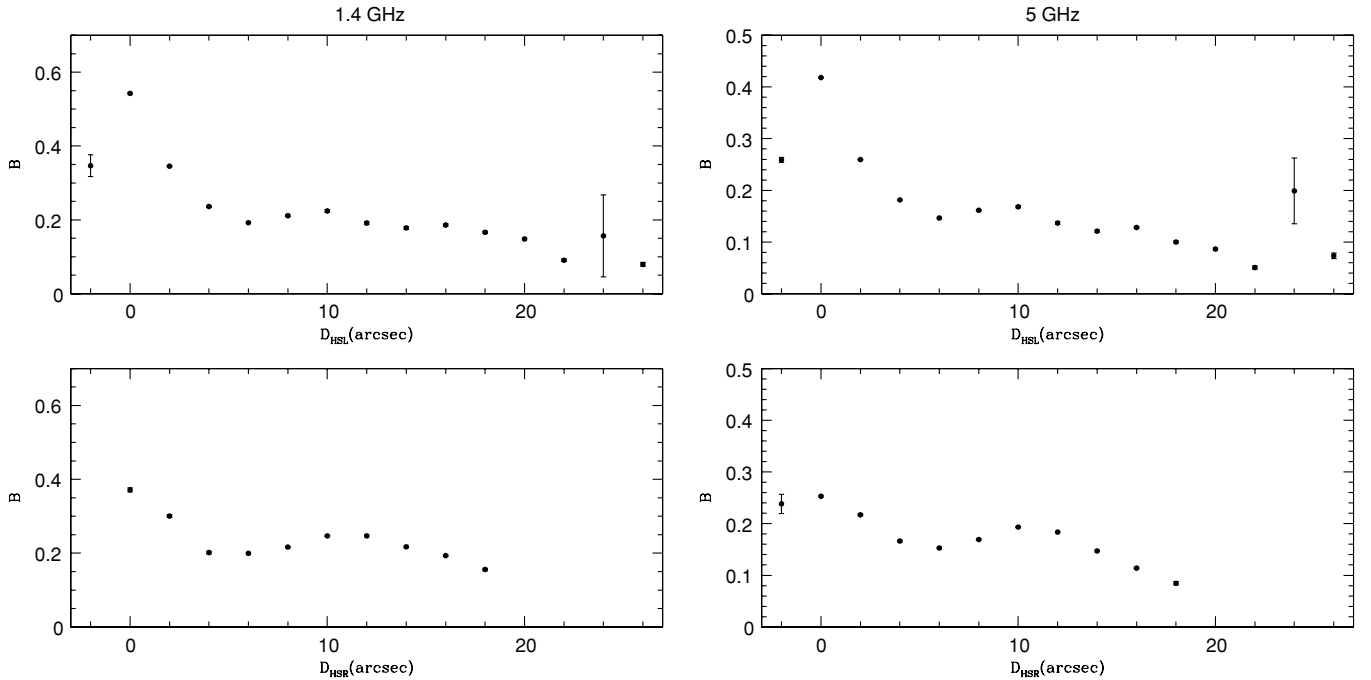


**Figure 23.** 3C34 minimum-energy magnetic field strength as a function of distance from the hot spot at 1.4 and 5 GHz (left and right panels, respectively) for the left- and right-hand sides of the source (top and bottom panels, respectively), as in Figure 11. The normalization is given in Table 1.

$10''$ , so  $v_{\perp} \simeq 0.1v_L \simeq 2.5 \times 10^3 \text{ km s}^{-1}$ , where a value of  $v_L$  of about  $0.05c$  obtained by O’Dea et al. (2009) for this source was used. This value of  $v_L$  was obtained assuming an offset,  $b$ , of the magnetic field strength in the radio bridge from minimum-energy conditions of 0.25. For 3C114, the first moment deviates from zero by about  $1''$  over  $20''$ , so  $v_{\perp} \simeq 0.05v_L \simeq 750 \text{ km s}^{-1}$  for  $v_L \simeq 0.05c$ , obtained by O’Dea et al. (2009) for  $b = 0.25$ . For 3C142.1, the first moment deviates from zero by about  $2''$  over a distance of about  $10''$ , so

$v_{\perp} \simeq 0.2v_L \simeq 2 \times 10^3 \text{ km s}^{-1}$  for  $v_L \simeq 0.033c$  obtained by O’Dea et al. (2009) assuming  $b = 0.25$ . For 3C169.1, the first moment deviates by about  $3''$  over a distance of about  $20''$ , so  $v_{\perp} \simeq 0.15v_L \simeq 2 \times 10^3 \text{ km s}^{-1}$  for a value of  $v_L \simeq 0.044c$  obtained by O’Dea et al. (2009) for  $b = 0.25$ . For 3C172, the first moment deviates by about  $4''$  over  $20''$  on the left-hand side of the source, so  $v_{\perp} \simeq 0.2v_L \simeq 3 \times 10^3 \text{ km s}^{-1}$  for  $v_L \simeq 0.058$  for this side of the source for  $b = 0.25$  (O’Dea et al. 2009). The right-hand side of the source shows a step function behavior,

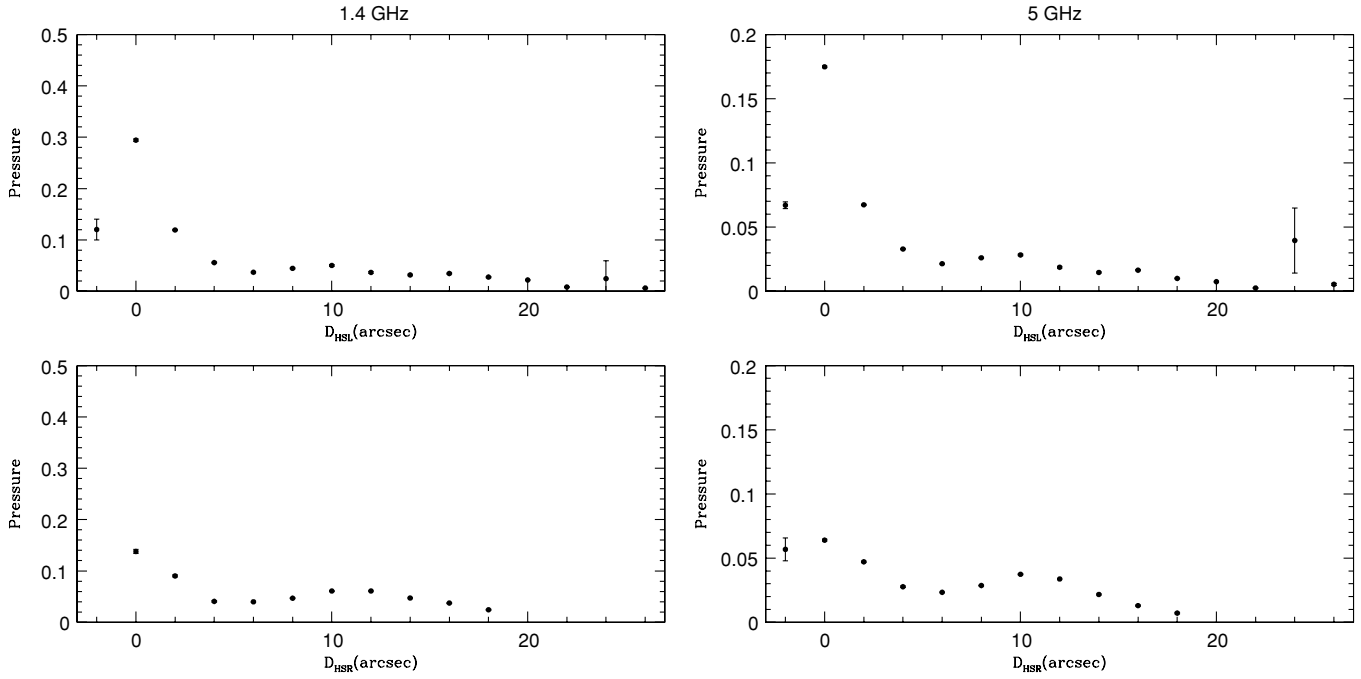


**Figure 24.** 3C34 minimum-energy pressure as a function of distance from the hot spot at 1.4 and 5 GHz (left and right panels, respectively) for the left- and right-hand sides of the source (top and bottom panels, respectively), as in Figure 12. The normalization is given in Table 1.

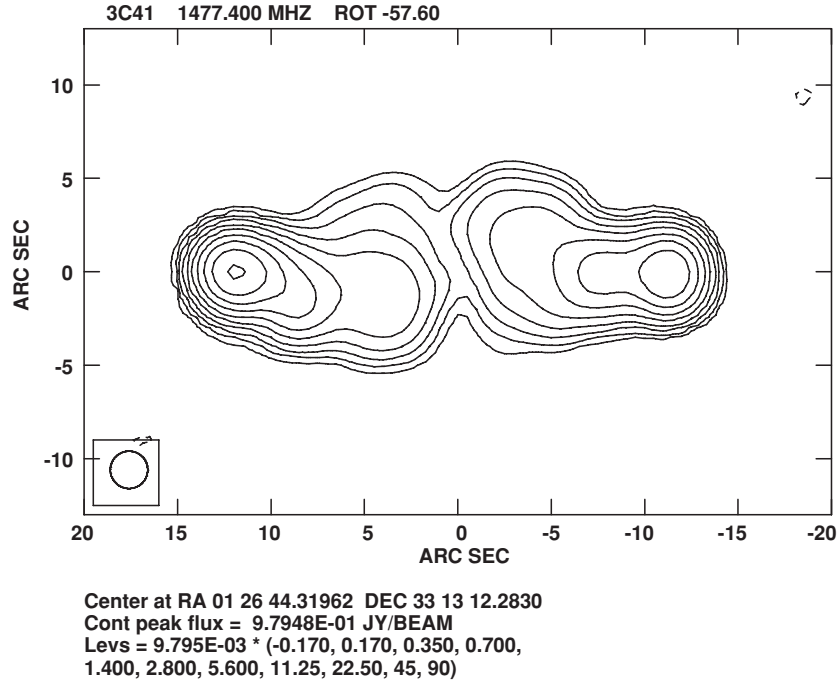


**Figure 25.** 3C41 at 1.4 GHz and 2'' resolution rotated by 57°60 clockwise, as in Figure 1.

so the left-hand side only is considered here. For 3C469.1, the deviation for the first moment from zero is about 1'' over a distance of 10'', so  $v_{\perp} \sim 0.1v_L \sim 3 \times 10^3 \text{ km s}^{-1}$  for  $v_L \sim 0.1c$  obtained for  $b = 0.25$  by O’Dea et al. (2009).

The values of  $v_{\perp} \simeq \text{few} \times 10^3 \text{ km s}^{-1}$  obtained seem quite reasonable. All of these values of  $v_L$  and  $v_{\perp}$  increase by about a factor of 3 if a value of  $b = 1$  (i.e., minimum-energy conditions) is adopted. If the systematic deviations of the first moment from zero are due to the motion of the AGN relative to the ambient gas, the reasonable values of  $v_{\perp}$  obtained for  $b = 0.25$  suggest that the synchrotron ages obtained for these sources assuming  $b = 0.25$  are reliable. Of course, these deviations of the first

moment from zero could be due to other factors, in which case these estimates of  $v_{\perp}$  obtained should be taken as upper bounds.

A deviation of the first moment from zero that is in the opposite sense for each side of the source would be produced if the direction of the outflow axis of the AGN is shifting over time. This behavior is seen in the first moments of 3C41, 3C54, and 3C441. 3C41 has a first moment that deviates from zero by about 1'' over a distance of 5'', suggesting that the axis of the outflow has shifted by about 0.2 rad, or about 10°. 3C54 has a first moment that deviates from zero by about 1'' over a distance of about 10'', suggesting that the outflow axis has shifted by about 0.1 rad, or 6°. And, 3C441 has a first moment that has

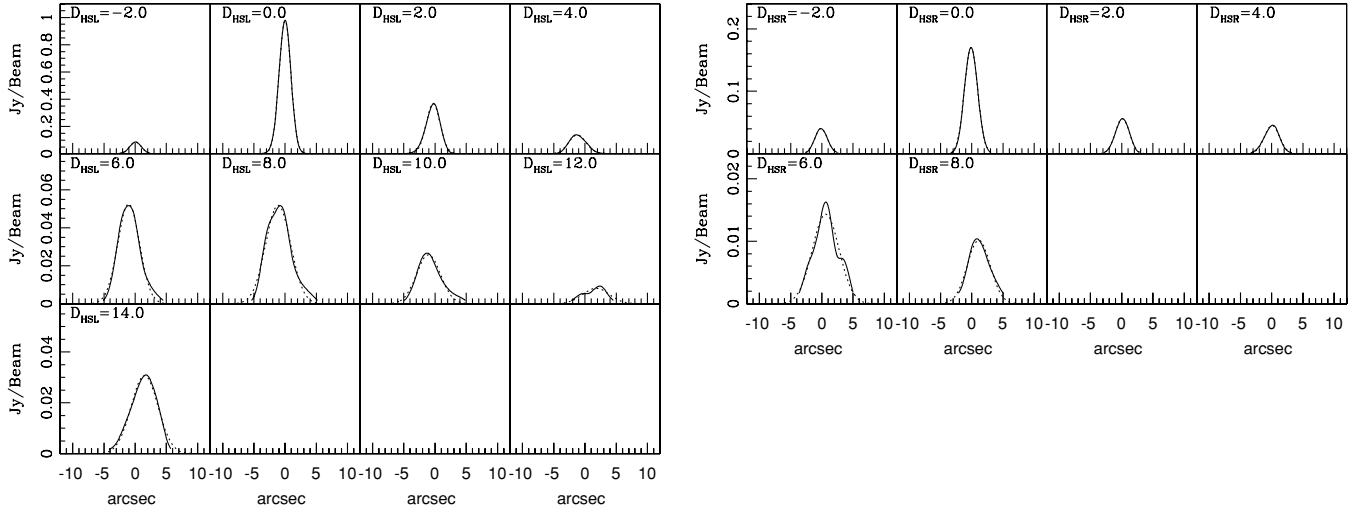


**Figure 26.** 3C41 surface brightness (solid line) and best-fit Gaussian (dotted line) for each cross-sectional slice of the radio bridge at 1.4 GHz, as in Figure 2. A Gaussian provides an excellent description of the surface brightness profile of each cross-sectional slice.

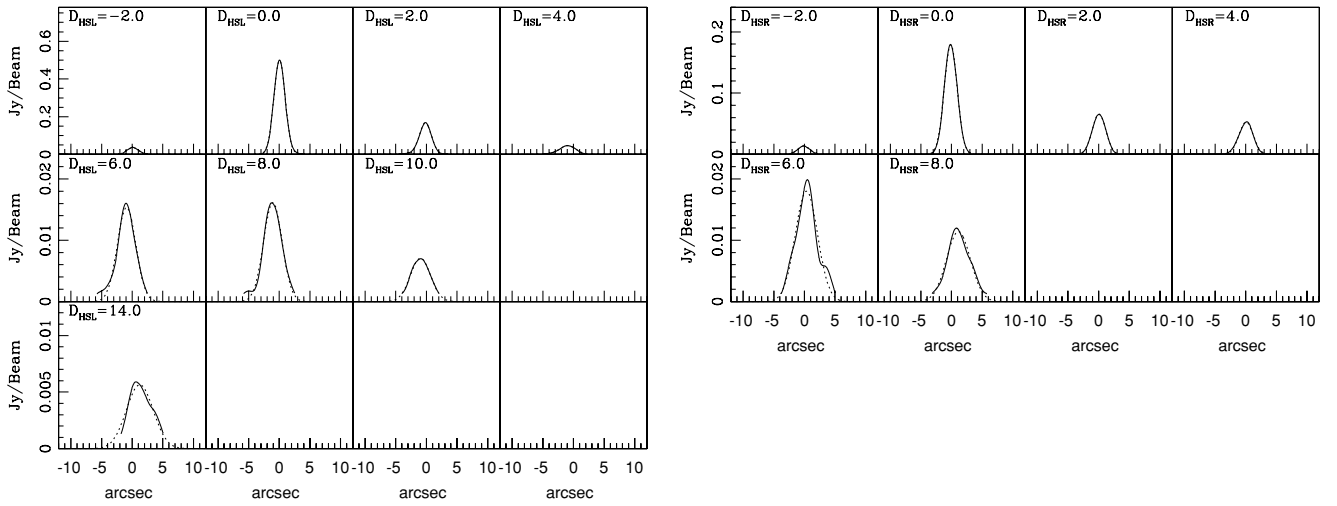


**Figure 27.** 3C41 surface brightness (solid line) and best-fit Gaussian (dotted line) for each cross-sectional slice of the radio bridge at 5 GHz, as in Figure 26 but at 5 GHz. Results obtained at 5 GHz are nearly identical to those obtained at 1.4 GHz.

shifted by about  $2''$  over a distance of about  $10''$ , suggesting the outflow axis has moved by about  $0.2$  rad or about  $10^\circ$ . Of course, other processes, such as side flows, etc., could have caused these deviations in which case the numbers obtained should be taken as upper bounds. Taking these constraints as bounds, the sources have  $v_\perp$  less than about  $(750\text{--}few \times 10^3)$  km s $^{-1}$ , and changes in outflow angle of less than about (few–10) degrees.

The remaining two sources, 3C6.1 and 3C34, have a first moment that appears to be flat on one side of the source, and deviates from zero on the other side of the source. The left side of 3C6.1 has a first moment that deviates by less than  $0.5'$  over a distance of  $10''$ , so the perpendicular velocity must be quite small,  $v_\perp < 0.05v_L < 750$  km s $^{-1}$  for  $v_L \simeq 0.05c$  obtained by O'Dea et al. (2009) for this source assuming  $b = 0.25$ . The outflow axis of the source could not have shifted by more than about  $0.05$  rad, or  $3^\circ$ . The structure of 3C34 is more complex, suggesting a sideways drift of the first moment on the left side of the source, and more chaotic motion on the right side of the source. This is consistent with other results obtained for this source. Based on optical imaging and spectroscopy, Best et al. (1997) concluded that the jet in 3C34 (on the western or right side of the source) seems to have passed through a

companion galaxy in the cluster to which 3C34 belongs, at a distance of about 120 kpc ( $17''$ ) from the core of 3C34, thereby inducing massive star formation in the companion galaxy. Based on the aging starburst in the companion galaxy, Best et al. (1997) concluded that the jet axis in 3C34 eventually changed direction due to precession, and is not currently passing through the companion galaxy. The precession is responsible for the new currently active hot spot, which is situated to the south of the older hot spot. Our first moment analysis shows a sideways drift on the left side of the source (east side of 3C34), and a more chaotic motion on the right side (west side of 3C34). This is consistent with the conclusions of Best et al. (1997). Interestingly, the source seems to be quite symmetric in terms of the width as a function of distance from the hot spot, and there does not seem to be any sign of the interaction on that parameter. The emissivity on the right side of the source seems to go to zero near the symmetry axis of the source at distances of 6, 8, and 18 arcsec from the hot spot, which may be a signature that the assumption of semi-cylindrical symmetry has broken down at these locations. Distances of 6 and 8 arcsec are near the location of the companion galaxy with which the radio jets may have interacted.

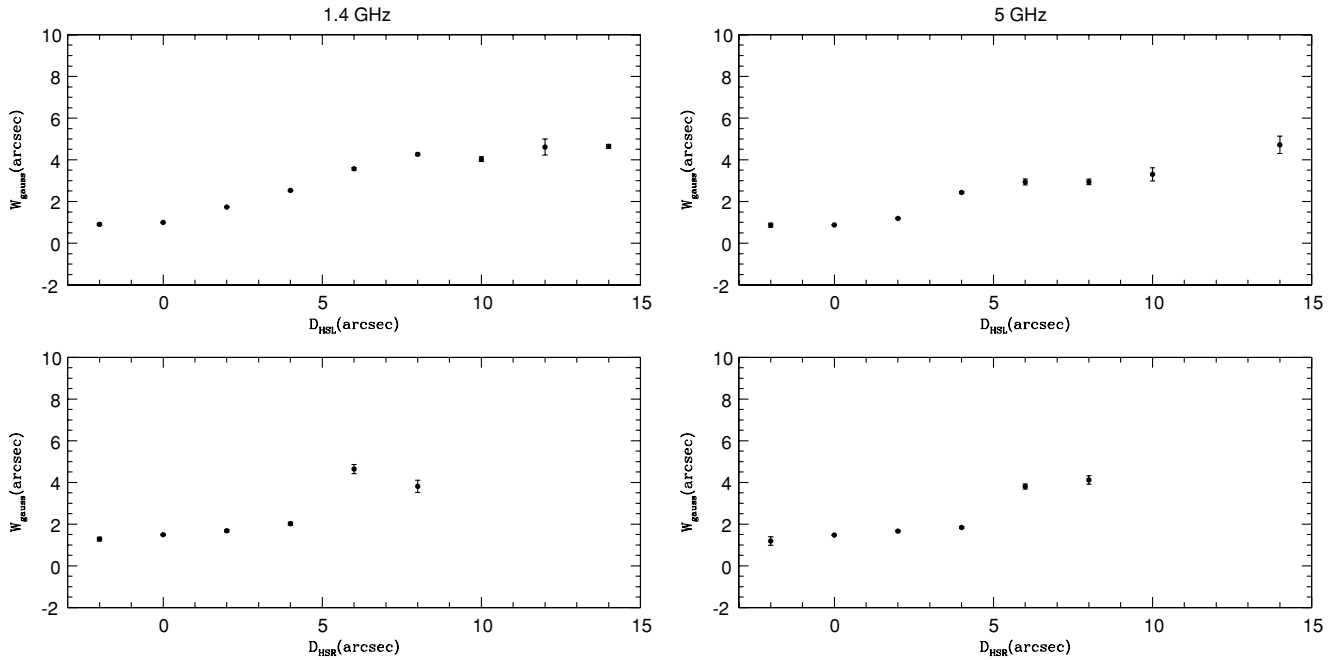


**Figure 28.** 3C41 Gaussian FWHM as a function of distance from the hot spot at 1.4 and 5 GHz (left and right panels, respectively) for the left- and right-hand sides of the source (top and bottom panels, respectively), as in Figure 4. The right- and left-hand sides of the source are fairly symmetric. Similar results are obtained at 1.4 and 5 GHz.

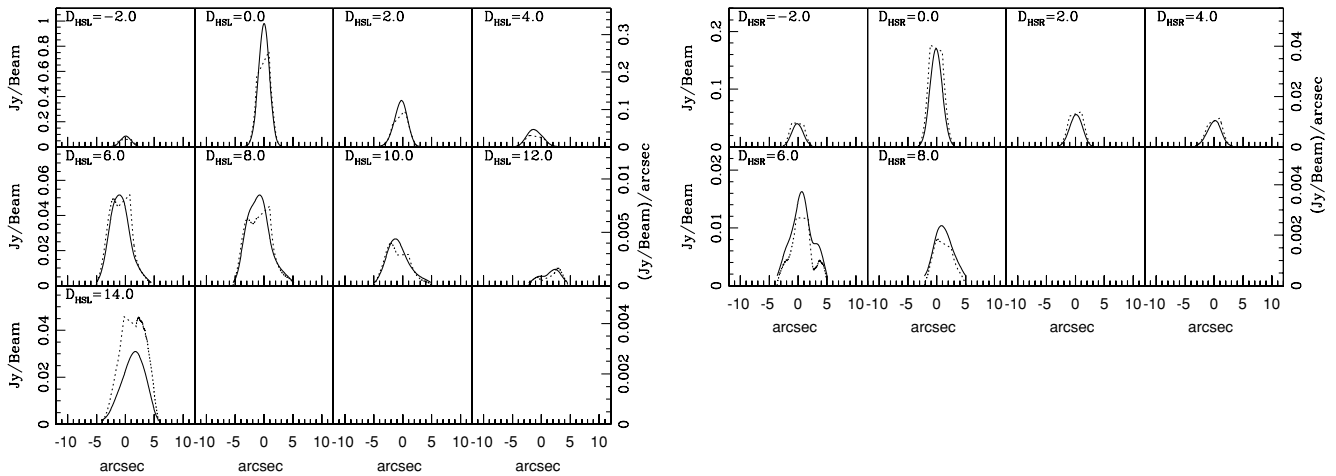


**Figure 29.** 3C41 emissivity (dotted line) and surface brightness (solid line) for each cross-sectional slice of the radio bridge at 1.4 GHz, as in Figure 5. A constant volume emissivity per slice provides a reasonable description of the data over most of the source.

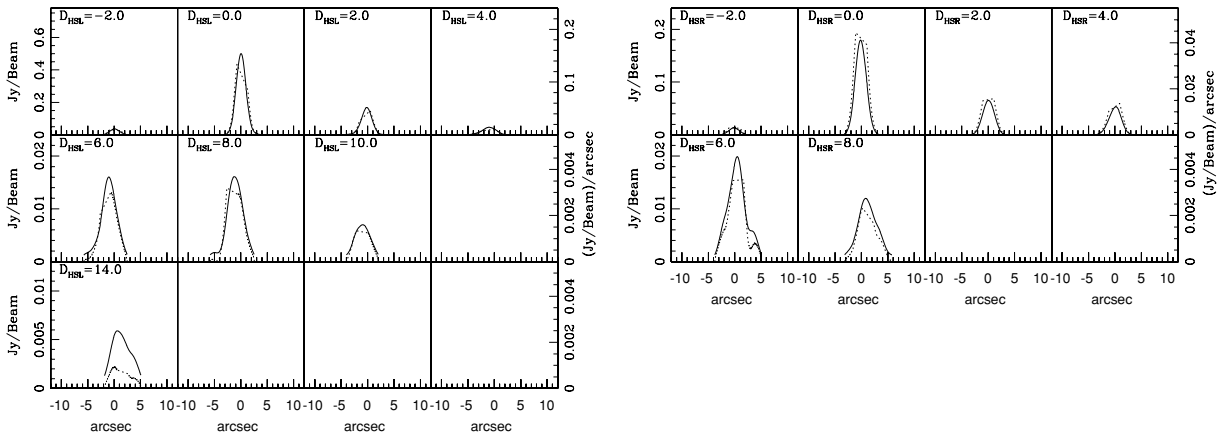


**Figure 30.** 3C41 emissivity (dotted line) and surface brightness (solid line) for each cross-sectional slice of the radio bridge at 5 GHz, as in Figure 29 but at 5 GHz. Results obtained at 5 GHz are nearly identical to those obtained at 1.4 GHz.

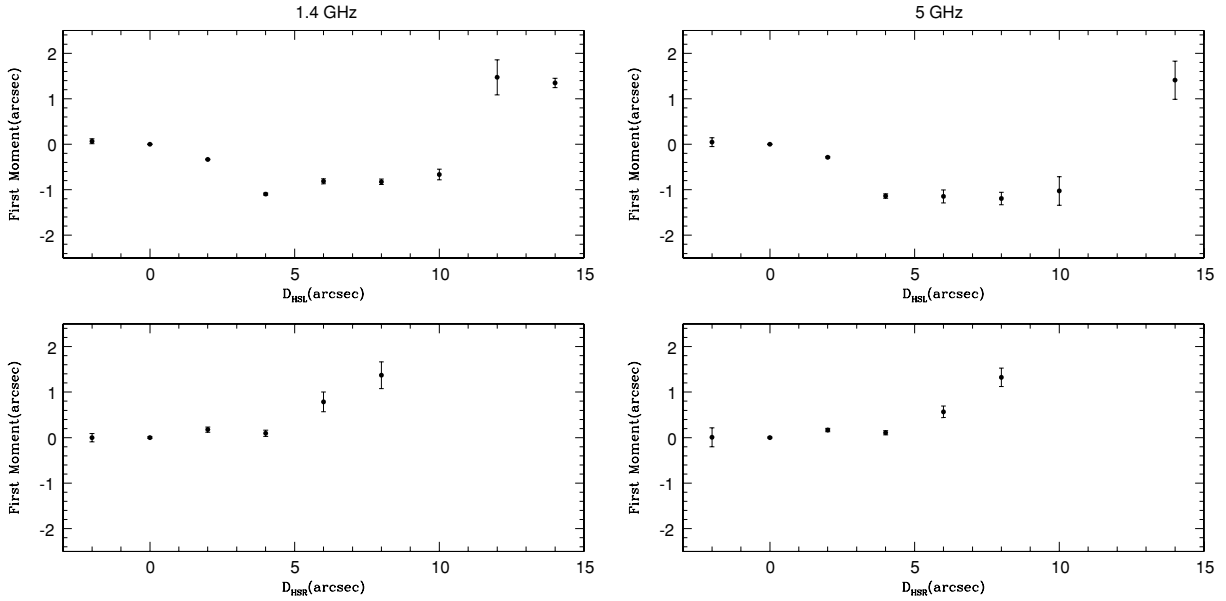


**Figure 31.** 3C41 first moment as a function of distance from the hot spot at 1.4 GHz and 5 GHz (left and right panels, respectively) for the left- and right-hand sides of the source (top and bottom, respectively).

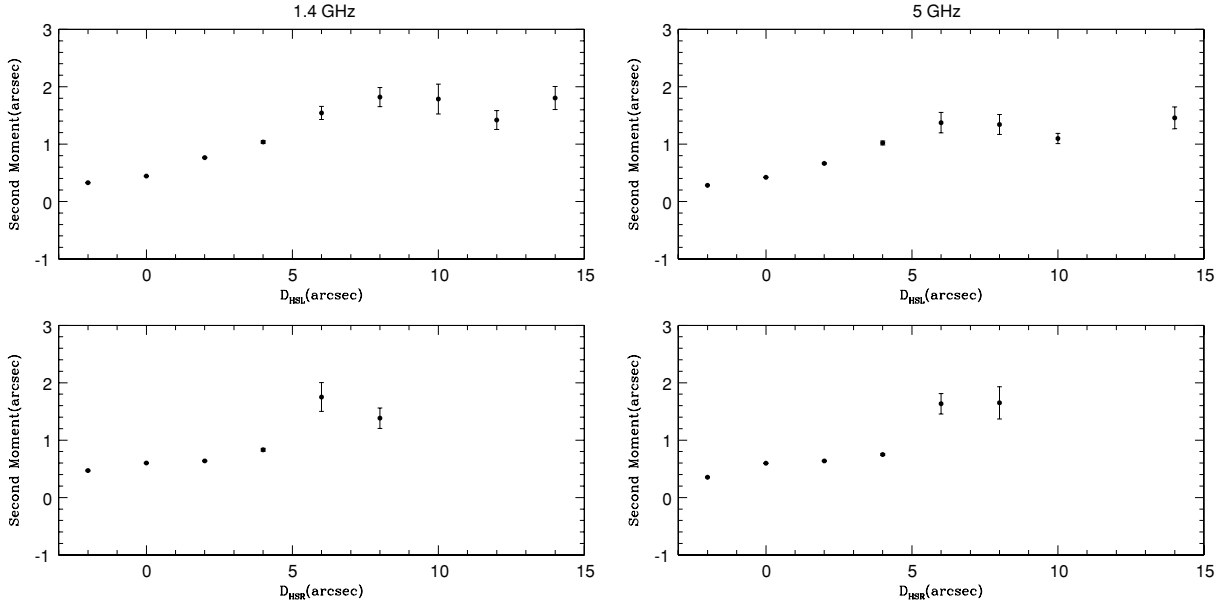


**Figure 32.** 3C41 second moment as a function of distance from the hot spot at 1.4 GHz and 5 GHz (left and right panels, respectively) for the left and right sides of the source (top and bottom panels, respectively).

#### 2.4. Second Moment and Comparison with Gaussian FWHM

The second moment is another measure of the bridge width. It is obtained for each cross-sectional slice using the expression  $(\sum S_i [x_i - \bar{x}]^2 / \sum S_i)^{1/2}$ , where  $S_i$  is the surface brightness at the position  $x_i$ , and  $\bar{x}$  is the first moment (see Section 2.3). In general, the source width as measured by the second moment is very similar to that indicated by the Gaussian width  $W_G$ .

The ratio of the second moment to the Gaussian FWHM remains fairly constant for each side of each source, with source to source variations that range from about 2.0 to 3.0 for the 11 sources studied, as can be seen in the figures. The second moment is a measure of the half-width of the source, so the width indicated by the Gaussian FWHM is about 25% larger than the width indicated by twice the second moment. For a slice with a constant emissivity, the ratio of the Gaussian

FWHM to the second moment is expected to be about 2.7 (see Table 1 of Carvalho et al. (2005) and account for the fact that the second moment measures a half width rather than a full width). This value for the ratio is quite close to those obtained empirically here, and is consistent with the typical emissivity profiles obtained for most slices. This ratio is expected to be slightly larger when the emissivity is “edge-peaked” (Carvalho et al. 2005), but the difference is so small that is difficult to detect.

#### 2.5. Mean Surface Brightness, Magnetic Field Strength, and Pressure

The average surface brightness of a slice,  $\bar{S}$ , is obtained by dividing the area under the surface brightness profile by  $W_G$ , and is shown in the figures; the units of  $\bar{S}$  are  $\text{Jy beam}^{-1}$ . The hot spot dominates the surface brightness of the lobe.

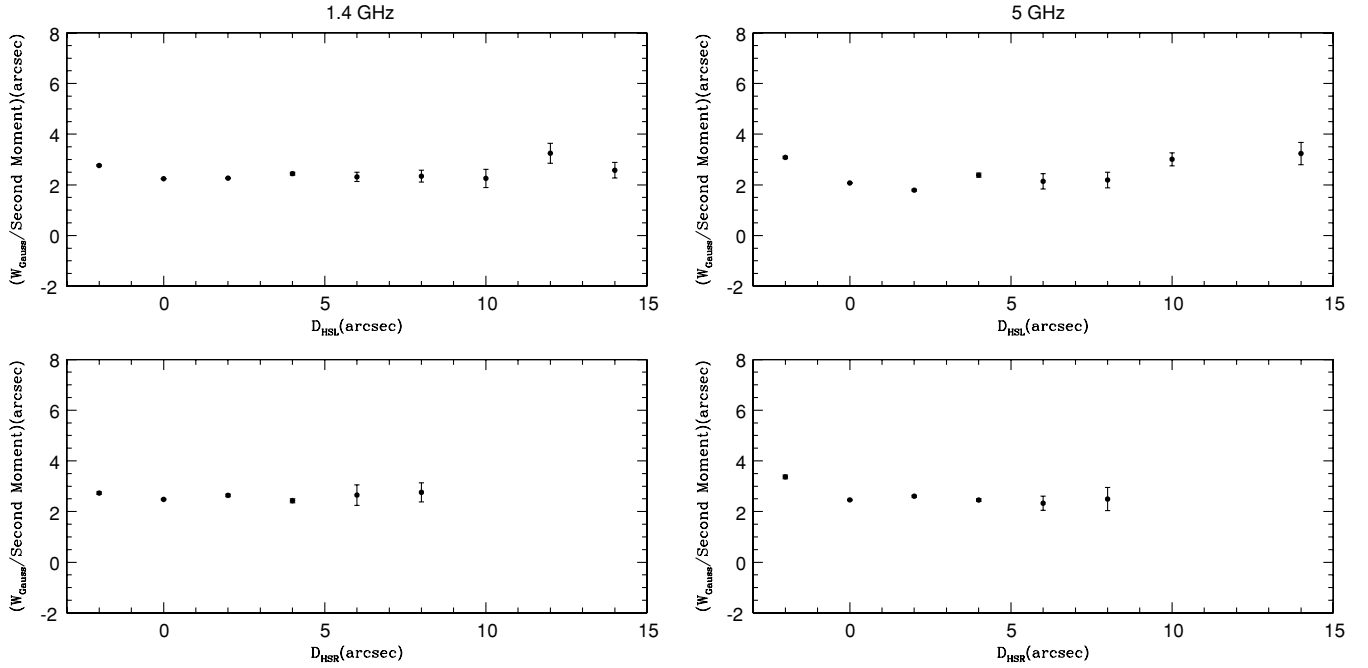


**Figure 33.** 3C41 ratio of the Gaussian FWHM to the second moment as a function of distance from the hot spot at 1.4 and 5 GHz (left and right panels, respectively) for the left- and right-hand sides of the source (top and bottom panels, respectively). The value of this ratio is fairly constant for each side of the source, and has a value of about 2. Similar results are obtained at 1.4 and 5 GHz.

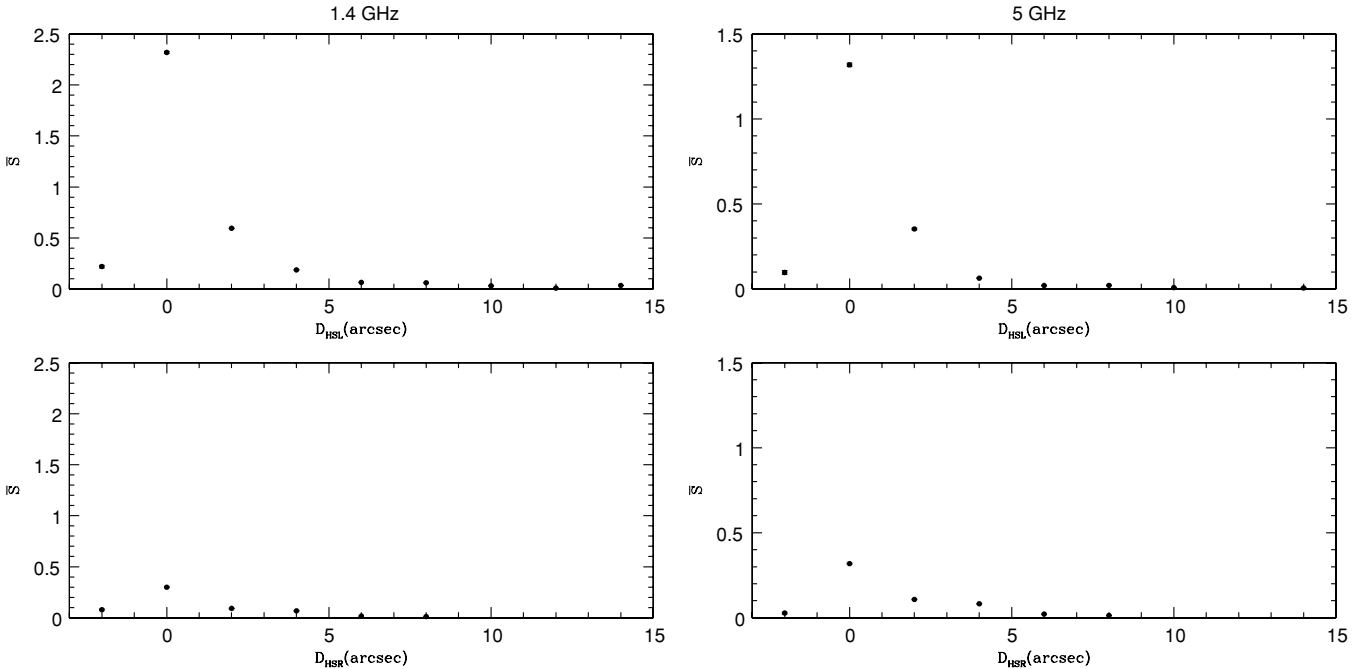


**Figure 34.** 3C41 average surface brightness in units of  $\text{Jy beam}^{-1}$  as a function of distance from the hot spot at 1.4 and 5 GHz (left and right panels, respectively) for the left- and right-hand sides of the source (top and bottom panels, respectively).

The minimum-energy magnetic field strength (Burbidge 1956) is obtained for each surface brightness profile slice using the expression  $B_{\min} = K_B B_M$ , where  $B_M$  is the magnetic field strength shown in the figures, and the normalization  $K_B$  is listed in Table 1 for  $B_M$  in the units shown. The magnetic field strength shown in the figures is obtained using the expression  $B_M = (\bar{S}/W_G)^{2/7}$ . The normalization factor  $K_B$  is obtained using the expression for the minimum-energy magnetic field strength presented by Miley (1980) assuming no relativistic protons, a volume filling factor of unity, and a spectral index of 0.7.

The minimum-energy pressure (Burbidge 1956) is obtained for each surface brightness slice using the expression  $P_{\min} = K_P P_M$ , where  $P_M$  is the pressure shown in the figures. This is obtained using the expression  $P_M = (\bar{S}/W_G)^{4/7}$ . The normalization factor  $K_P$  is obtained from  $K_B$  noting that the source pressure is  $P = [(4/3)b^{-1.5} + b^2]B_{\min}^2/(24\pi)$ , where  $b$  represents the offset of the magnetic field strength  $B$  from the minimum-energy field,  $b \equiv B/B_{\min}$ , taken here to be unity. Values of  $K_P$  are listed in Table 1 for  $P_M$  in the units shown in the figures.

All three quantities,  $\bar{S}$ ,  $B_{\min}$ , and  $P_{\min}$ , peak in the vicinity of the hot spot, have a region where each steadily decreases across

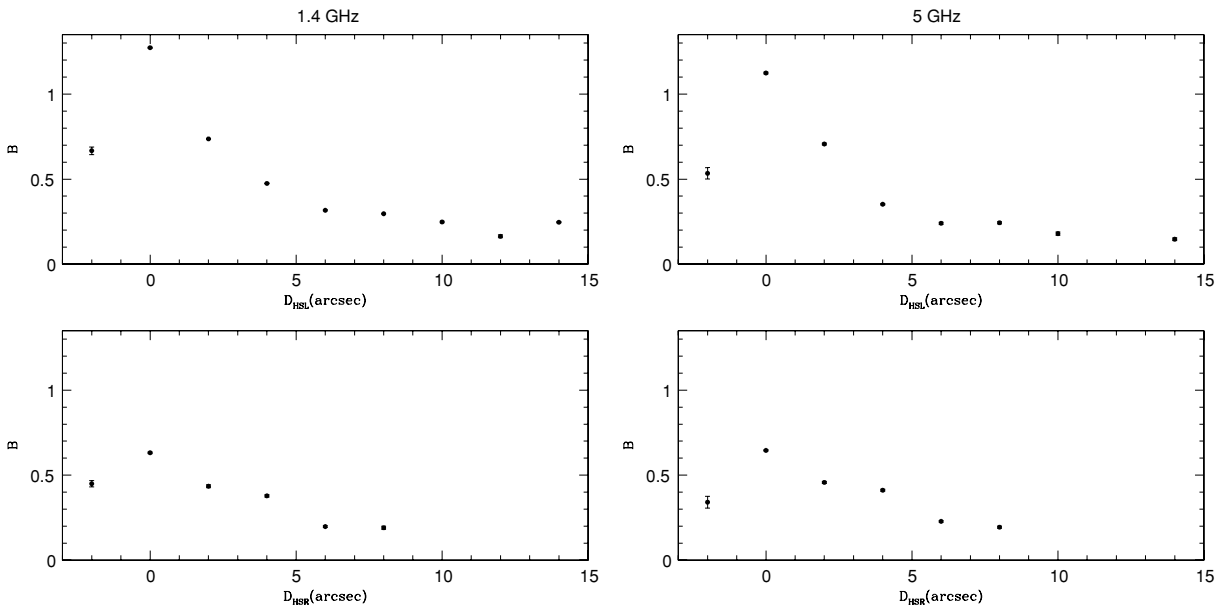


**Figure 35.** 3C41 minimum-energy magnetic field strength as a function of distance from the hot spot at 1.4 and 5 GHz (left and right panels, respectively) for the left- and right-hand sides of the source (top and bottom panels, respectively). The normalization is given in Table 1.

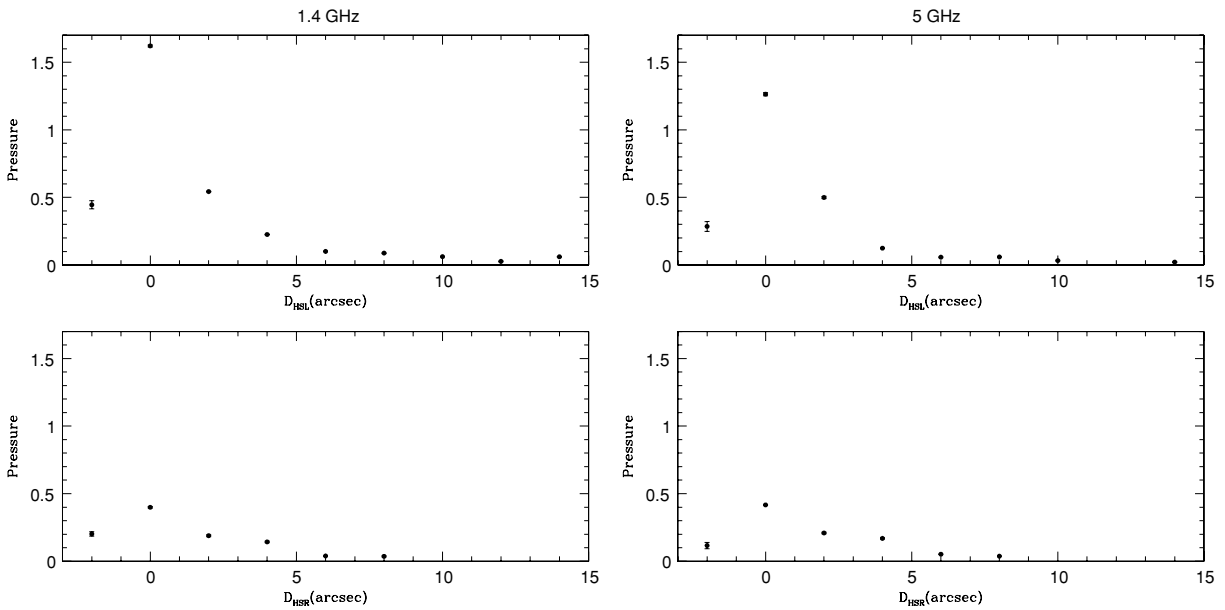


**Figure 36.** 3C41 minimum-energy pressure as a function of distance from the hot spot at 1.4 and 5 GHz (left and right panels, respectively) for the left- and right-hand sides of the source (top and bottom panels, respectively), as in Figure 12. The normalization is given in Table 1.

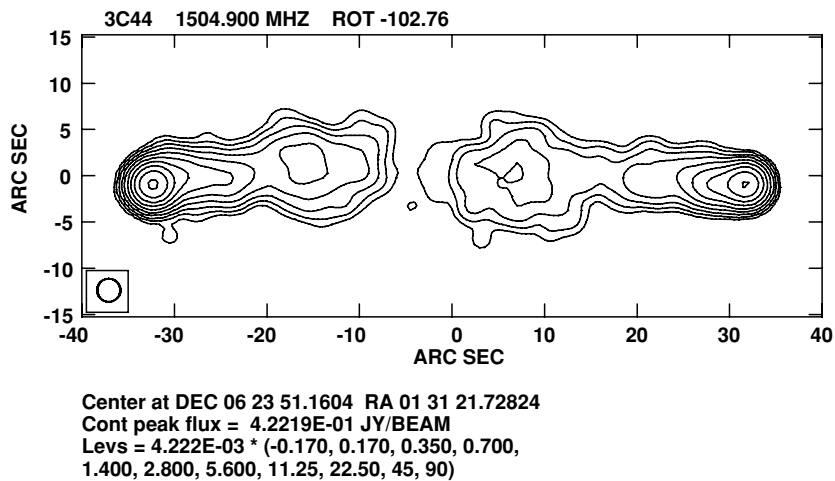


**Figure 37.** 3C44 at 1.4 GHz and 2.5 resolution rotated by 102.76 degrees clockwise, as in Figure 1.

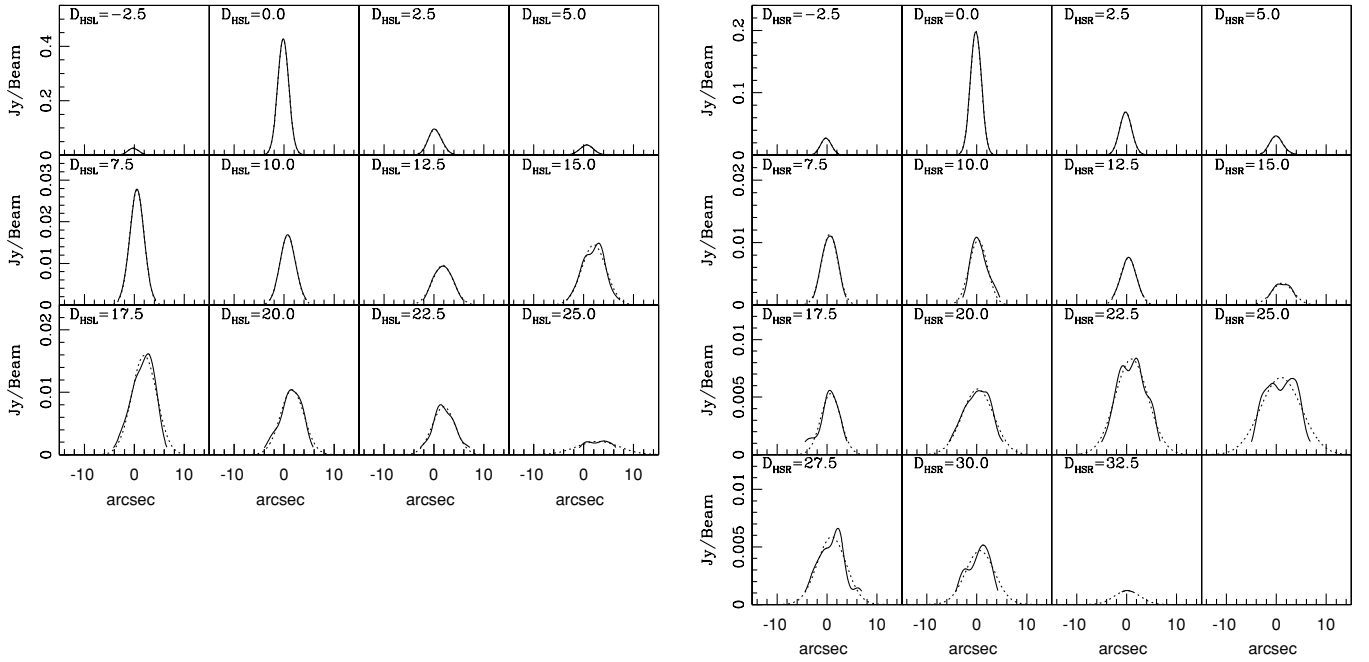


**Figure 38.** 3C44 surface brightness (solid line) and best-fit Gaussian (dotted line) for each cross-sectional slice of the radio bridge at 1.4 GHz, as in Figure 2. A Gaussian provides an excellent description of the surface brightness profile of each cross-sectional slice.

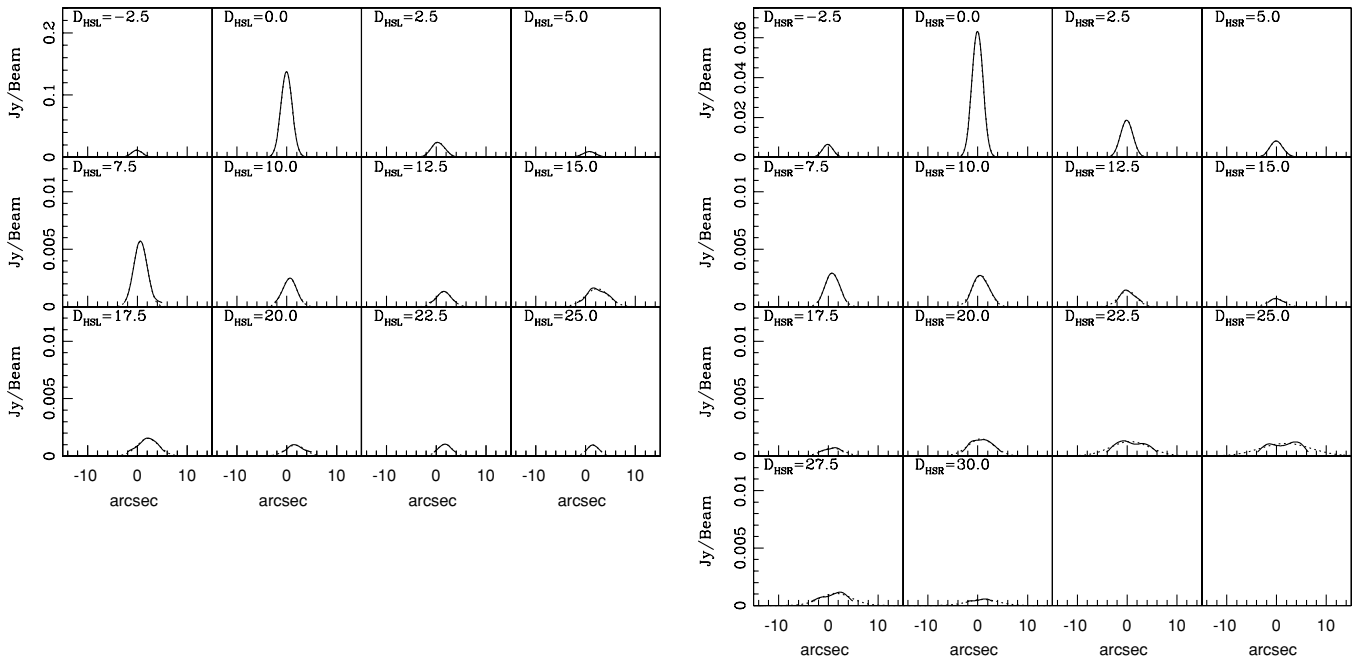


**Figure 39.** 3C44 surface brightness (solid line) and best-fit Gaussian (dotted line) for each cross-sectional slice of the radio bridge at 5 GHz, as in Figure 38 but at 5 GHz. Results obtained at 5 GHz are nearly identical to those obtained at 1.4 GHz.

the source away from the hot spot, and then level off to a roughly constant or very slowly declining value.

Interestingly, the location at which the pressure levels off and becomes roughly constant seems to be related to the location of the local maxima of the bridge width discussed in Section 2.1. Moving away from the hot spot, the pressure seems to level off just before the local maxima of the bridge width for 3C6.1, 3C34, 3C41, 3C44, the right side of 3C142.1, the left side of 3C169.1 (perhaps in two places), and 3C469.1. The effect is less obvious but may also be present for 3C54, 3C114, the left side of 3C142.1, and the left side of 3C441. The effect is not seen in 3C172 or the right side of 3C169.1,

and the pressure is not seen to level off for the right side of 3C441.

Thus, it would appear that in many sources the bridge width increases with distance from the hot spot and the pressure of the relativistic fluid in this region has strong gradients. Pressure waves propagating through the fluid tend to bring the pressure into equilibrium. Equilibrium is approached or reached near the location of the local maxima of the radio bridge width (and this approach to equilibrium is perhaps the reason that the bridge width does not continue to increase with distance from the hot spot). Sometimes the source overexpands at the local maxima of the bridge width, and a signature of this overexpansion could

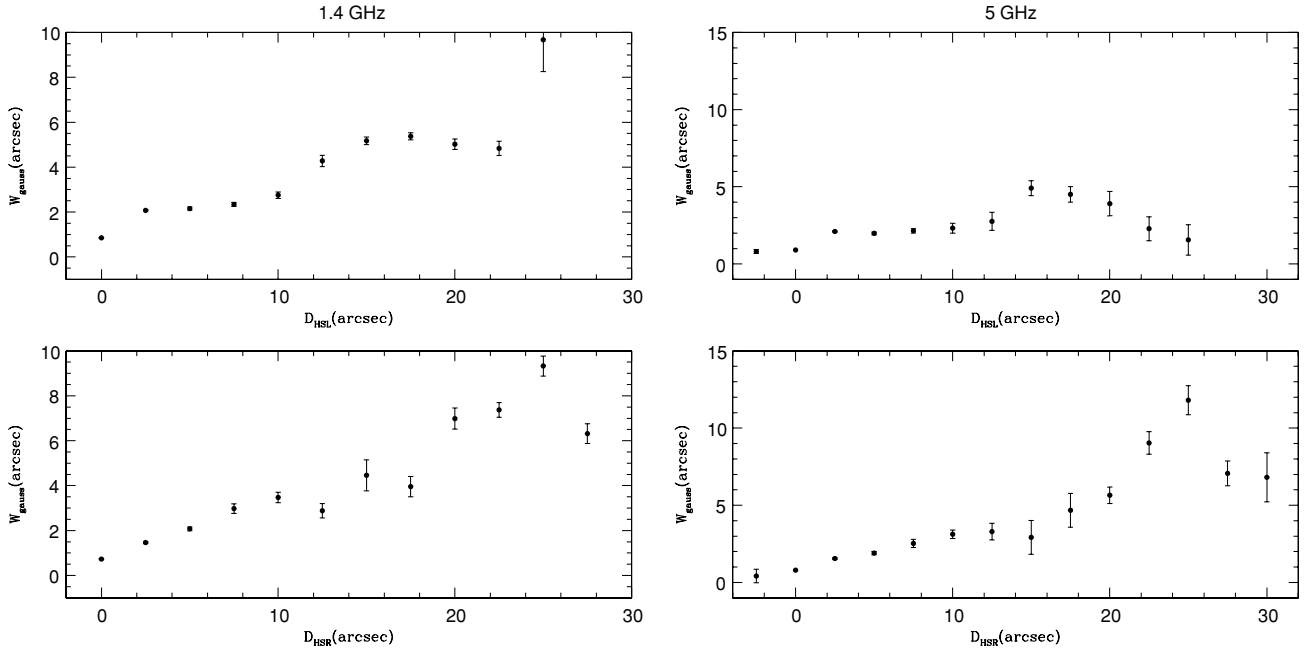


**Figure 40.** 3C44 Gaussian FWHM as a function of distance from the hot spot at 1.4 and 5 GHz (left and right panels, respectively) for the left- and right-hand sides of the source (top and bottom panels, respectively), as in Figure 4. The right- and left-hand sides of the source are fairly symmetric. Similar results are obtained at 1.4 and 5 GHz.

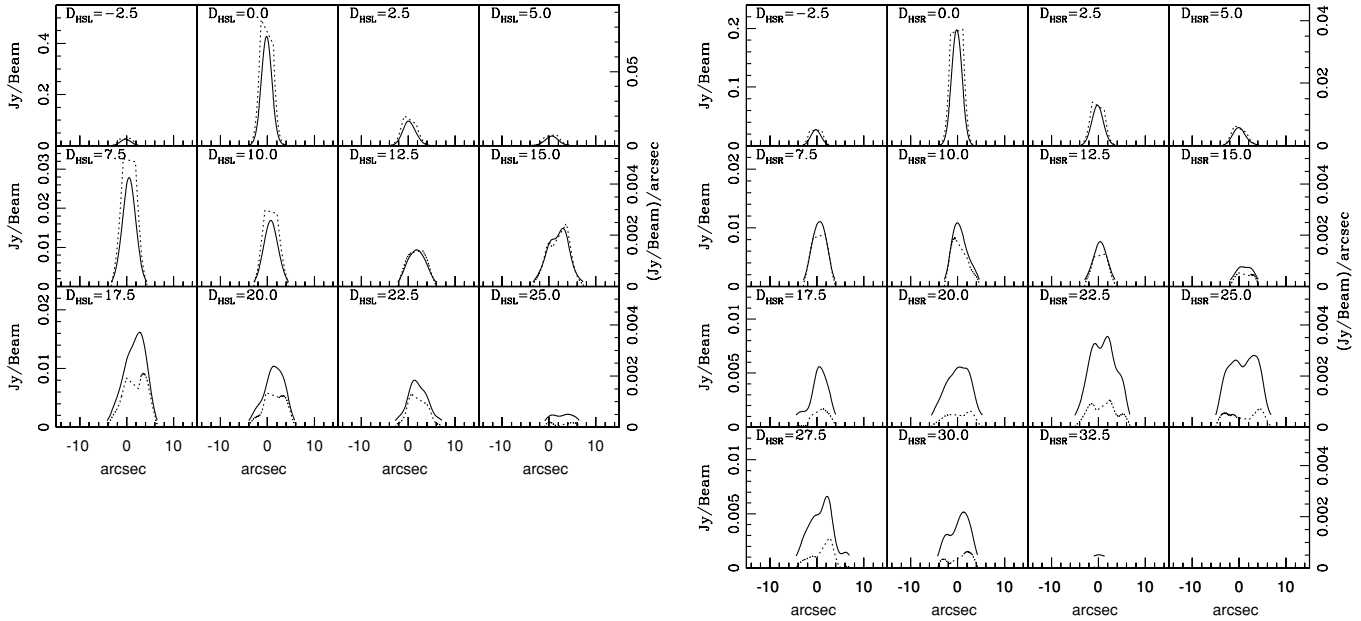


**Figure 41.** 3C44 emissivity (dotted line) and surface brightness (solid line) for each cross-sectional slice of the radio bridge at 1.4 GHz, as in Figure 5. A constant volume emissivity per slice provides a reasonable description of the data over most of the source.

be emissivity and pressure slice profiles that are “edge-peaked” with a minimum near the symmetry axis of the lobe. Regions downstream of this point, which are further away from the hot spot, are in rough pressure equilibrium. Pressure waves propagate throughout the radio lobe region as indicated by fluctuations of the emissivity and pressure both within a slice and as seen by comparing emissivities of adjacent slices.

Effects which could cause apparent fluctuations of pressure across a slice are deviations of the magnetic field strength from minimum-energy conditions or a non-semi-cylindrically symmetric slice, as discussed in Section 2.2. It is interesting that the emissivity obtained independently by stepping in from the top and bottom of the slice match in most slices, suggesting

that semi-cylindrical symmetry is a good approximation for most slices, and that the pressure fluctuations seen across most slices are rather modest.

### 3. SUMMARY AND CONCLUSIONS

The radio lobes of a sample of 11 very powerful classical double radio galaxies were studied in detail. Each source was rotated so that the line connecting the hot spots was horizontal. Vertical cross-sectional cuts separated by one beam width of the radio surface brightness were taken beginning at the hot spot of each side of each source and moving in toward the source center.

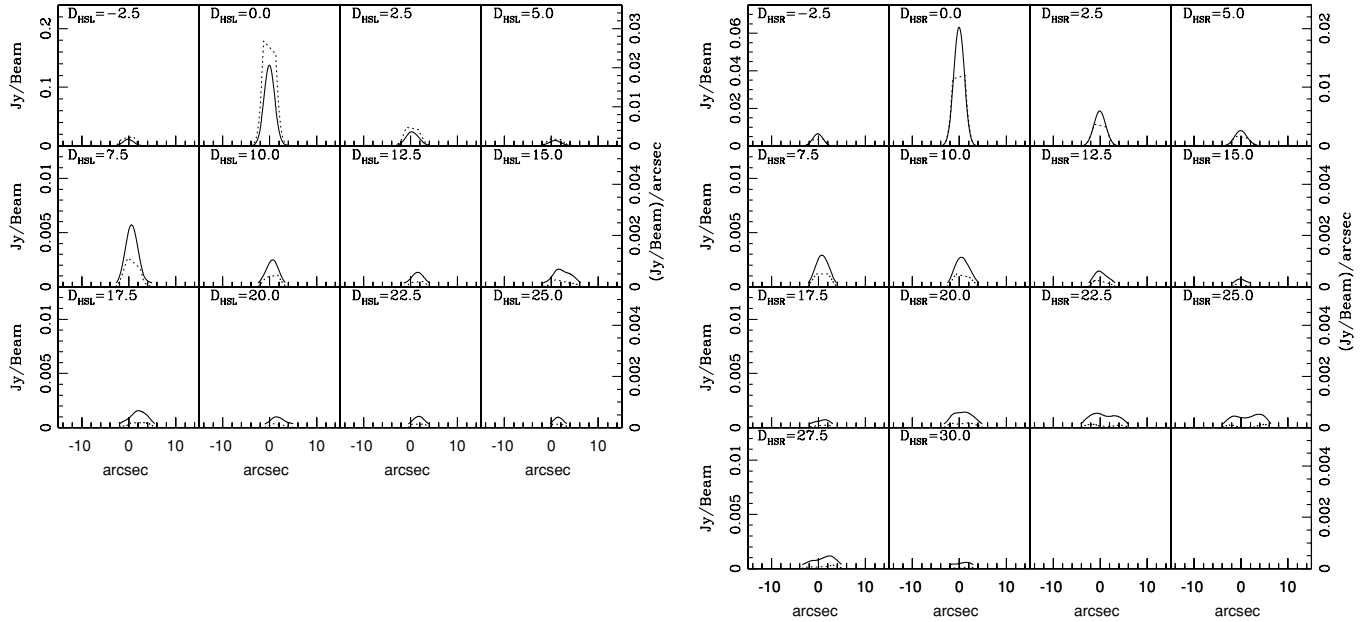


**Figure 42.** 3C44 emissivity (dotted line) and surface brightness (solid line) for each cross-sectional slice of the radio bridge at 5 GHz, as in Figure 41 but at 5 GHz. Results obtained at 5 GHz are nearly identical to those obtained at 1.4 GHz.

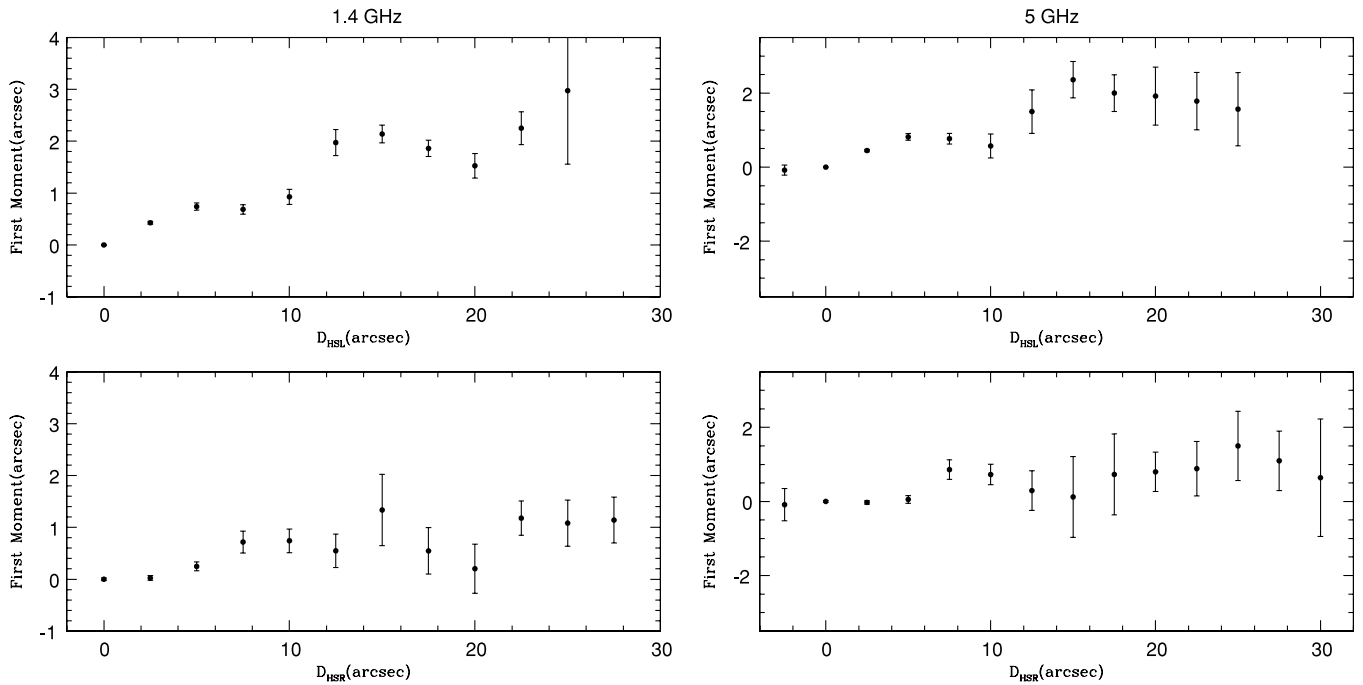


**Figure 43.** 3C44 first moment as a function of distance from the hot spot at 1.4 GHz and 5 GHz (left and right panels, respectively) for the left- and right-hand sides of the source (top and bottom, respectively).

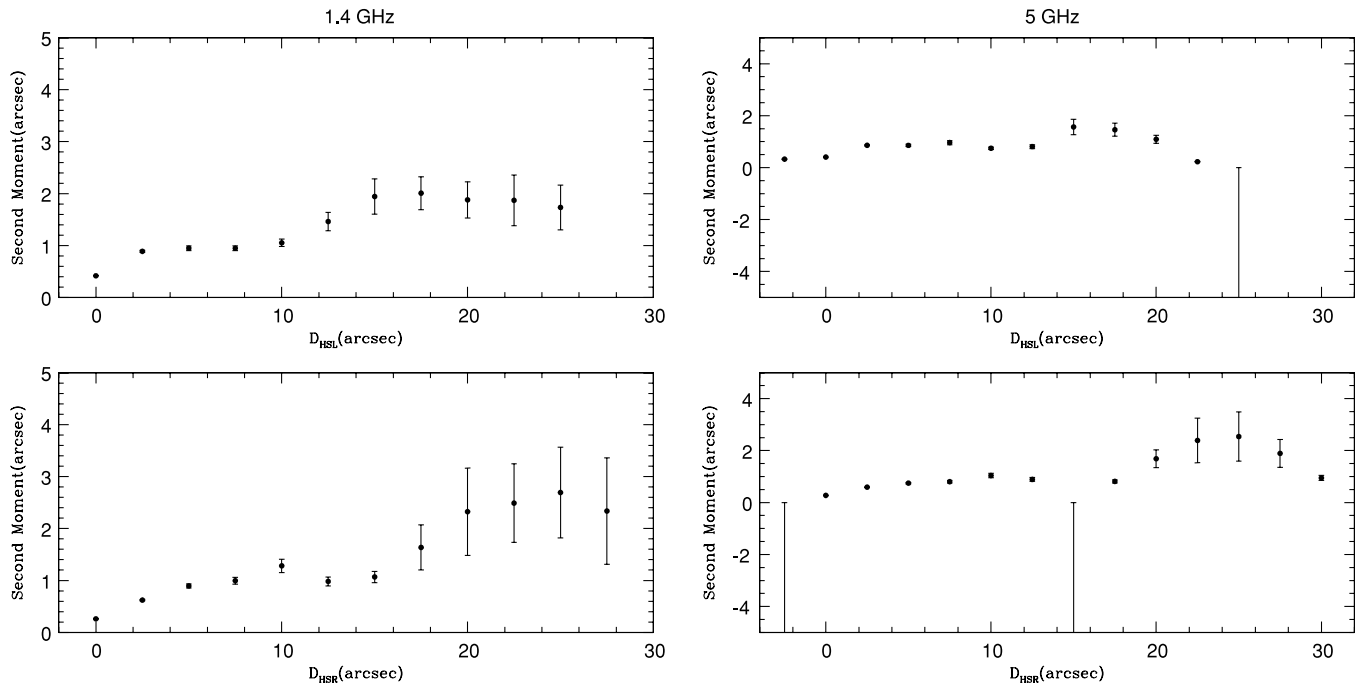


**Figure 44.** 3C44 second moment as a function of distance from the hot spot at 1.4 GHz and 5 GHz (left and right panels, respectively) for the left and right sides of the source (top and bottom panels, respectively).

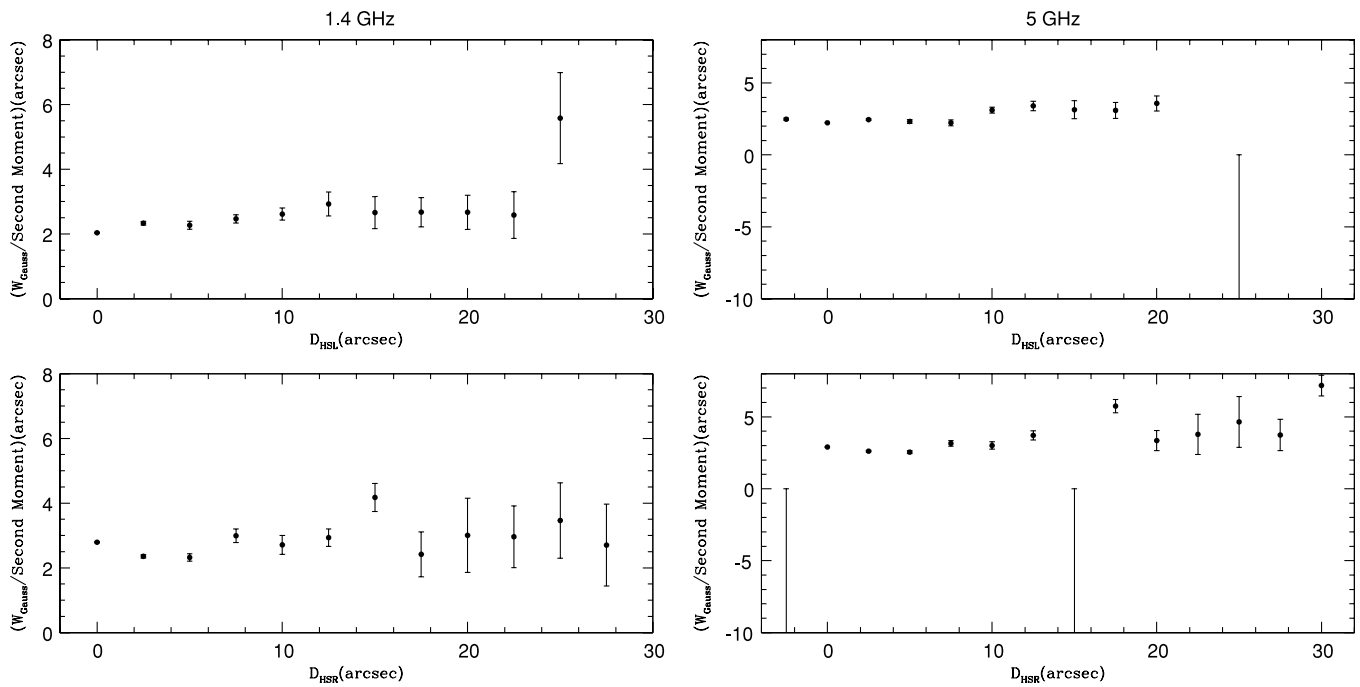


**Figure 45.** 3C44 ratio of the Gaussian FWHM to the second moment as a function of distance from the hot spot at 1.4 and 5 GHz (left and right panels, respectively) for the left- and right-hand sides of the source (top and bottom panels, respectively). The value of this ratio is fairly constant for each side of the source, and has a value of about 2. Similar results are obtained at 1.4 and 5 GHz.

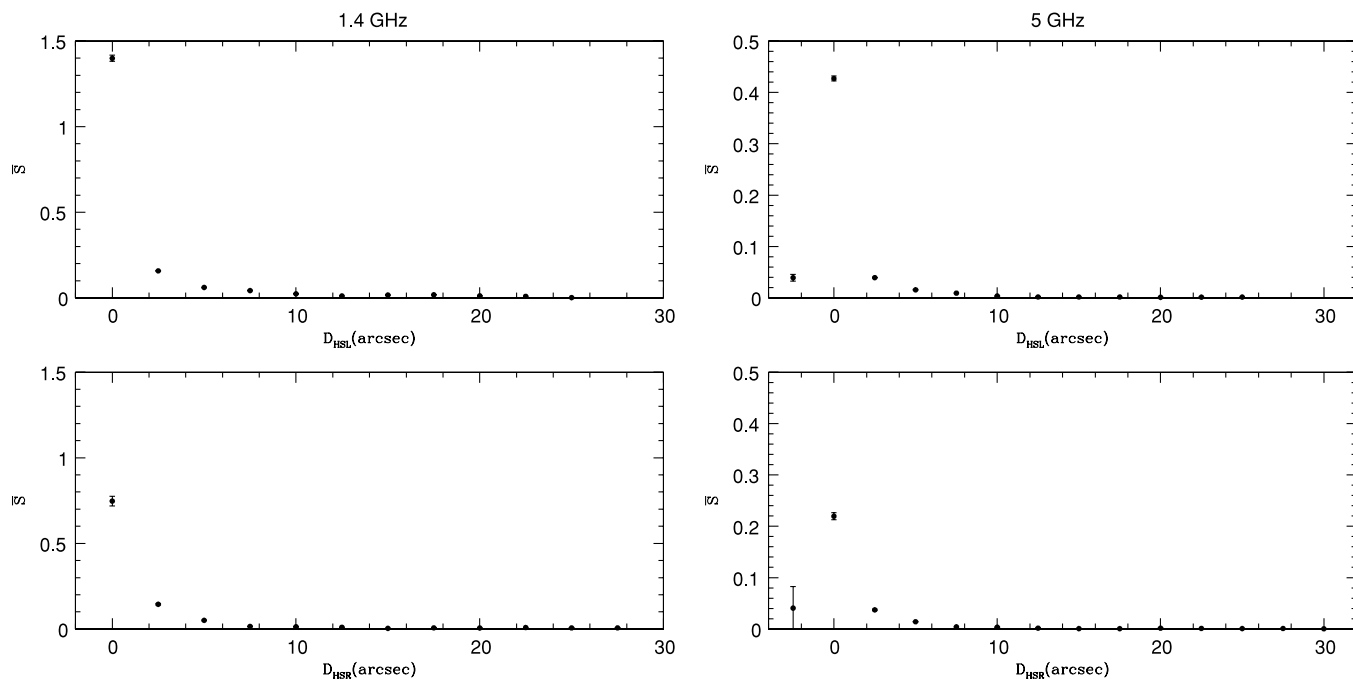


**Figure 46.** 3C44 average surface brightness in units of  $\text{Jy beam}^{-1}$  as a function of distance from the hot spot at 1.4 and 5 GHz (left and right panels, respectively) for the left- and right-hand sides of the source (top and bottom panels, respectively).

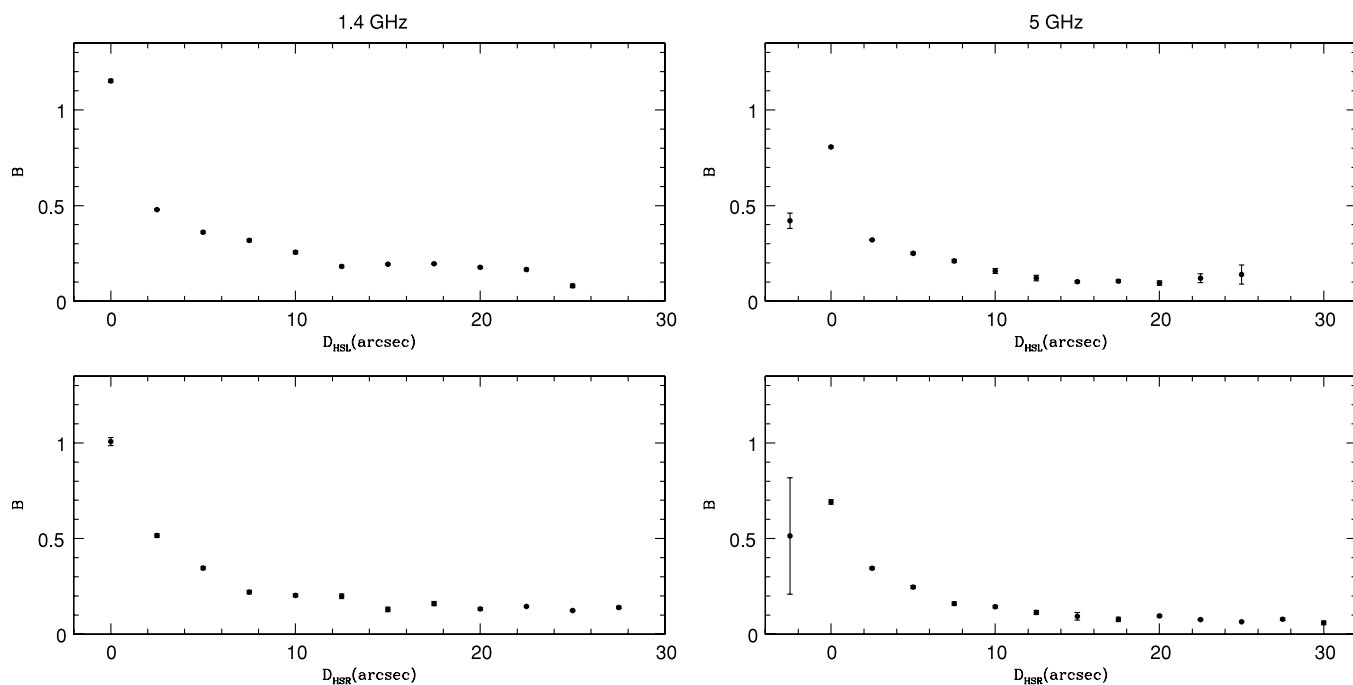


**Figure 47.** 3C44 minimum-energy magnetic field strength as a function of distance from the hot spot at 1.4 and 5 GHz (left and right panels, respectively) for the left- and right-hand sides of the source (top and bottom panels, respectively). The normalization is given in Table 1.

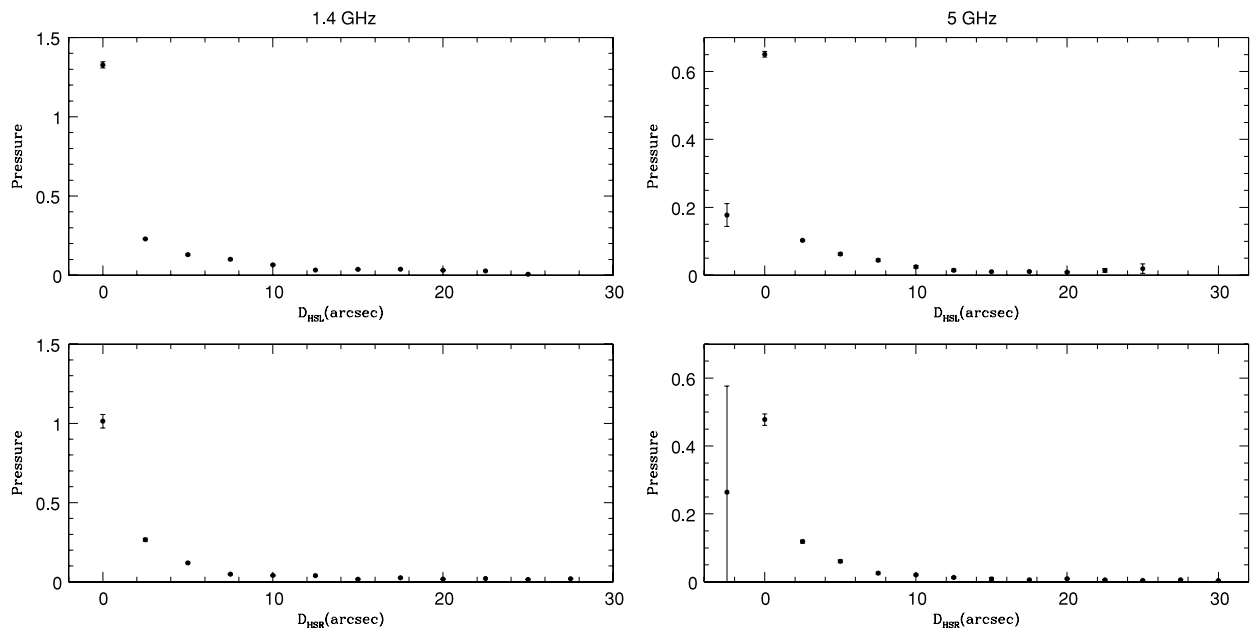


**Figure 48.** 3C44 minimum-energy pressure as a function of distance from the hot spot at 1.4 and 5 GHz (left and right panels, respectively) for the left- and right-hand sides of the source (top and bottom panels, respectively), as in Figure 12. The normalization is given in Table 1.

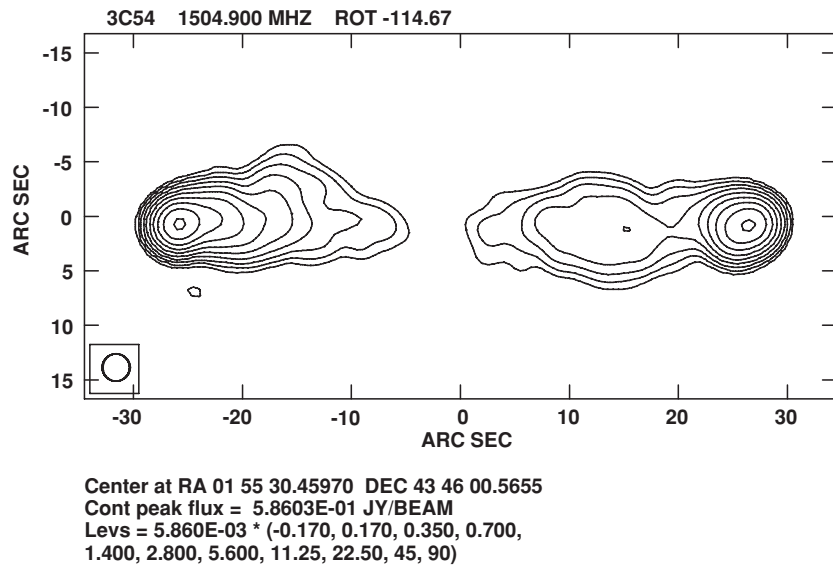


**Figure 49.** 3C54 at 1.4 GHz and 2'' resolution rotated by 114.67 clockwise, as in Figure 1.

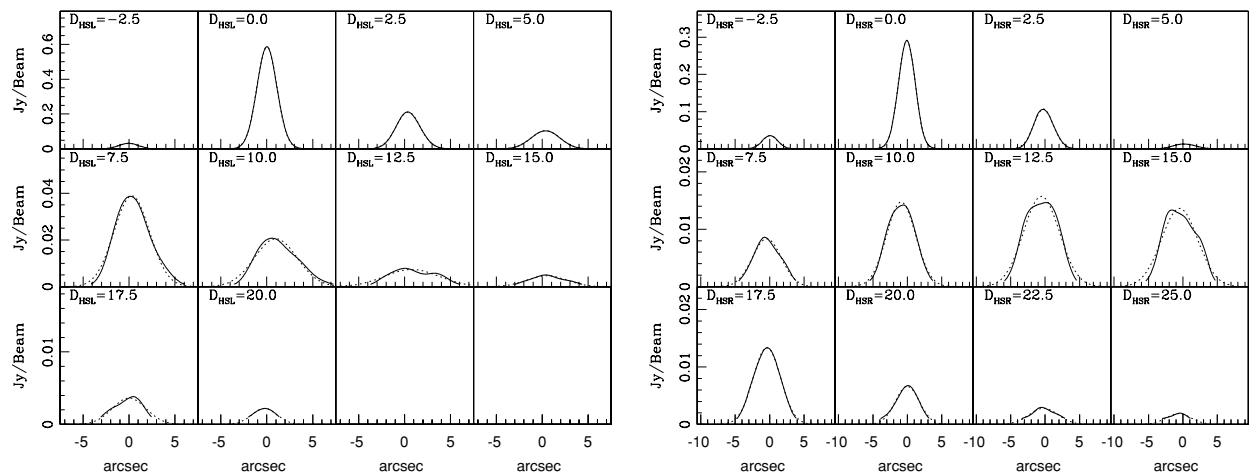


**Figure 50.** 3C54 surface brightness (solid line) and best-fit Gaussian (dotted line) for each cross-sectional slice of the radio bridge at 1.4 GHz, as in Figure 2. A Gaussian provides an excellent description of the surface brightness profile of each cross-sectional slice.

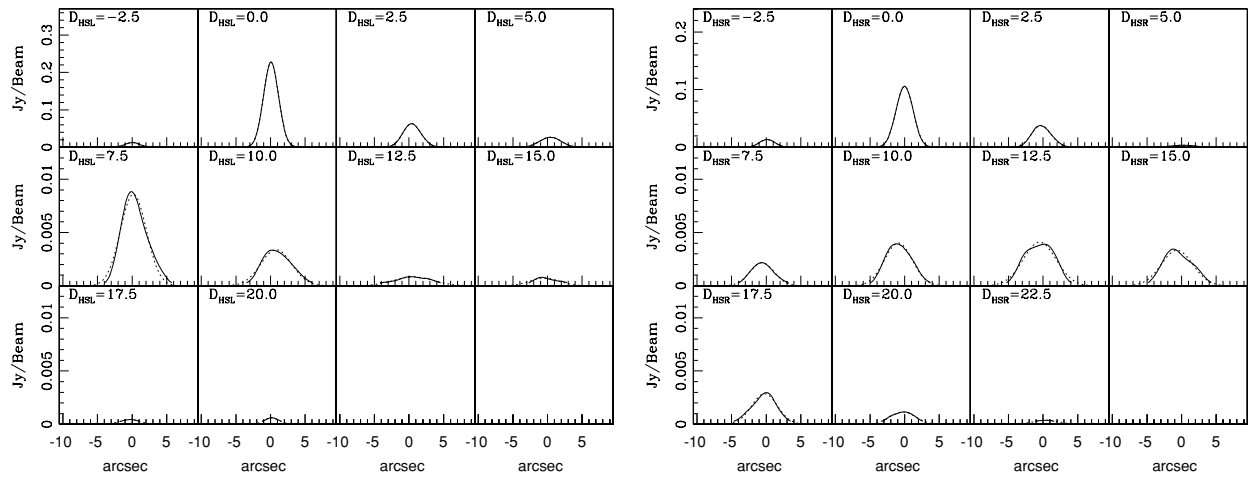


**Figure 51.** 3C54 surface brightness (solid line) and best-fit Gaussian (dotted line) for each cross-sectional slice of the radio bridge at 5 GHz, as in Figure 50 but at 5 GHz. Results obtained at 5 GHz are nearly identical to those obtained at 1.4 GHz.

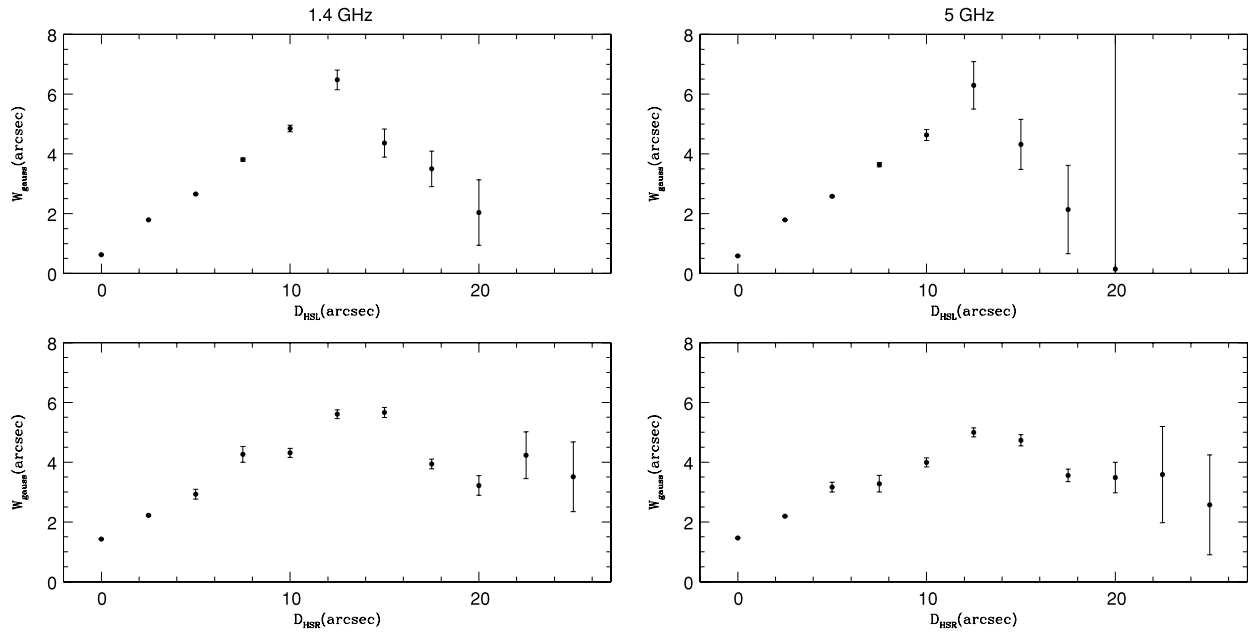


**Figure 52.** 3C54 Gaussian FWHM as a function of distance from the hot spot at 1.4 and 5 GHz (left and right panels, respectively) for the left- and right-hand sides of the source (top and bottom panels, respectively), as in Figure 4. The right- and left-hand sides of the source are quite symmetric. Similar results are obtained at 1.4 and 5 GHz.

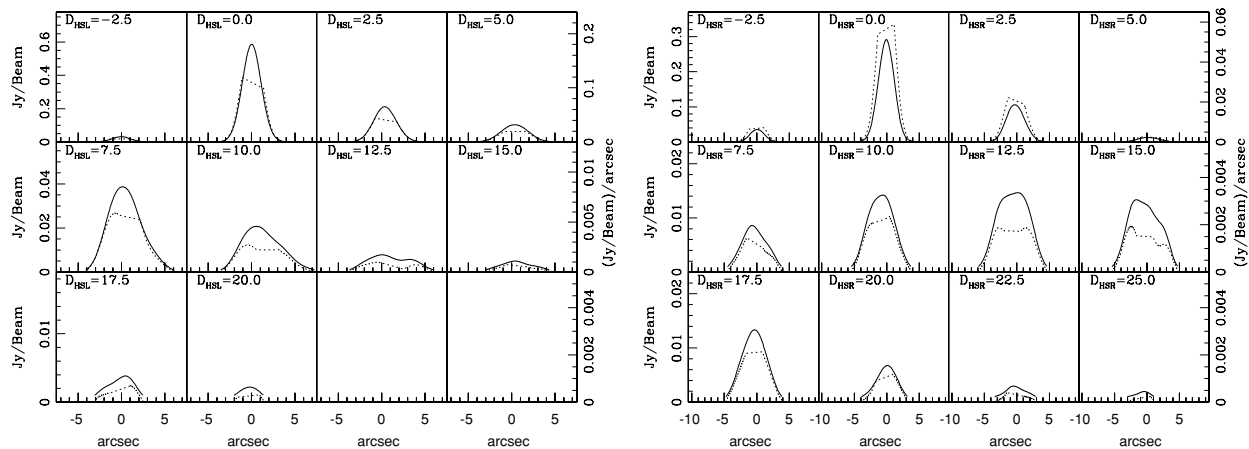


**Figure 53.** 3C54 emissivity (dotted line) and surface brightness (solid line) for each cross-sectional slice of the radio bridge at 1.4 GHz, as in Figure 5. A constant volume emissivity per slice provides a reasonable description of the data over most of the source.

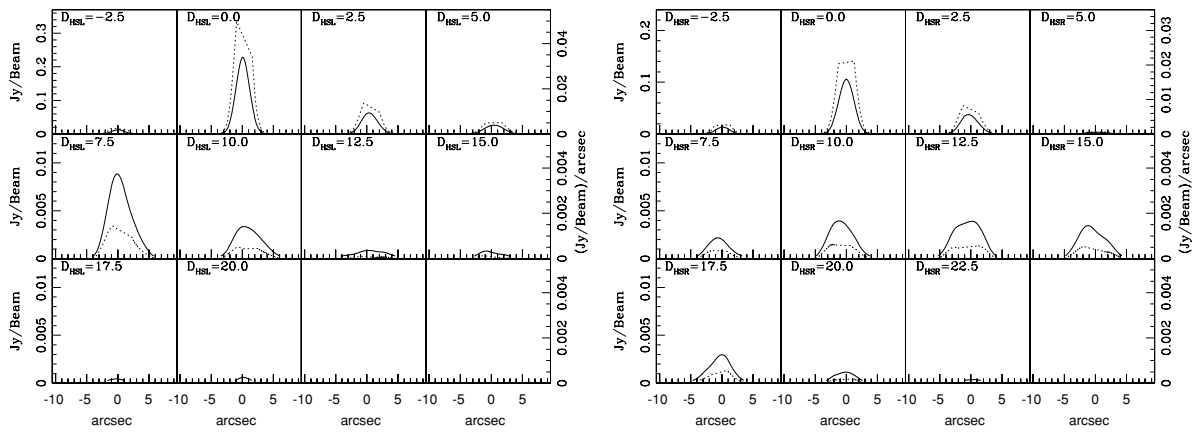


**Figure 54.** 3C54 emissivity (dotted line) and surface brightness (solid line) for each cross-sectional slice of the radio bridge at 5 GHz, as in Figure 53 but at 5 GHz. Results obtained at 5 GHz are nearly identical to those obtained at 1.4 GHz.

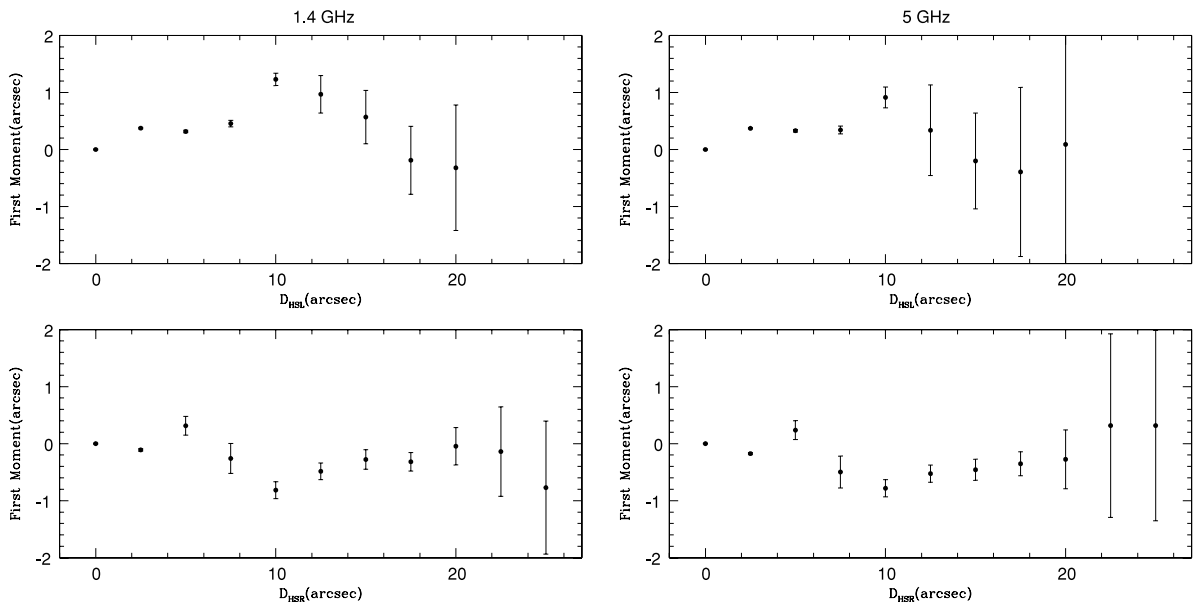


**Figure 55.** 3C54 first moment as a function of distance from the hot spot at 1.4 GHz and 5 GHz (left and right panels, respectively) for the left- and right-hand sides of the source (top and bottom, respectively).

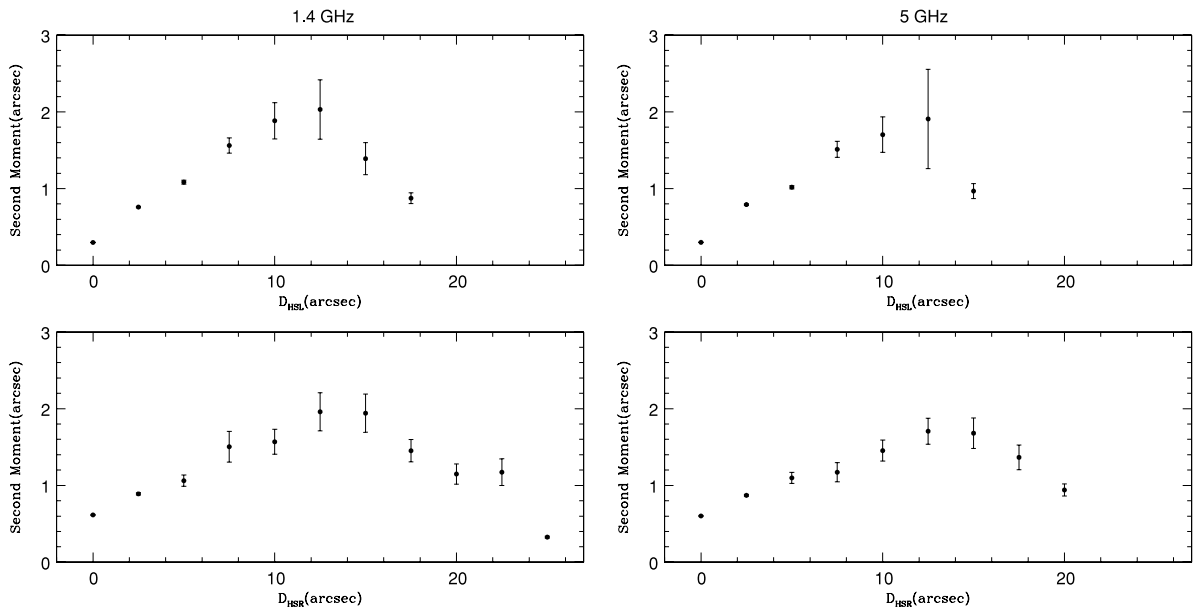


**Figure 56.** 3C54 second moment as a function of distance from the hot spot at 1.4 GHz and 5 GHz (left and right panels, respectively) for the left and right sides of the source (top and bottom panels, respectively).

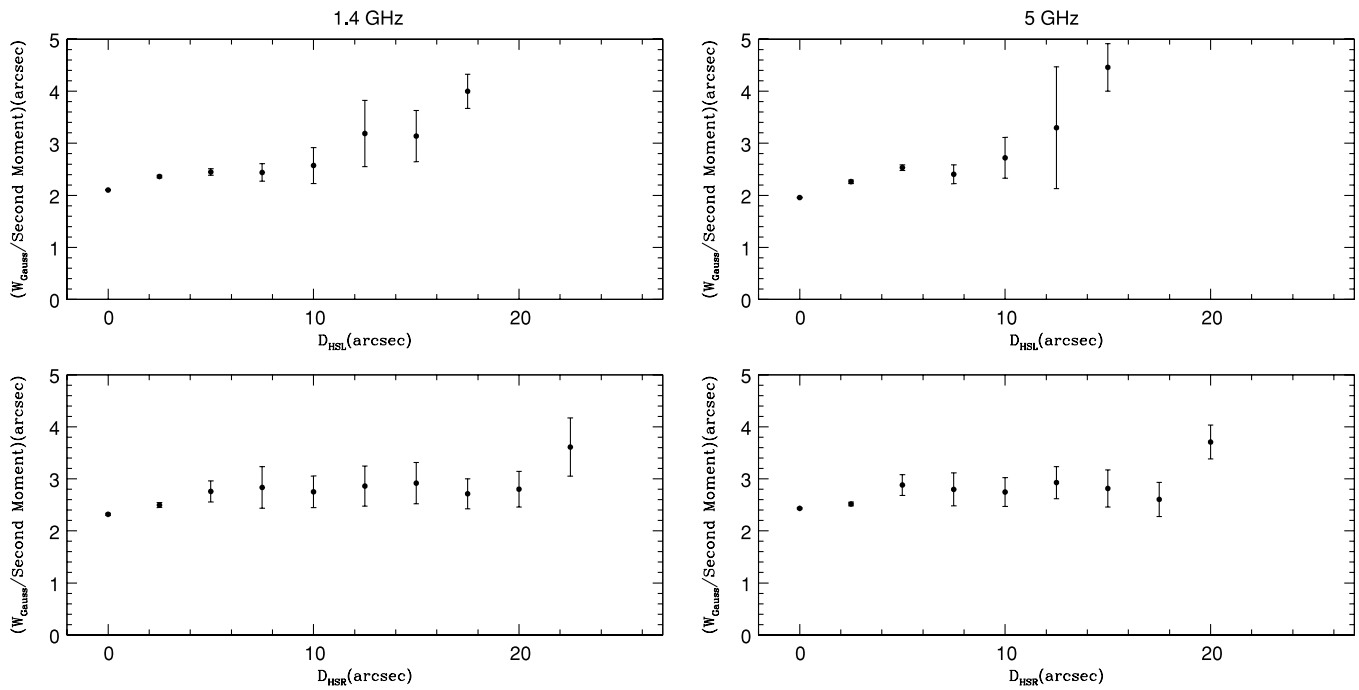


**Figure 57.** 3C54 ratio of the Gaussian FWHM to the second moment as a function of distance from the hot spot at 1.4 and 5 GHz (left and right panels, respectively) for the left- and right-hand sides of the source (top and bottom panels, respectively). The value of this ratio is fairly constant for each side of the source, and has a value of about 2–2.5. Similar results are obtained at 1.4 and 5 GHz.

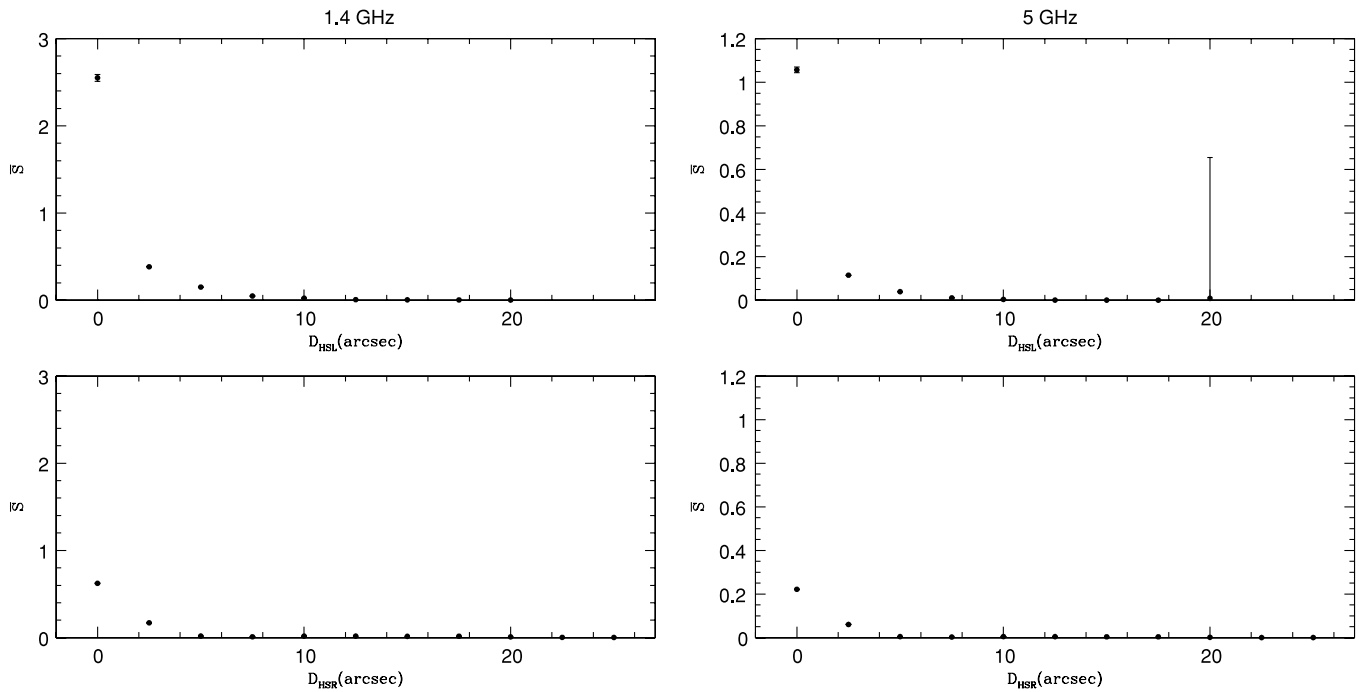


**Figure 58.** 3C54 average surface brightness in units of  $\text{Jy beam}^{-1}$  as a function of distance from the hot spot at 1.4 and 5 GHz (left and right panels, respectively) for the left- and right-hand sides of the source (top and bottom panels, respectively).

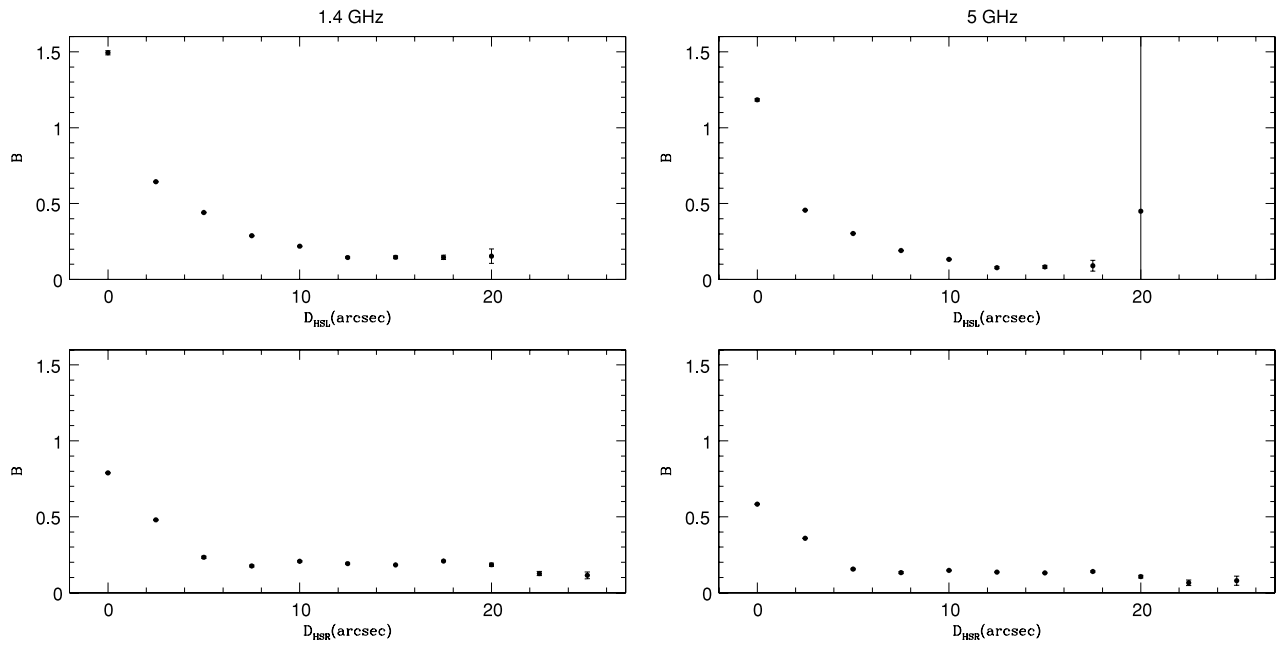


**Figure 59.** 3C54 minimum-energy magnetic field strength as a function of distance from the hot spot at 1.4 and 5 GHz (left and right panels, respectively) for the left- and right-hand sides of the source (top and bottom panels, respectively). The normalization is given in Table 1.

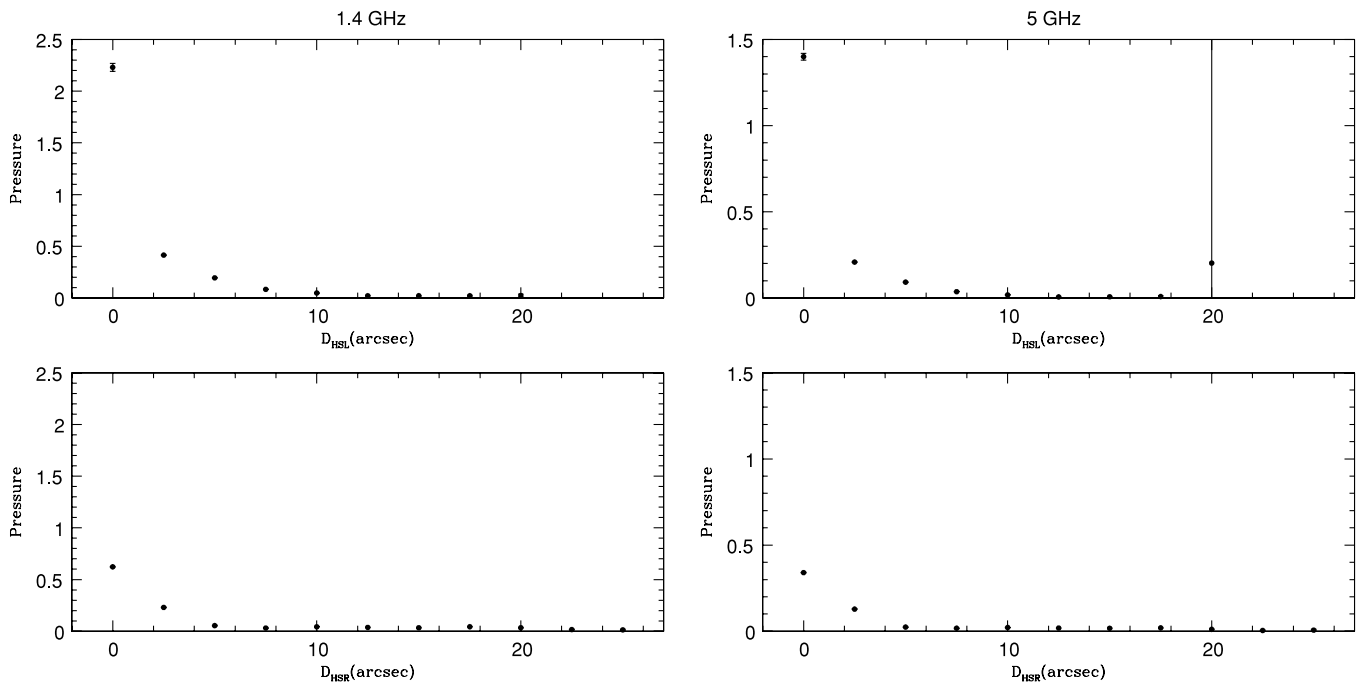


**Figure 60.** 3C54 minimum-energy pressure as a function of distance from the hot spot at 1.4 and 5 GHz (left and right panels, respectively) for the left- and right-hand sides of the source (top and bottom panels, respectively), as in Figure 12. The normalization is given in Table 1.

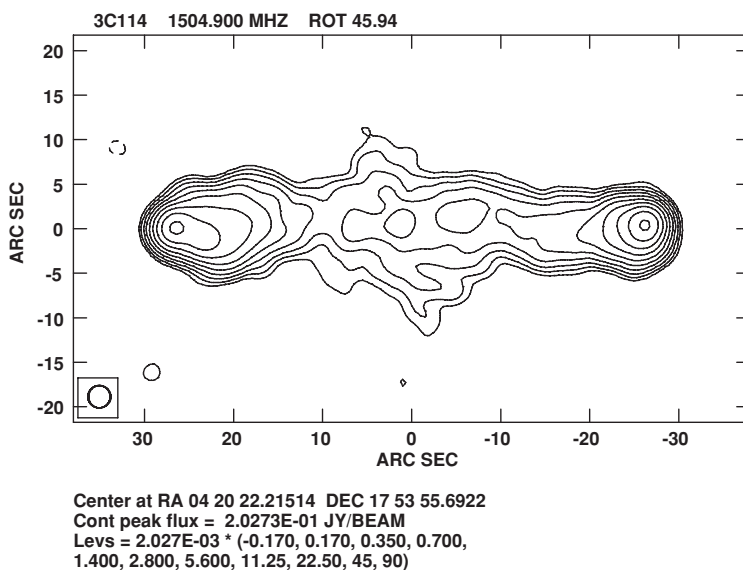


Figure 61. 3C114 at 1.4 GHz and 2.5 resolution rotated by 45.94 counterclockwise, as in Figure 1.

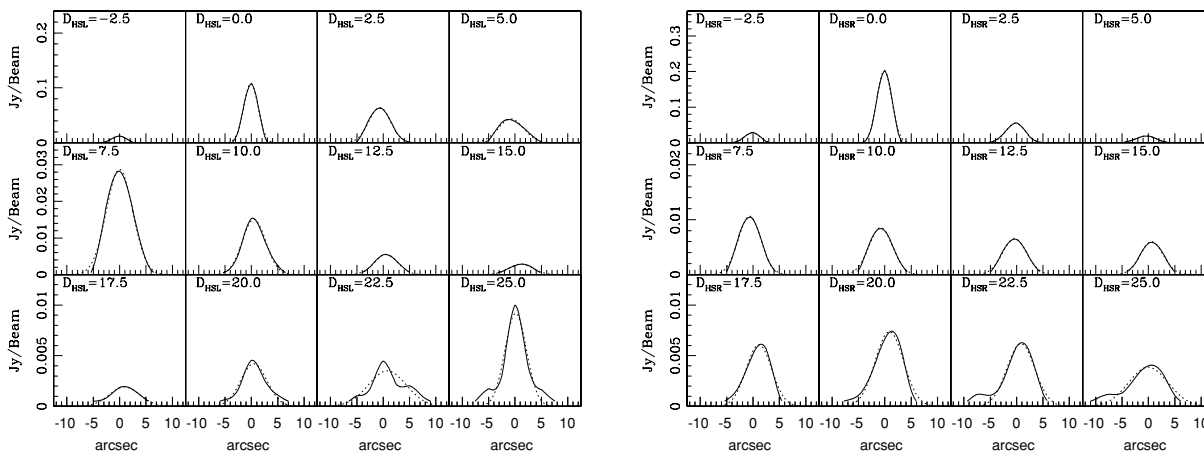


Figure 62. 3C114 surface brightness (solid line) and best-fit Gaussian (dotted line) for each cross-sectional slice of the radio bridge at 1.4 GHz, as in Figure 2. A Gaussian provides an excellent description of the surface brightness profile of each cross-sectional slice.

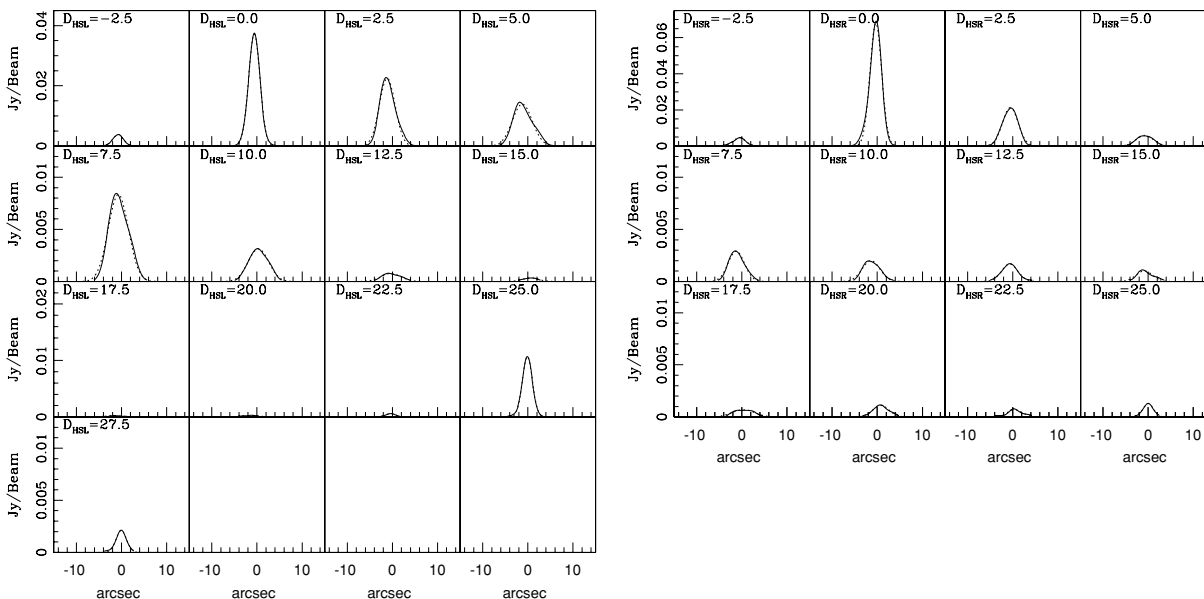
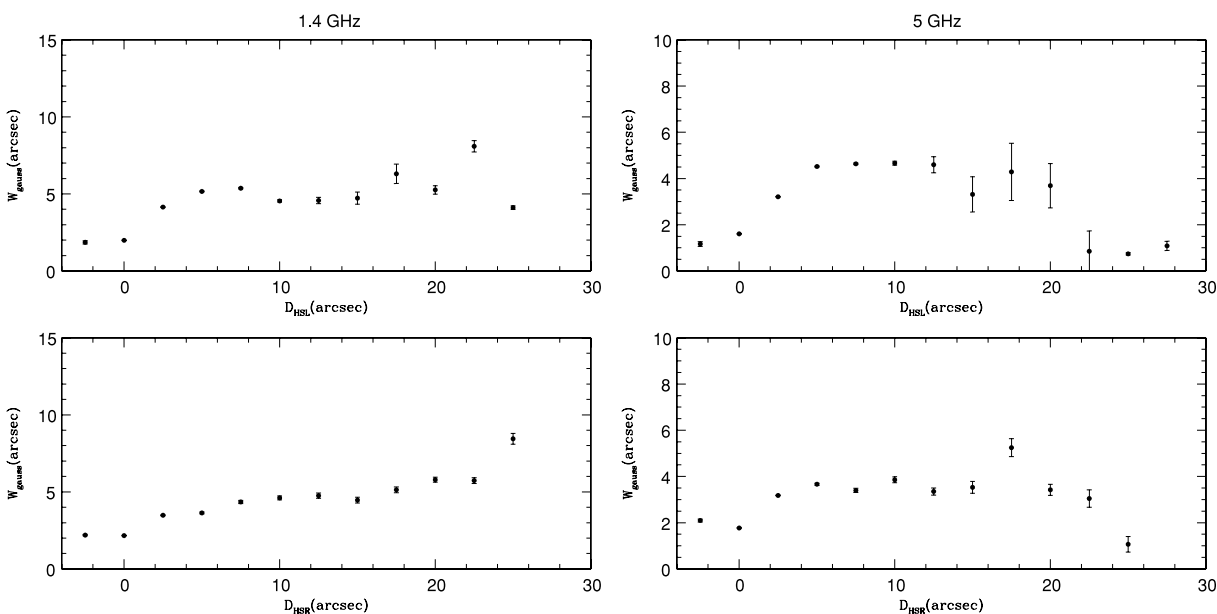
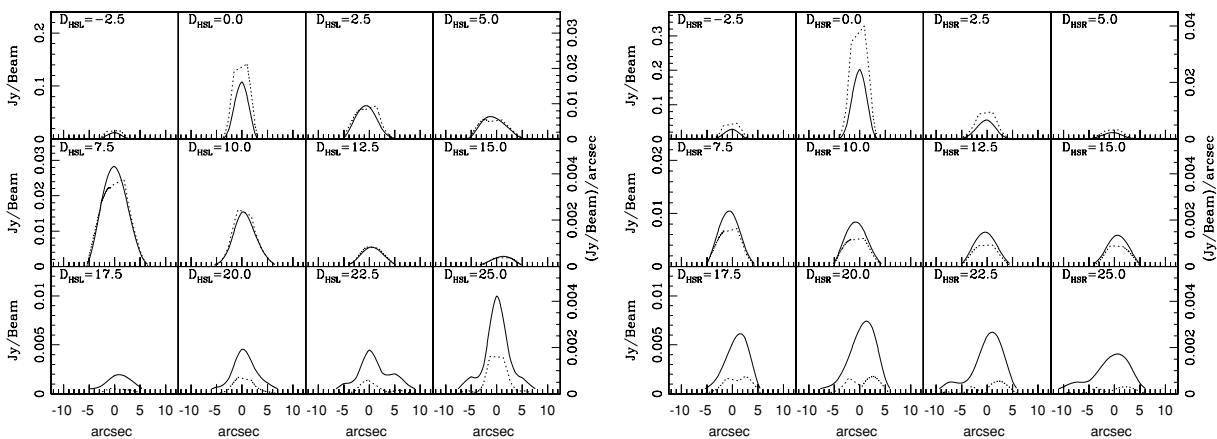


Figure 63. 3C114 surface brightness (solid line) and best-fit Gaussian (dotted line) for each cross-sectional slice of the radio bridge at 5 GHz, as in Figure 62 but at 5 GHz. Results obtained at 5 GHz are nearly identical to those obtained at 1.4 GHz.



**Figure 64.** 3C114 Gaussian FWHM as a function of distance from the hot spot at 1.4 and 5 GHz (left and right panels, respectively) for the left- and right-hand sides of the source (top and bottom panels, respectively), as in Figure 4. The right- and left-hand sides of the source are highly symmetric. Similar results are obtained at 1.4 and 5 GHz.



**Figure 65.** 3C114 emissivity (dotted line) and surface brightness (solid line) for each cross-sectional slice of the radio bridge at 1.4 GHz, as in Figure 5. A constant volume emissivity per slice provides a reasonable description of the data over most of the source.

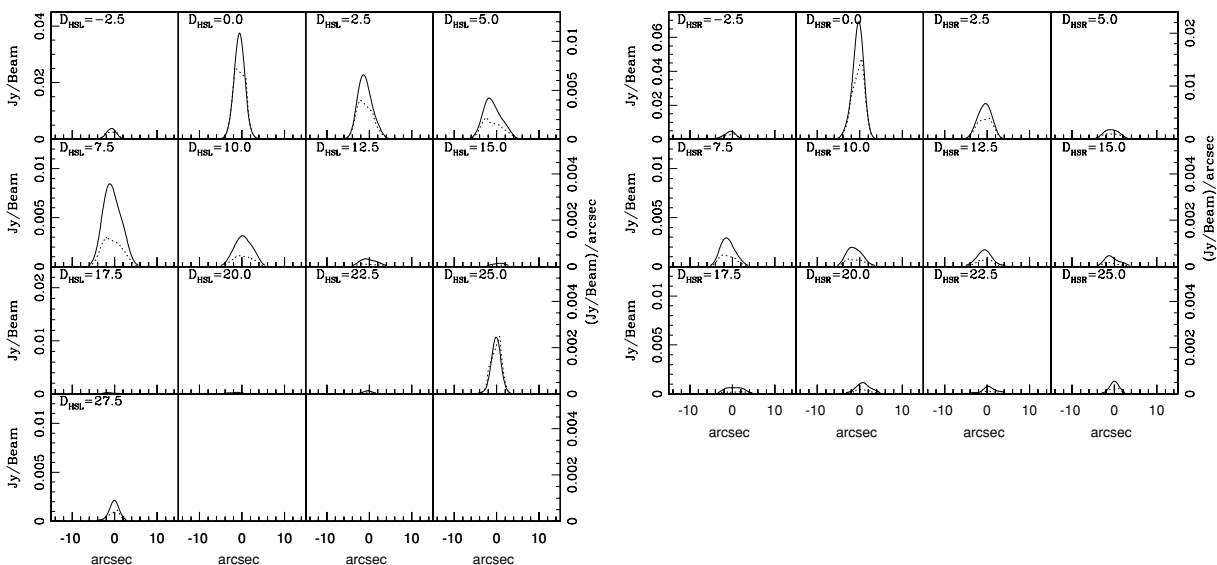


**Figure 66.** 3C114 emissivity (dotted line) and surface brightness (solid line) for each cross-sectional slice of the radio bridge at 5 GHz, as in Figure 65 but at 5 GHz. Results obtained at 5 GHz are nearly identical to those obtained at 1.4 GHz.

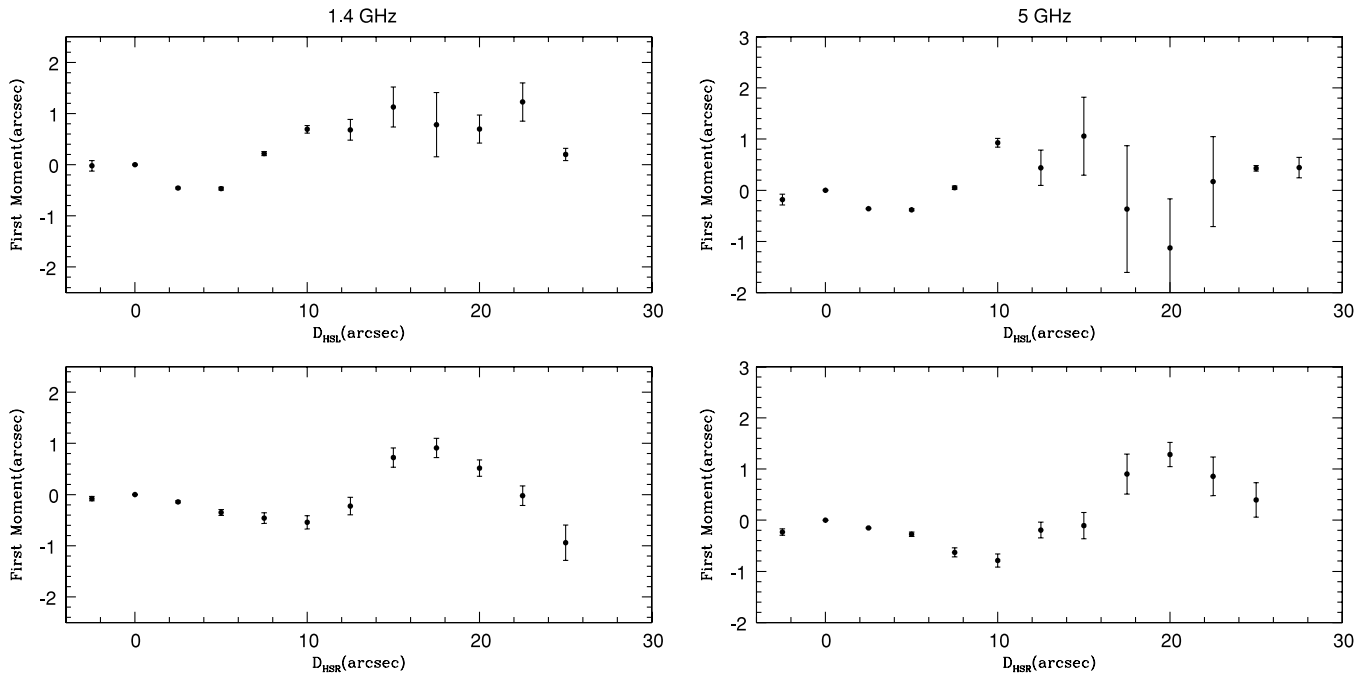


**Figure 67.** 3C114 first moment as a function of distance from the hot spot at 1.4 GHz and 5 GHz (left and right panels, respectively) for the left- and right-hand sides of the source (top and bottom, respectively).

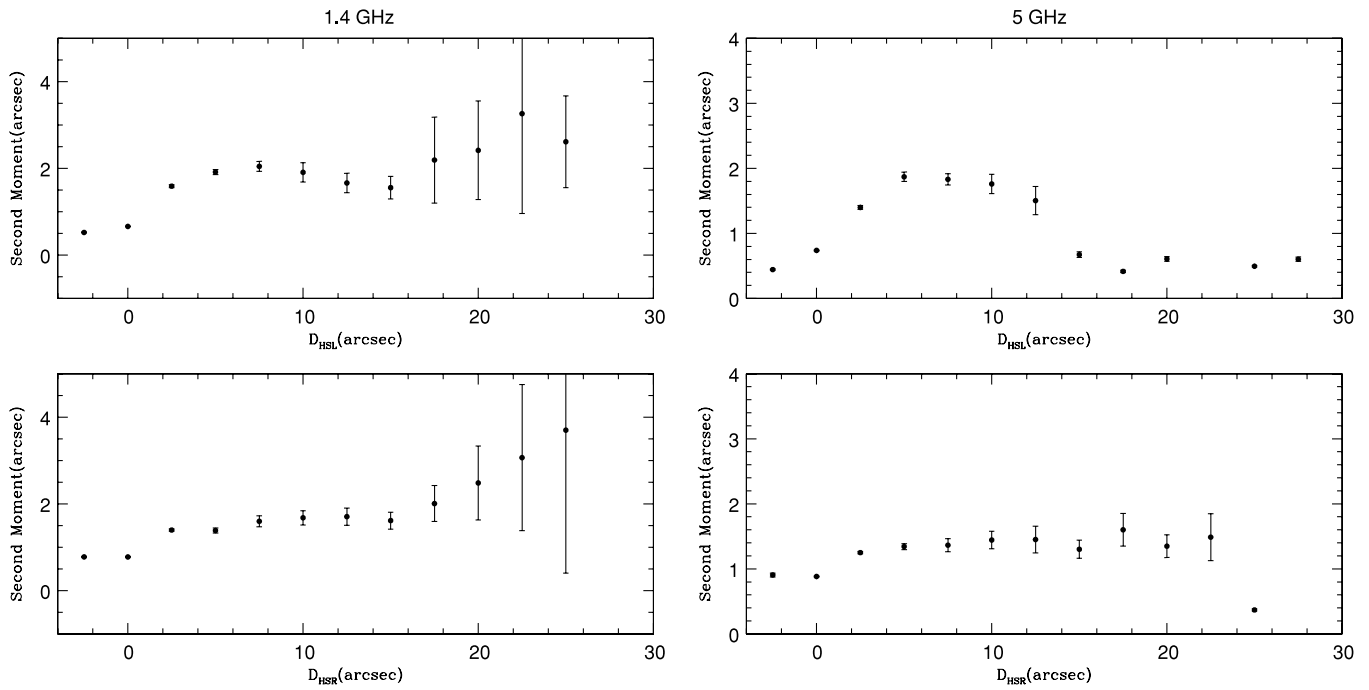


**Figure 68.** 3C114 second moment as a function of distance from the hot spot at 1.4 GHz and 5 GHz (left and right panels, respectively) for the left and right sides of the source (top and bottom panels, respectively).

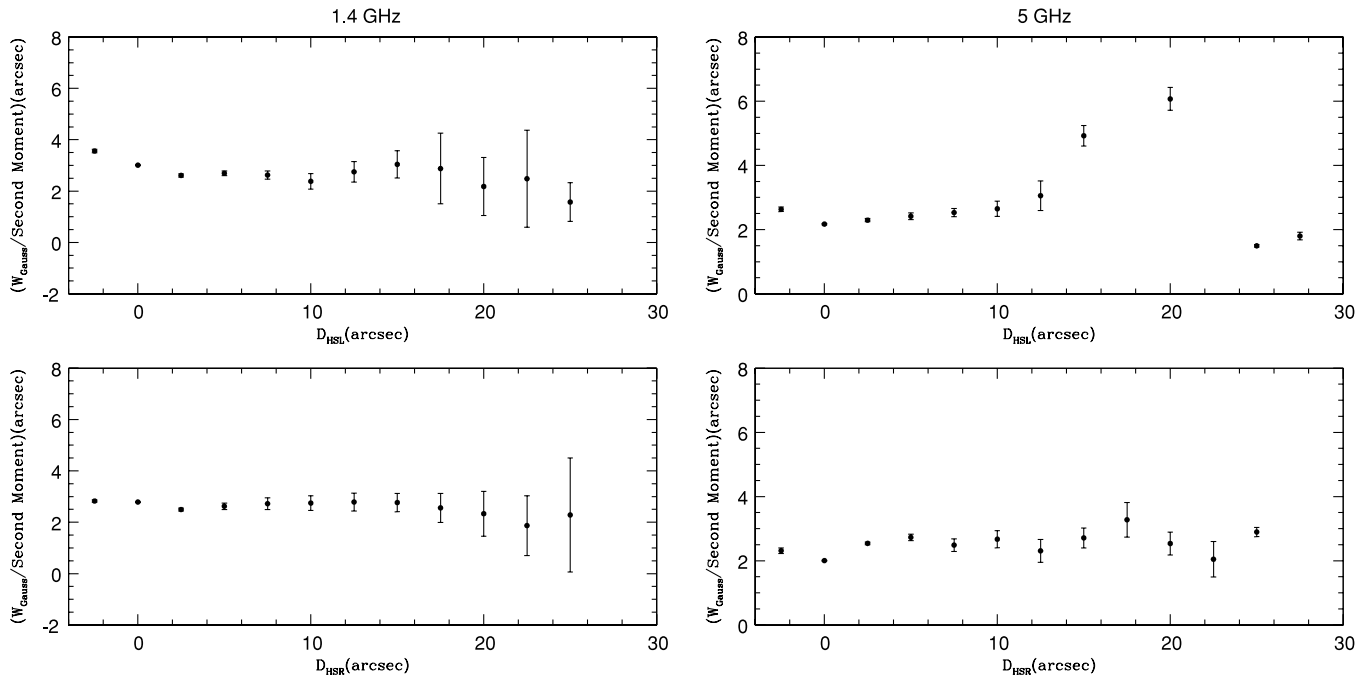


**Figure 69.** 3C114 ratio of the Gaussian FWHM to the second moment as a function of distance from the hot spot at 1.4 and 5 GHz (left and right panels, respectively) for the left- and right-hand sides of the source (top and bottom panels, respectively). The value of this ratio is fairly constant for each side of the source, and has a value of about 2.5–3. Similar results are obtained at 1.4 and 5 GHz.

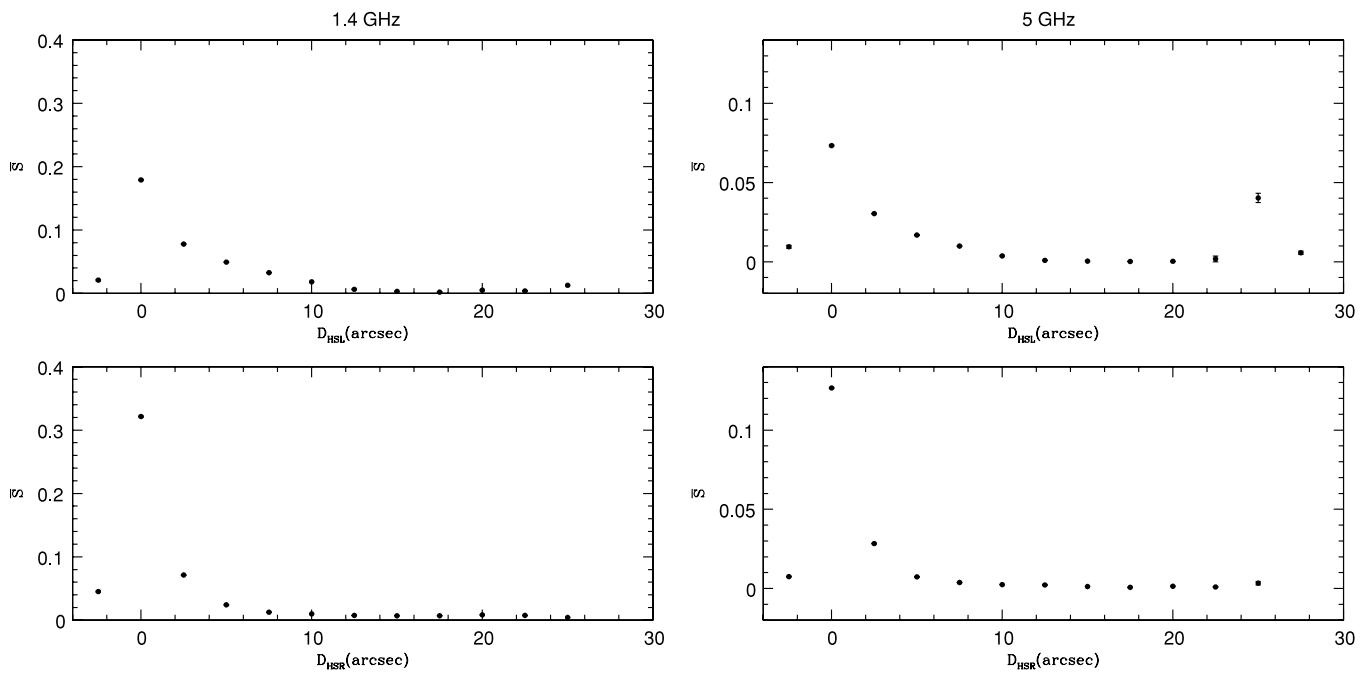


**Figure 70.** 3C114 average surface brightness in units of  $\text{Jy beam}^{-1}$  as a function of distance from the hot spot at 1.4 and 5 GHz (left and right panels, respectively) for the left- and right-hand sides of the source (top and bottom panels, respectively).

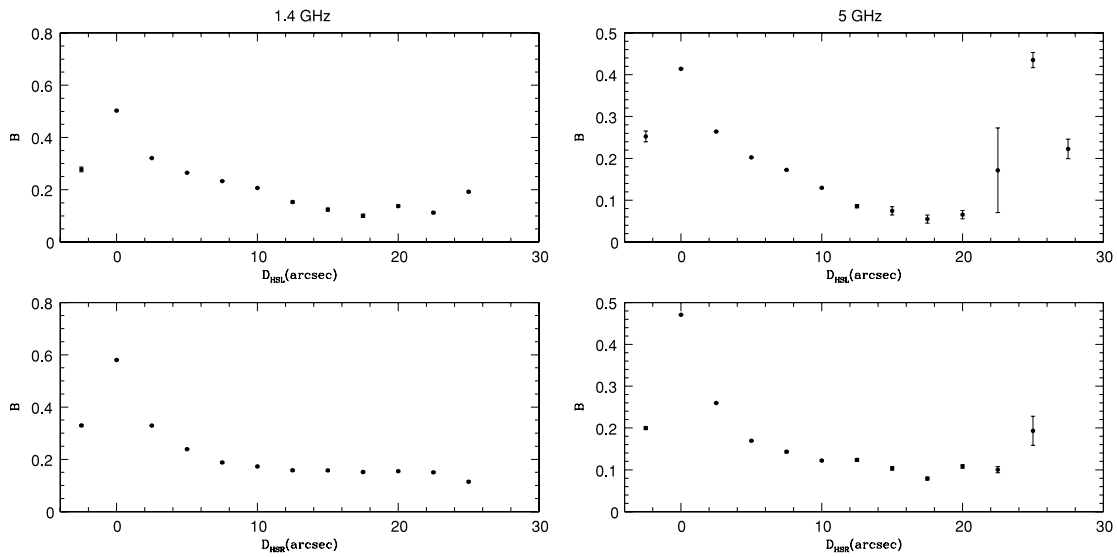


**Figure 71.** 3C114 minimum-energy magnetic field strength as a function of distance from the hot spot at 1.4 and 5 GHz (left and right panels, respectively) for the left- and right-hand sides of the source (top and bottom panels, respectively). The normalization is given in Table 1.

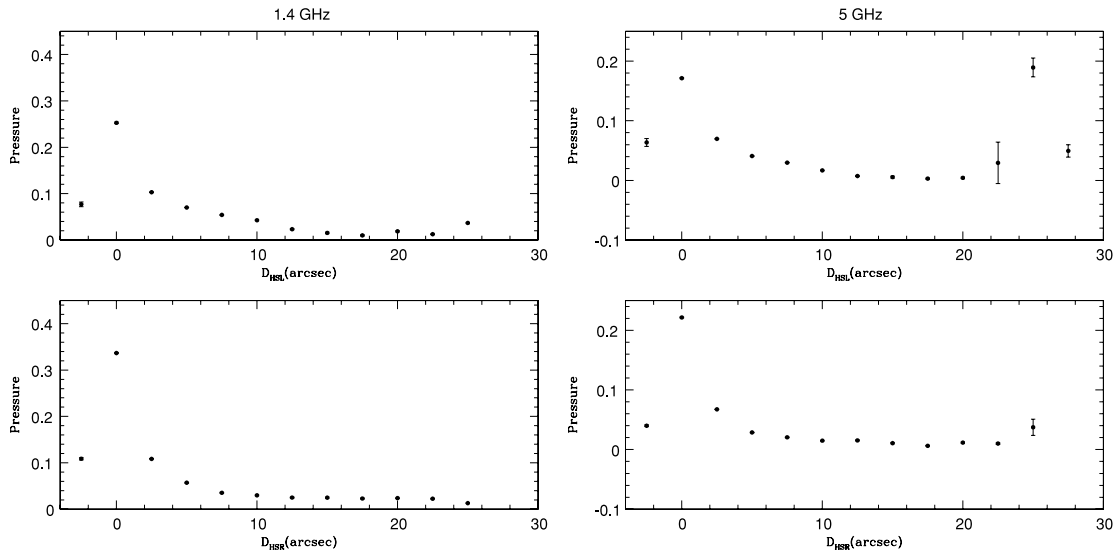


**Figure 72.** 3C114 minimum-energy pressure as a function of distance from the hot spot at 1.4 and 5 GHz (left and right panels, respectively) for the left- and right-hand sides of the source (top and bottom panels, respectively), as in Figure 12. The normalization is given in Table 1.

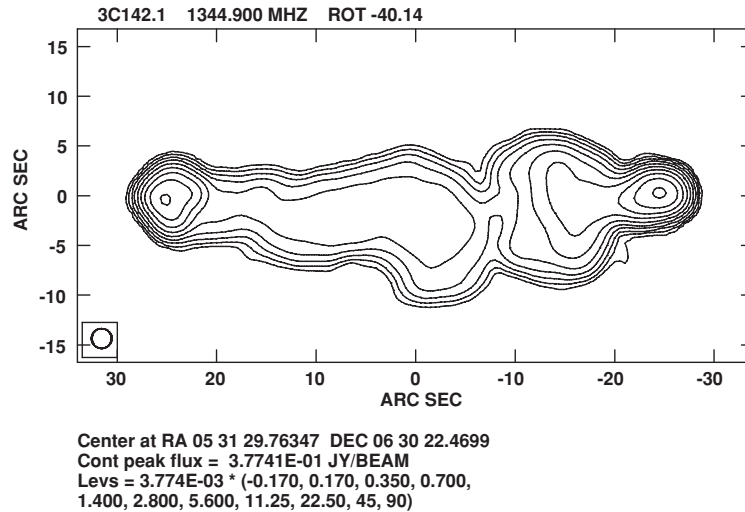


**Figure 73.** 3C142.1 at 1.4 GHz and 2'' resolution rotated by 40° 14 clockwise, as in Figure 1.

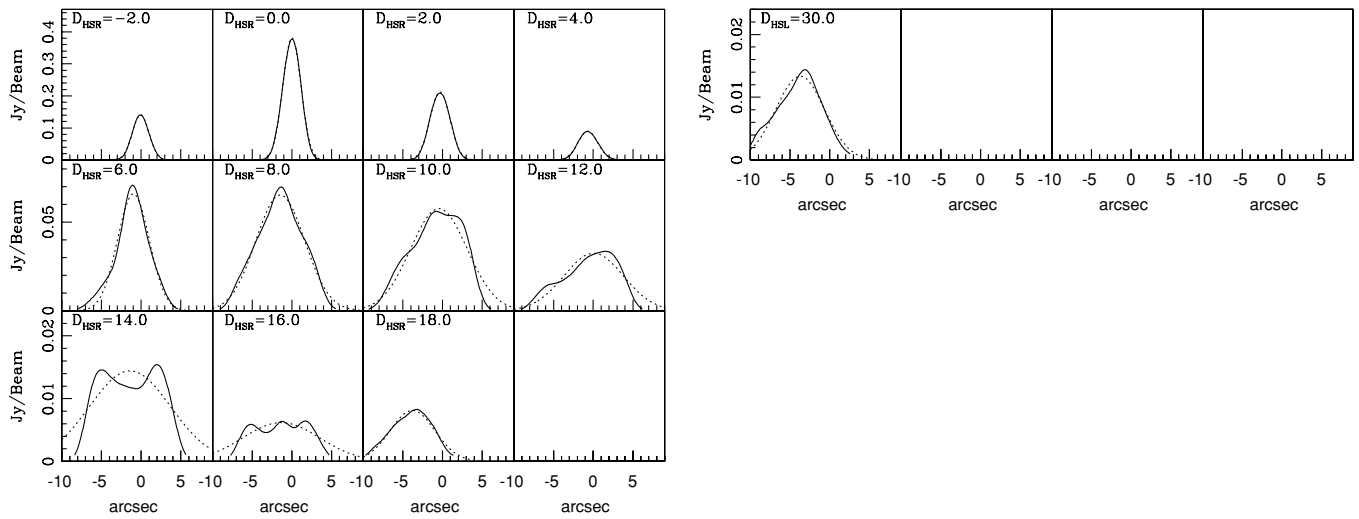


**Figure 74.** 3C142.1 surface brightness (solid line) and best-fit Gaussian (dotted line) for each cross-sectional slice of the radio bridge at 1.4 GHz, as in Figure 2. A Gaussian provides an excellent description of the surface brightness profile of each cross-sectional slice.

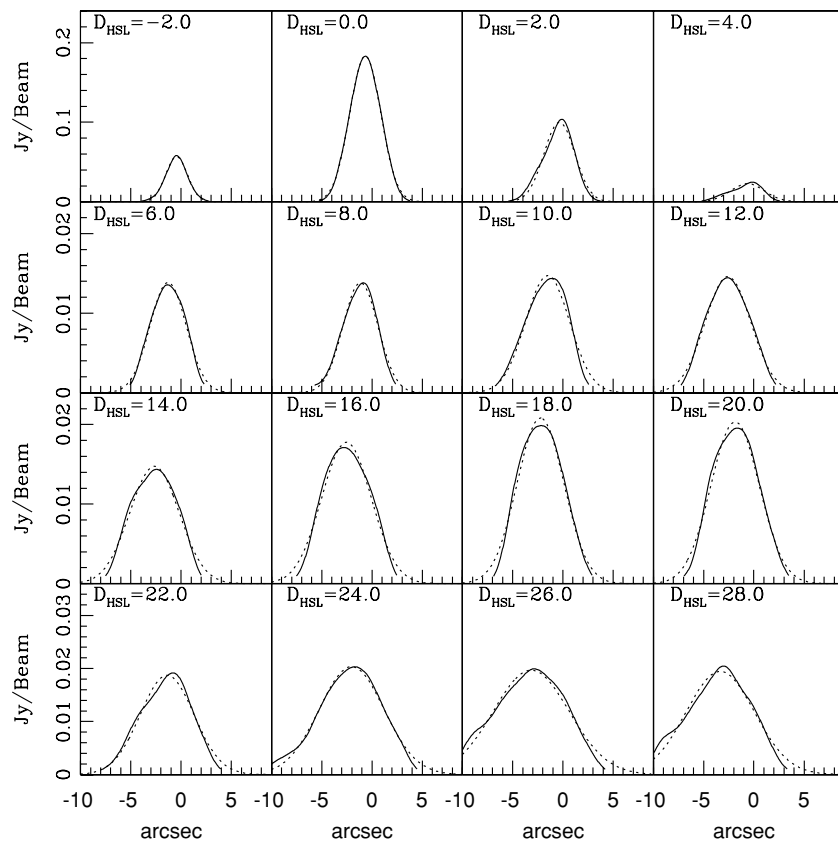


**Figure 75.** 3C142.1 surface brightness (solid line) and best-fit Gaussian (dotted line) for each cross-sectional slice of the radio bridge at 1.4 GHz, as in Figure 74. A Gaussian provides an excellent description of the surface brightness profile of each cross-sectional slice.

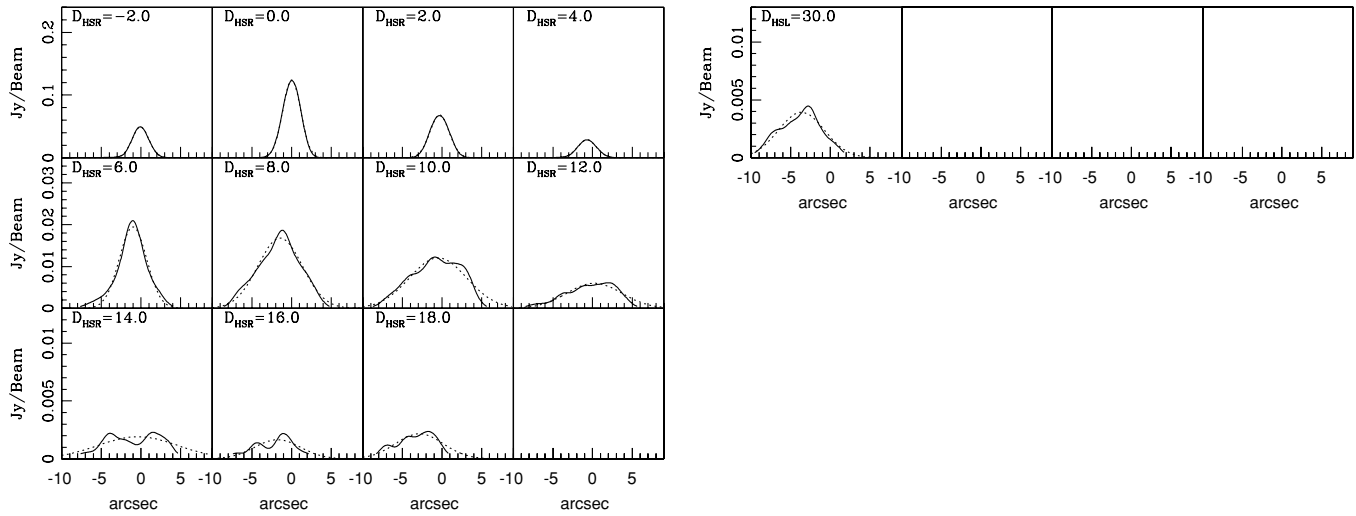


**Figure 76.** 3C142.1 surface brightness (solid line) and best-fit Gaussian (dotted line) for each cross-sectional slice of the radio bridge at 5 GHz, as in Figure 74 but at 5 GHz. Results obtained at 5 GHz are nearly identical to those obtained at 1.4 GHz.

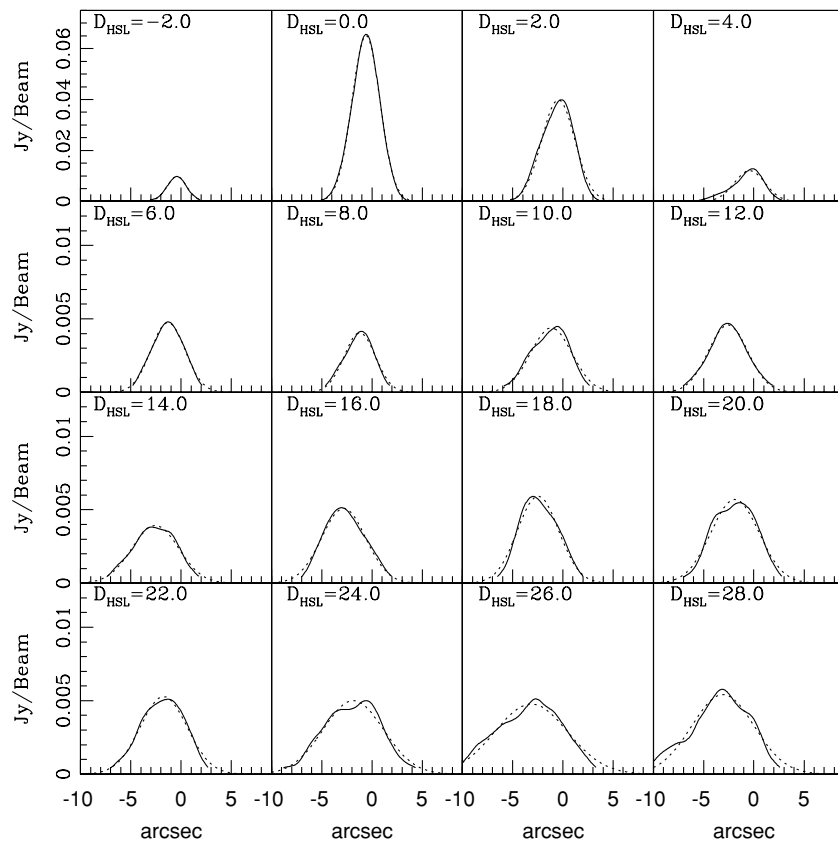


**Figure 77.** 3C142.1 surface brightness (solid line) and best-fit Gaussian (dotted line) for each cross-sectional slice of the radio bridge at 5 GHz, as in Figure 76. Results obtained at 5 GHz are nearly identical to those obtained at 1.4 GHz.

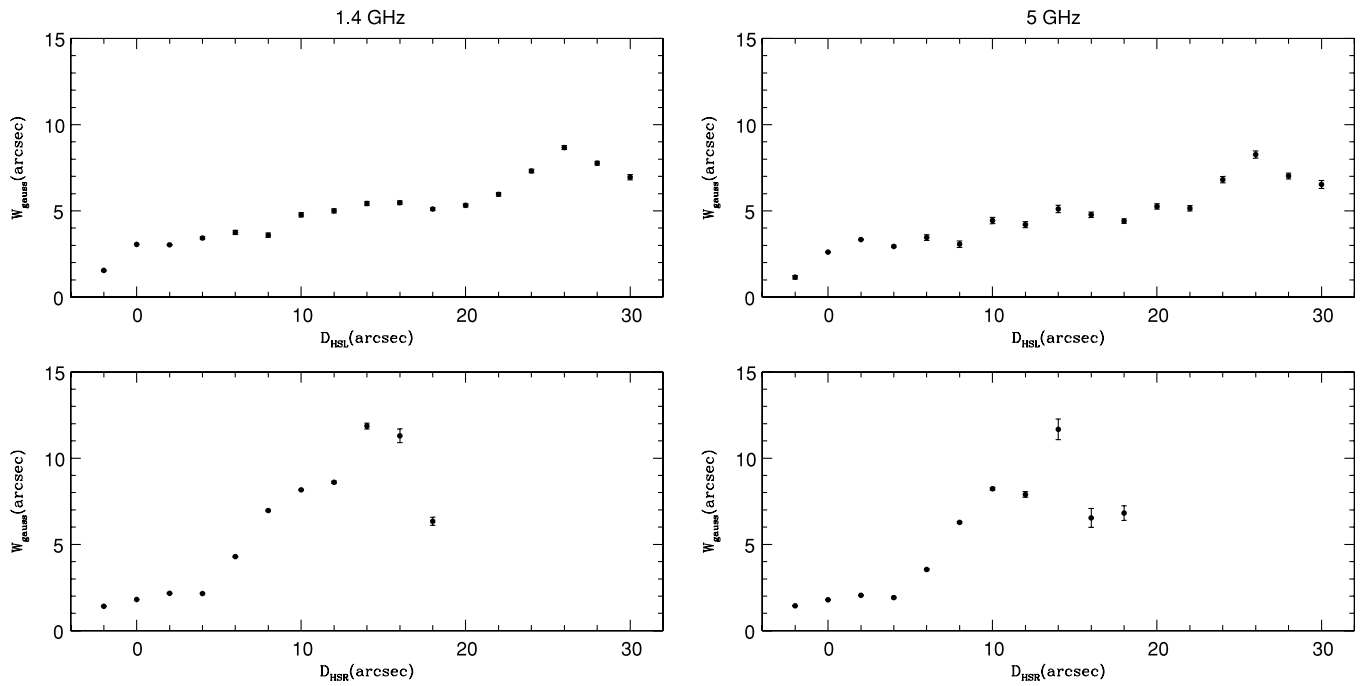


**Figure 78.** 3C142.1 Gaussian FWHM as a function of distance from the hot spot at 1.4 and 5 GHz (left and right panels, respectively) for the left- and right-hand sides of the source (top and bottom panels, respectively), as in Figure 4. The right- and left-hand sides of the source are somewhat symmetric. Similar results are obtained at 1.4 and 5 GHz.

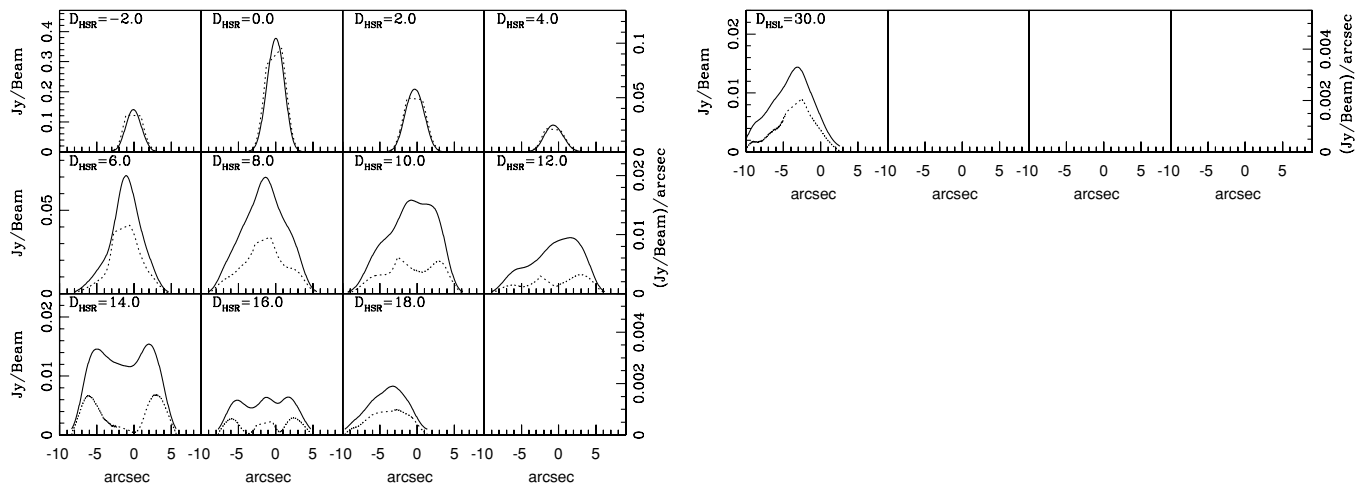


**Figure 79.** 3C142.1 emissivity (dotted line) and surface brightness (solid line) for each cross-sectional slice of the radio bridge at 1.4 GHz, as in Figure 5. A constant volume emissivity per slice provides a reasonable description of the data over most of the source.

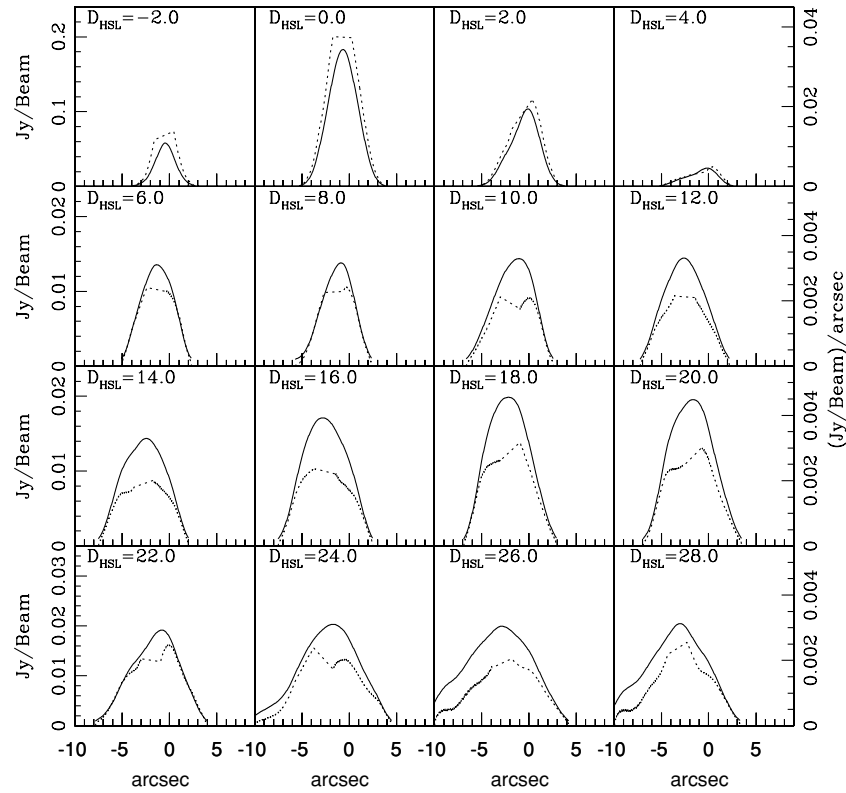


**Figure 80.** 3C142.1 emissivity (dotted line) and surface brightness (solid line) for each cross-sectional slice of the radio bridge at 1.4 GHz, as in Figure 79. A constant volume emissivity per slice provides a reasonable description of the data over most of the source.

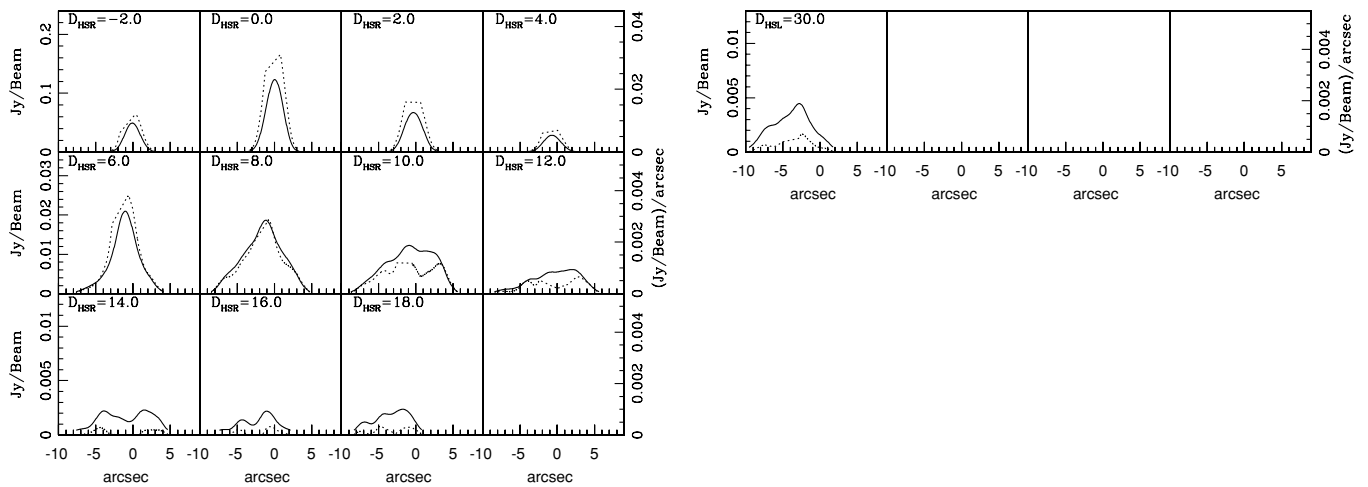


**Figure 81.** 3C142.1 emissivity (dotted line) and surface brightness (solid line) for each cross-sectional slice of the radio bridge at 5 GHz, as in Figure 79 but at 5 GHz. Results obtained at 5 GHz are nearly identical to those obtained at 1.4 GHz.

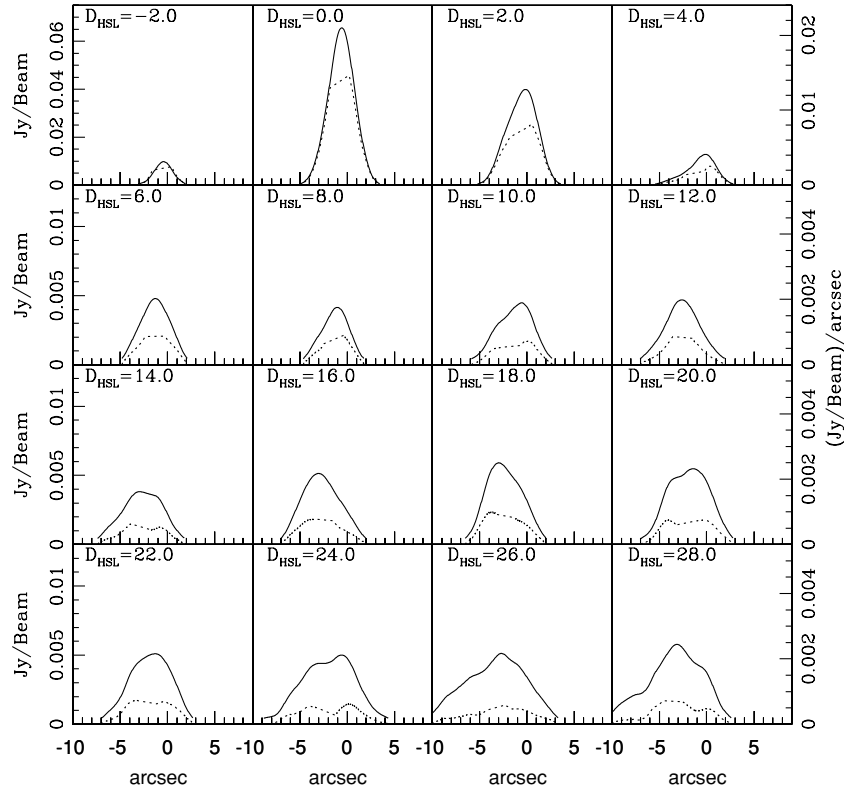


**Figure 82.** 3C142.1 emissivity (dotted line) and surface brightness (solid line) for each cross-sectional slice of the radio bridge at 5 GHz, as in Figure 79 but at 5 GHz. Results obtained at 5 GHz are nearly identical to those obtained at 1.4 GHz.

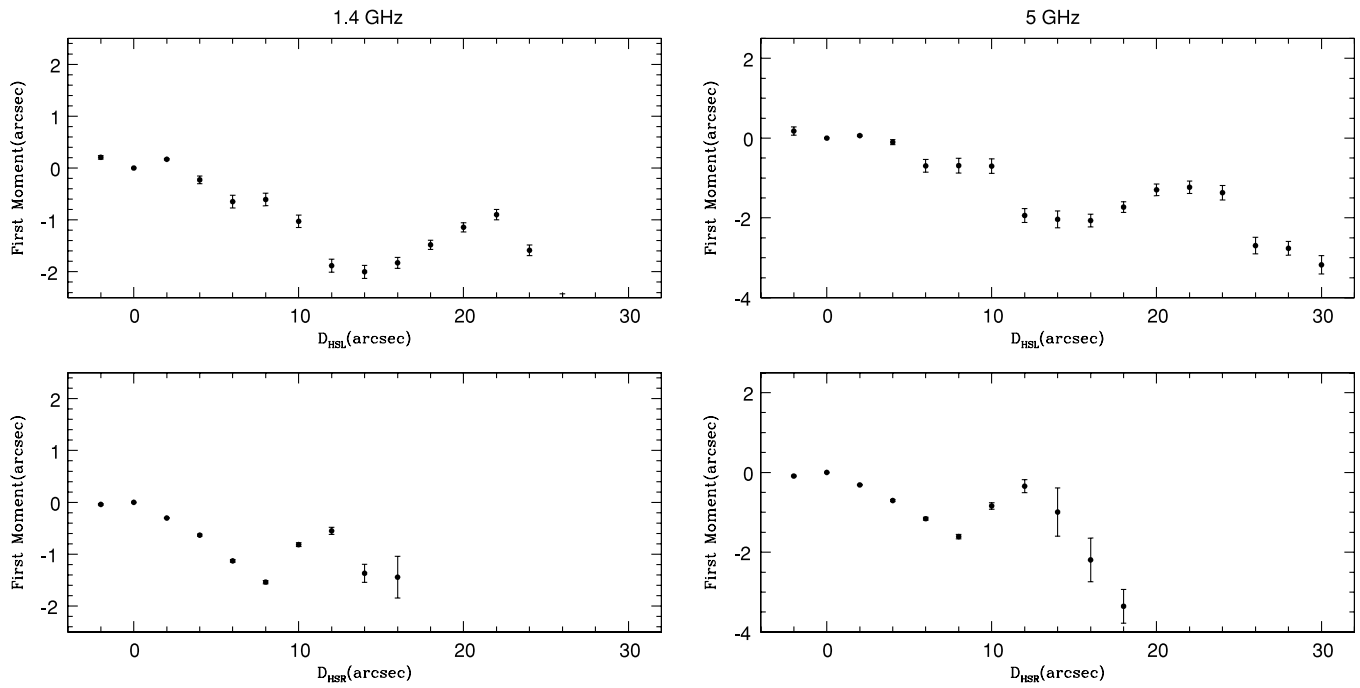


**Figure 83.** 3C142.1 first moment as a function of distance from the hot spot at 1.4 GHz and 5 GHz (left and right panels, respectively) for the left- and right-hand sides of the source (top and bottom, respectively).

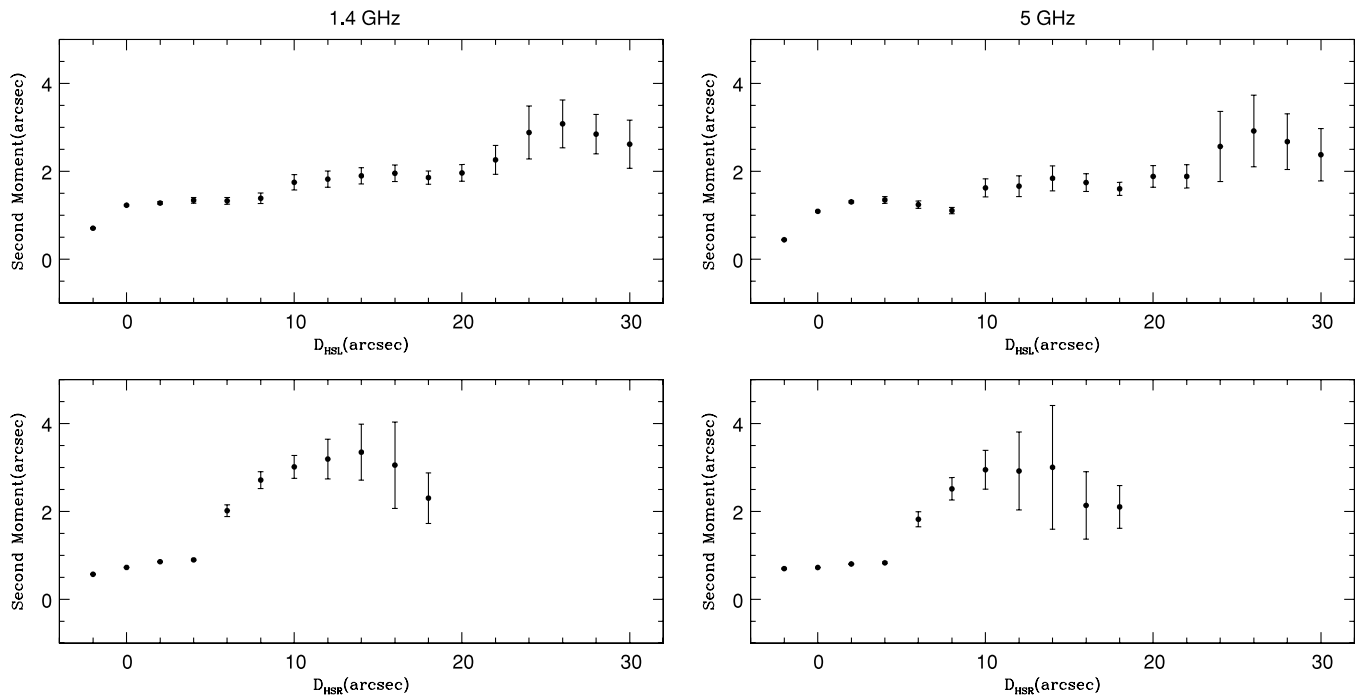


**Figure 84.** 3C142.1 second moment as a function of distance from the hot spot at 1.4 GHz and 5 GHz (left and right panels, respectively) for the left and right sides of the source (top and bottom panels, respectively).

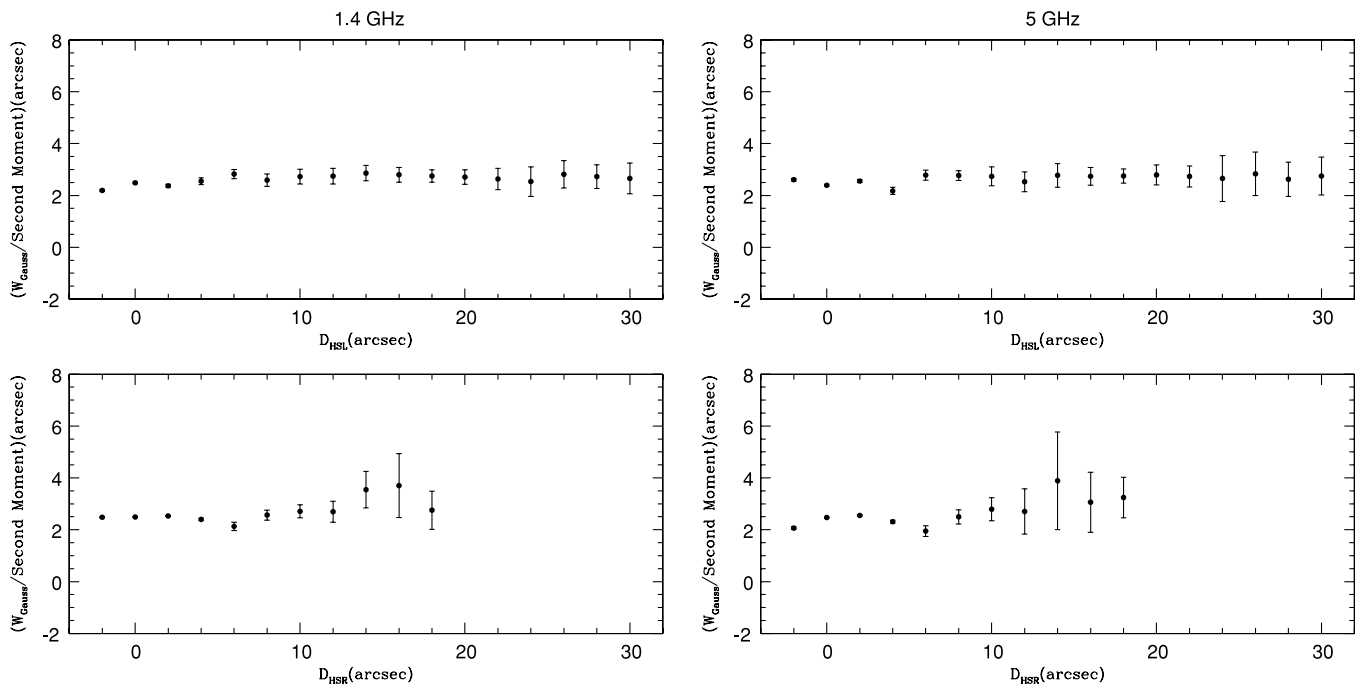


**Figure 85.** 3C142.1 ratio of the Gaussian FWHM to the second moment as a function of distance from the hot spot at 1.4 and 5 GHz (left and right panels, respectively) for the left- and right-hand sides of the source (top and bottom panels, respectively). The value of this ratio is fairly constant for each side of the source, and has a value of about 2. Similar results are obtained at 1.4 and 5 GHz.

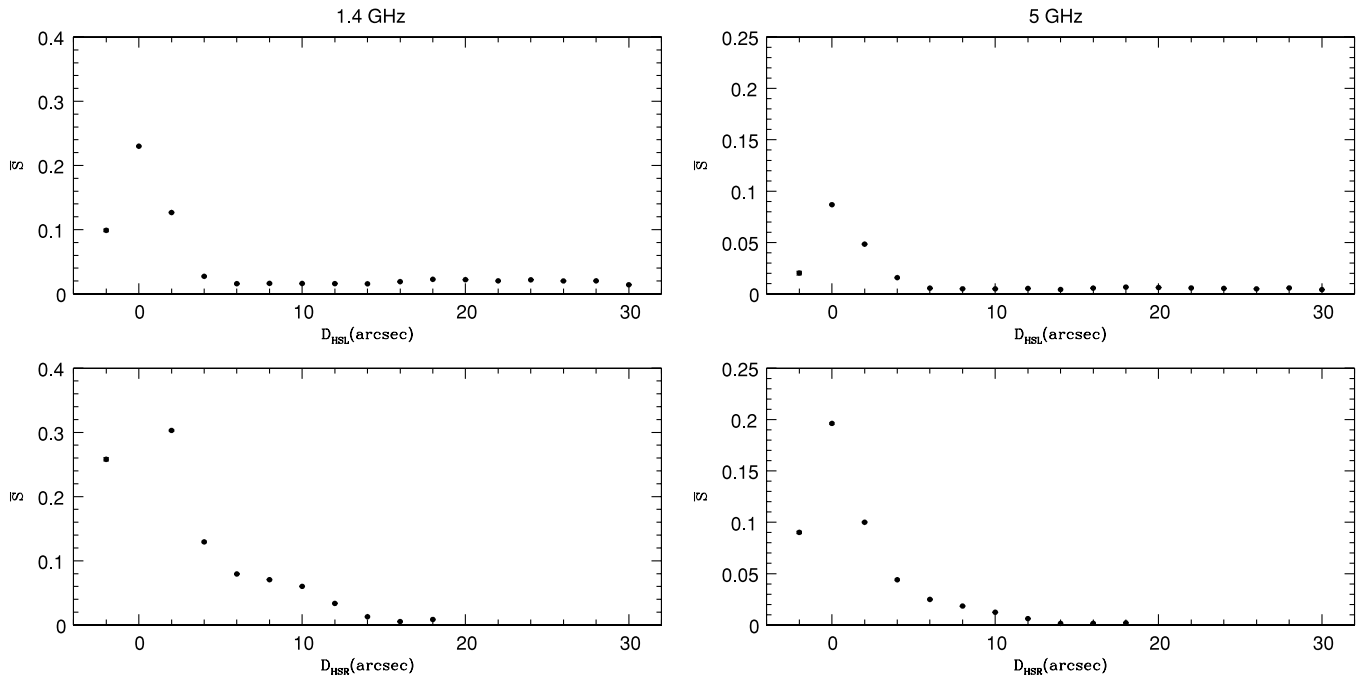


**Figure 86.** 3C142.1 average surface brightness in units of  $\text{Jy beam}^{-1}$  as a function of distance from the hot spot at 1.4 and 5 GHz (left and right panels, respectively) for the left- and right-hand sides of the source (top and bottom panels, respectively).

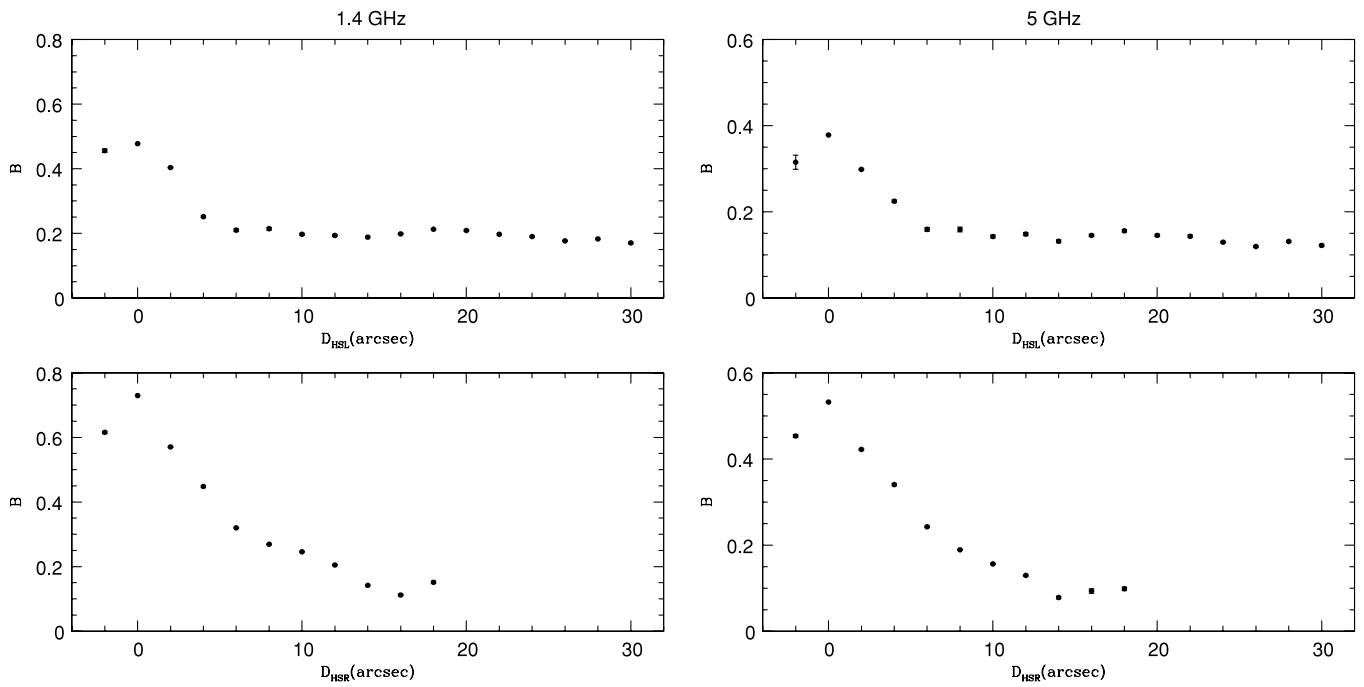


**Figure 87.** 3C142.1 minimum-energy magnetic field strength as a function of distance from the hot spot at 1.4 and 5 GHz (left and right panels, respectively) for the left- and right-hand sides of the source (top and bottom panels, respectively). The normalization is given in Table 1.

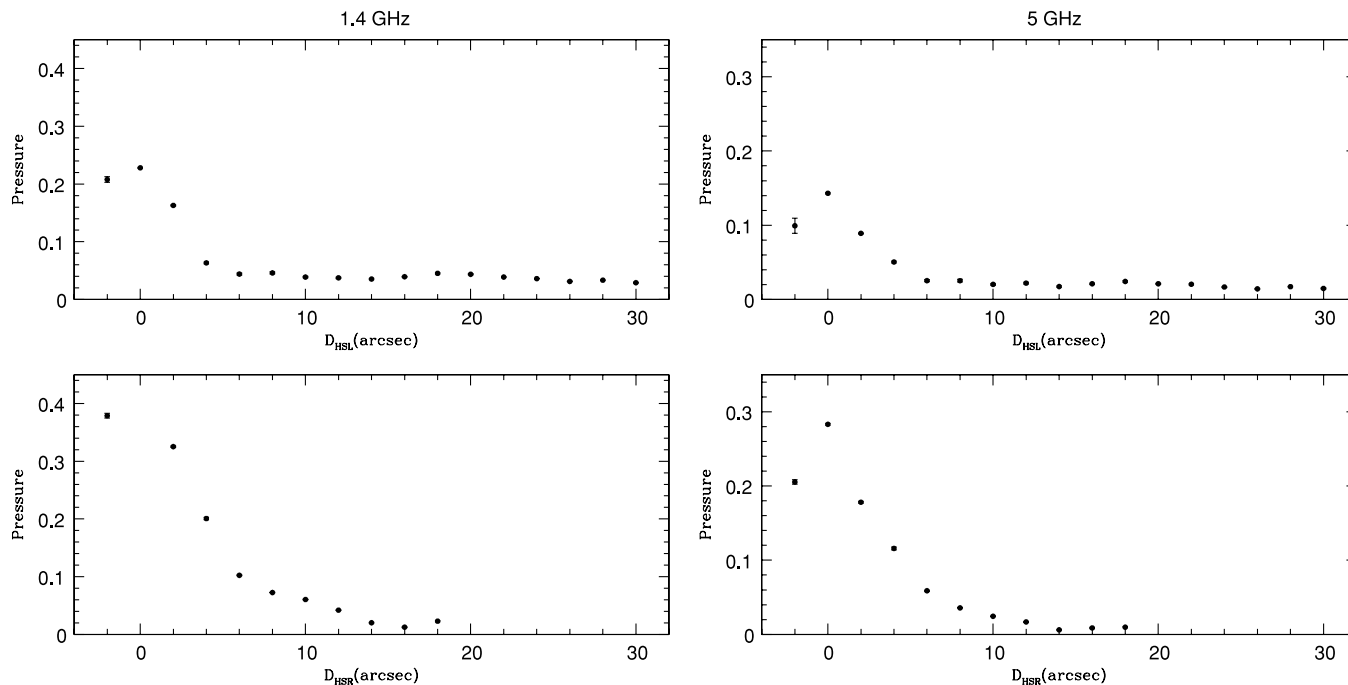


**Figure 88.** 3C142.1 minimum-energy pressure as a function of distance from the hot spot at 1.4 and 5 GHz (left and right panels, respectively) for the left- and right-hand sides of the source (top and bottom panels, respectively), as in Figure 12. The normalization is given in Table 1.

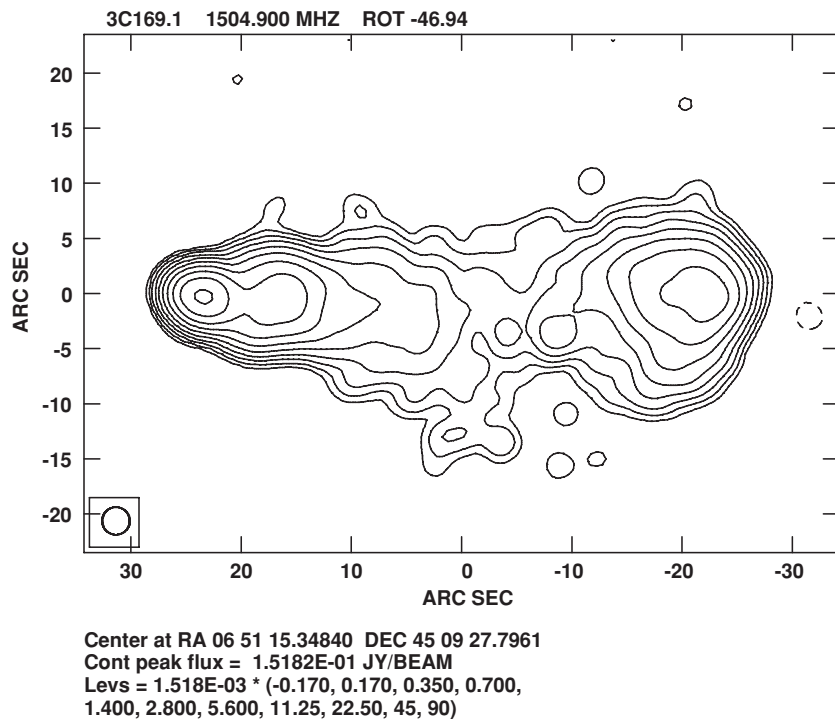


**Figure 89.** 3C169.1 at 1.4 GHz and 2.5 resolution rotated by 46.94 clockwise, as in Figure 1.

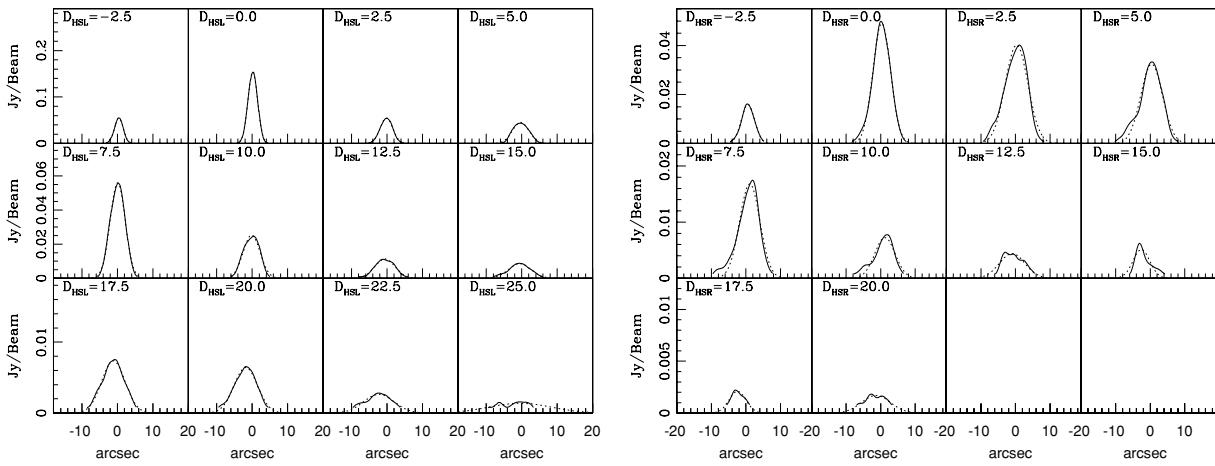


**Figure 90.** 3C169.1 surface brightness (solid line) and best-fit Gaussian (dotted line) for each cross-sectional slice of the radio bridge at 1.4 GHz, as in Figure 2. A Gaussian provides an excellent description of the surface brightness profile of each cross-sectional slice.

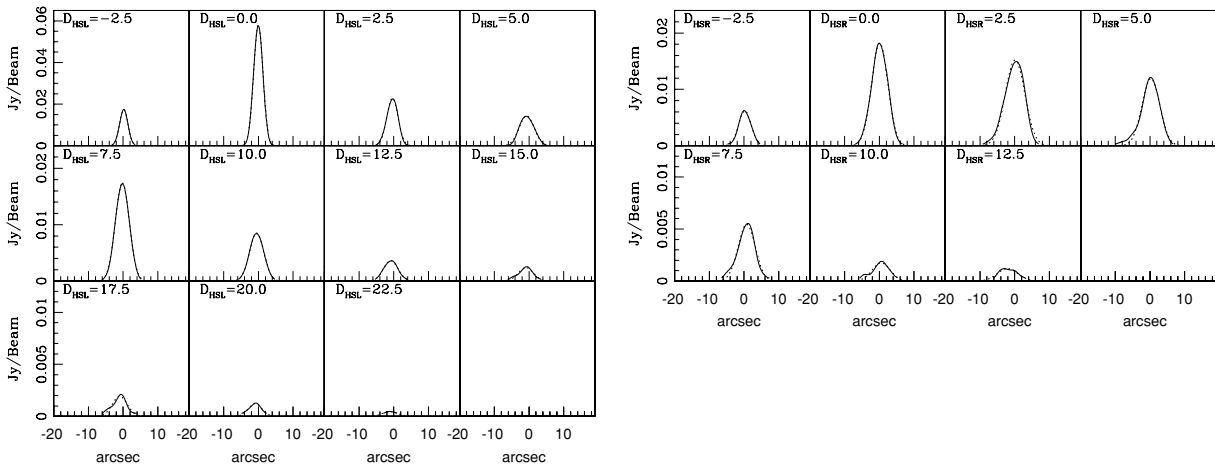


**Figure 91.** 3C169.1 surface brightness (solid line) and best-fit Gaussian (dotted line) for each cross-sectional slice of the radio bridge at 5 GHz, as in Figure 90 but at 5 GHz. Results obtained at 5 GHz are nearly identical to those obtained at 1.4 GHz.

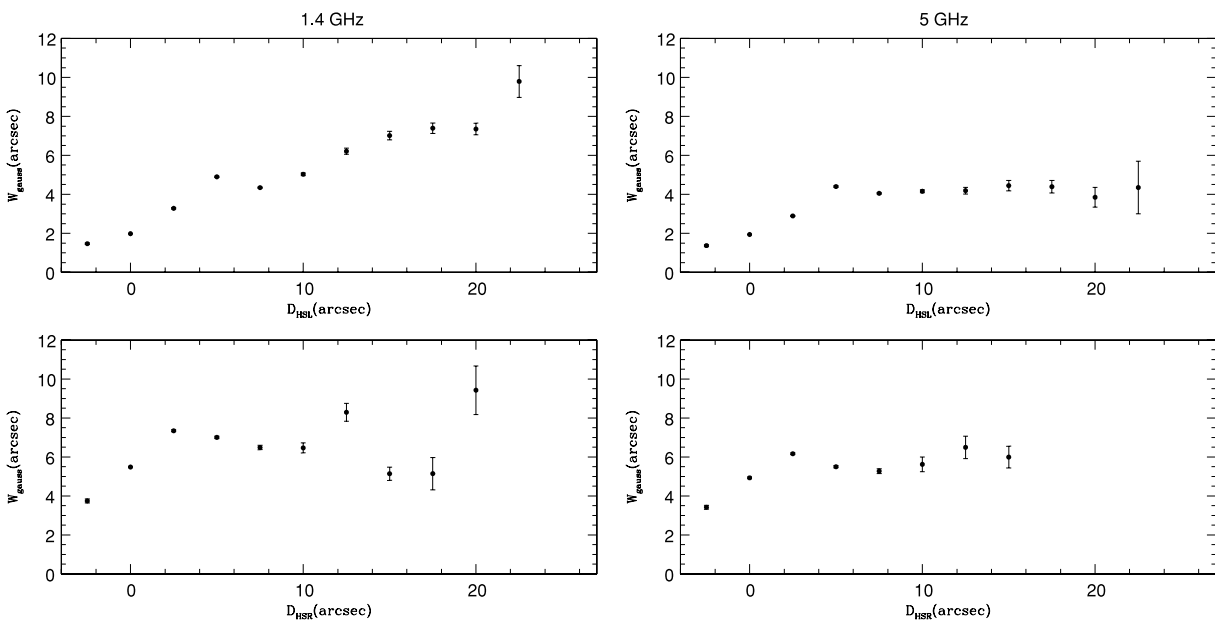


**Figure 92.** 3C169.1 Gaussian FWHM as a function of distance from the hot spot at 1.4 and 5 GHz (left and right panels, respectively) for the left- and right-hand sides of the source (top and bottom panels, respectively), as in Figure 4. The right- and left-hand sides of the source are fairly symmetric. Similar results are obtained at 1.4 and 5 GHz.

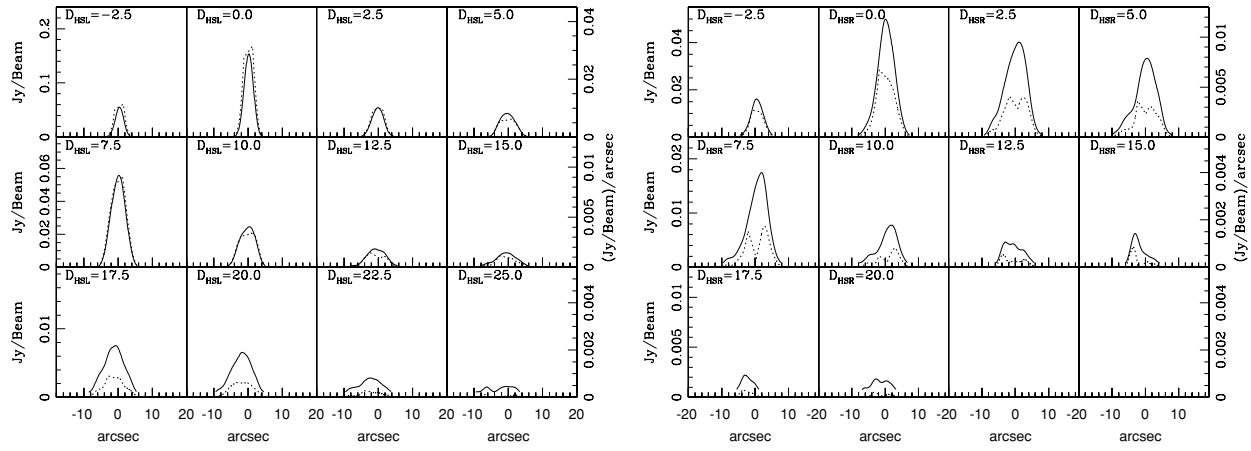


**Figure 93.** 3C169.1 emissivity (dotted line) and surface brightness (solid line) for each cross-sectional slice of the radio bridge at 1.4 GHz, as in Figure 5. A constant volume emissivity per slice provides a reasonable description of the data over most of the source.

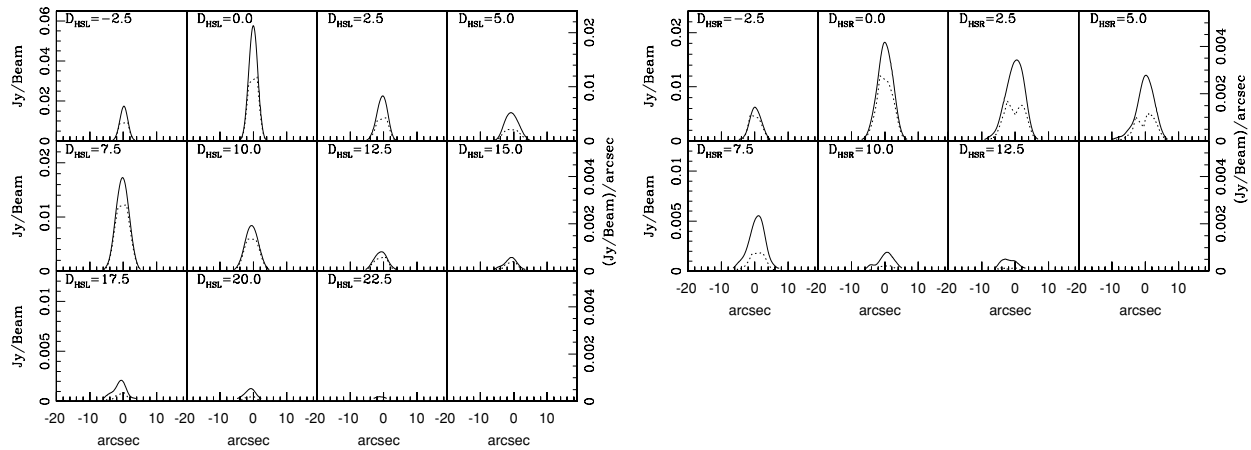


**Figure 94.** 3C169.1 emissivity (dotted line) and surface brightness (solid line) for each cross-sectional slice of the radio bridge at 5 GHz, as in Figure 93 but at 5 GHz. Results obtained at 5 GHz are nearly identical to those obtained at 1.4 GHz.

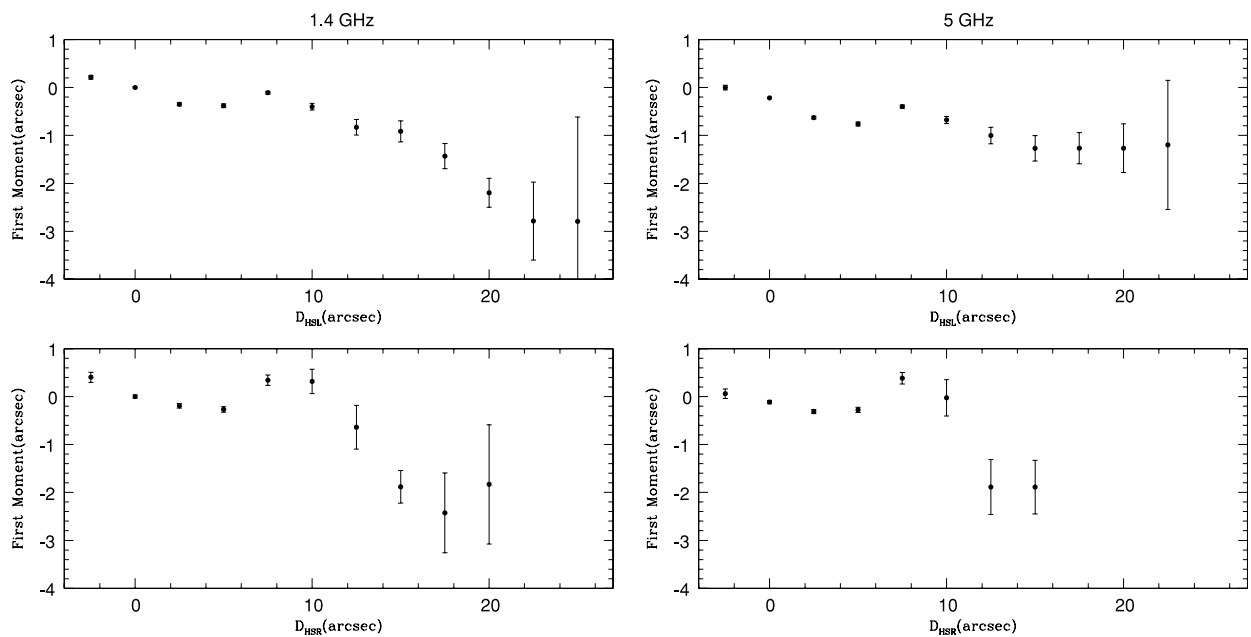


**Figure 95.** 3C169.1 first moment as a function of distance from the hot spot at 1.4 GHz and 5 GHz (left and right panels, respectively) for the left- and right-hand sides of the source (top and bottom, respectively).

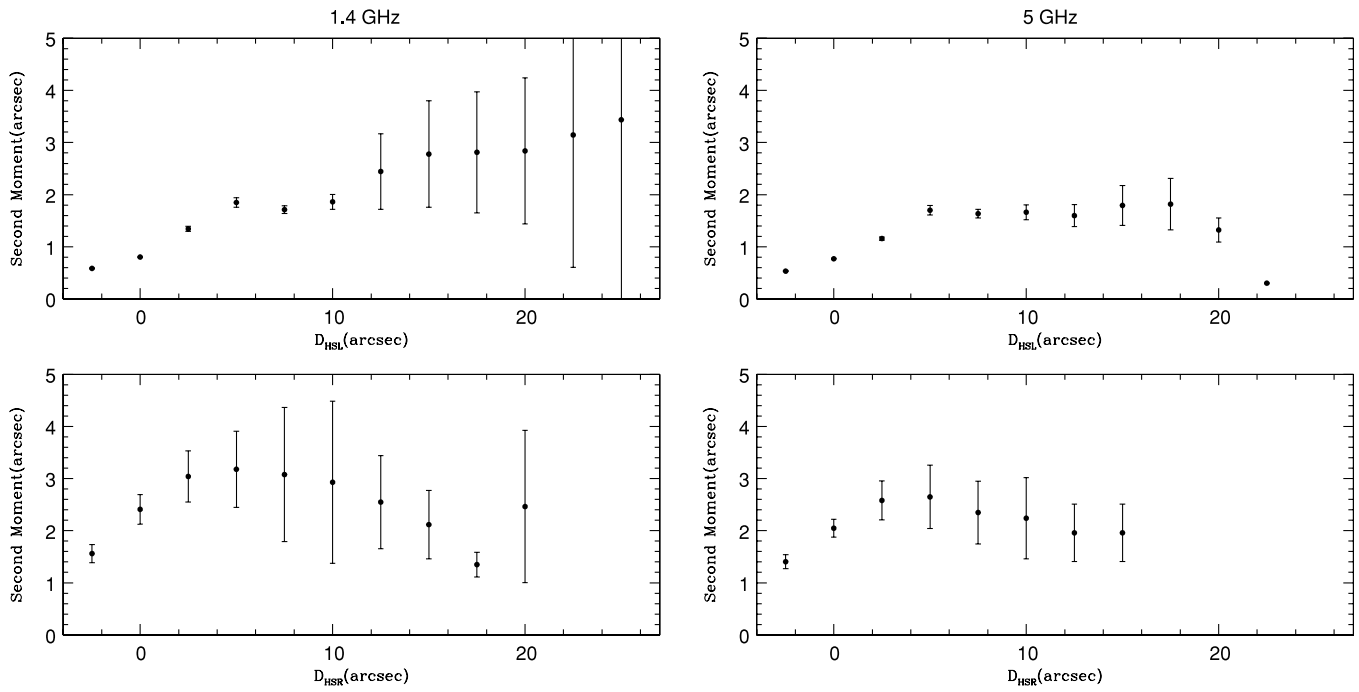


**Figure 96.** 3C169.1 second moment as a function of distance from the hot spot at 1.4 GHz and 5 GHz (left and right panels, respectively) for the left and right sides of the source (top and bottom panels, respectively).

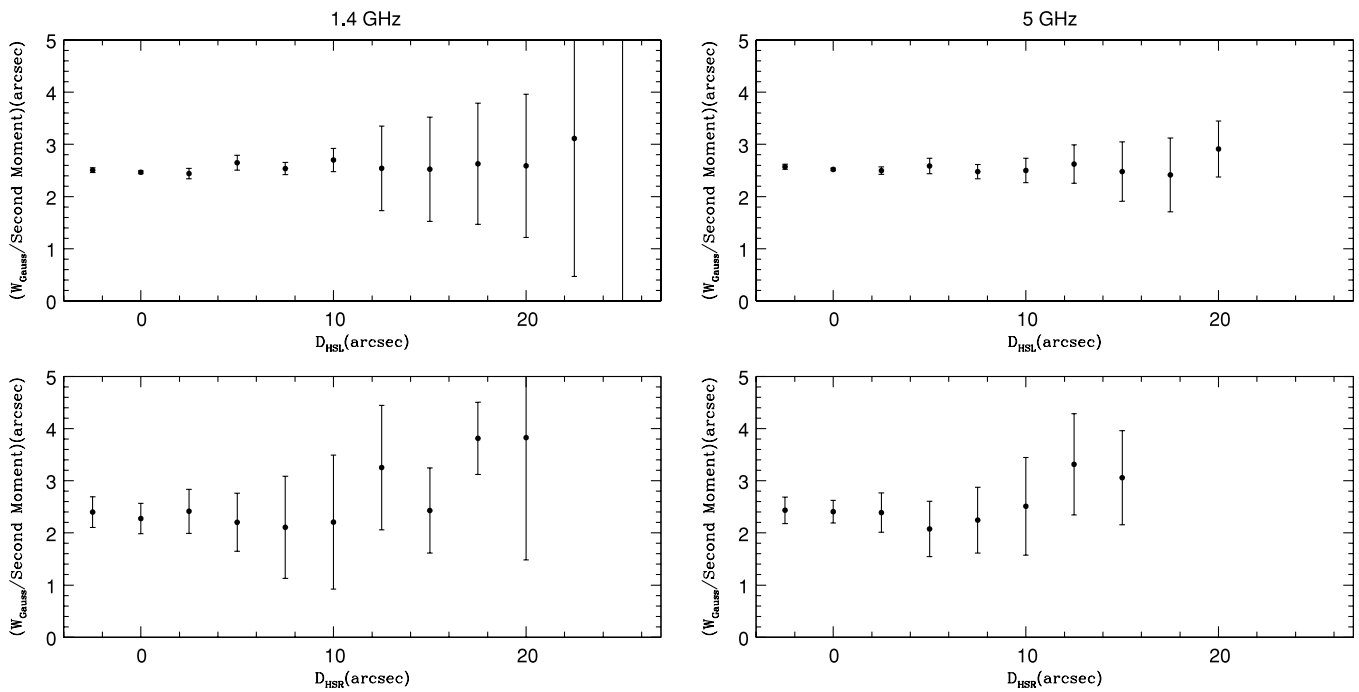


**Figure 97.** 3C169.1 ratio of the Gaussian FWHM to the second moment as a function of distance from the hot spot at 1.4 and 5 GHz (left and right panels, respectively) for the left- and right-hand sides of the source (top and bottom panels, respectively). The value of this ratio is fairly constant for each side of the source, and has a value of about 2.5. Similar results are obtained at 1.4 and 5 GHz.

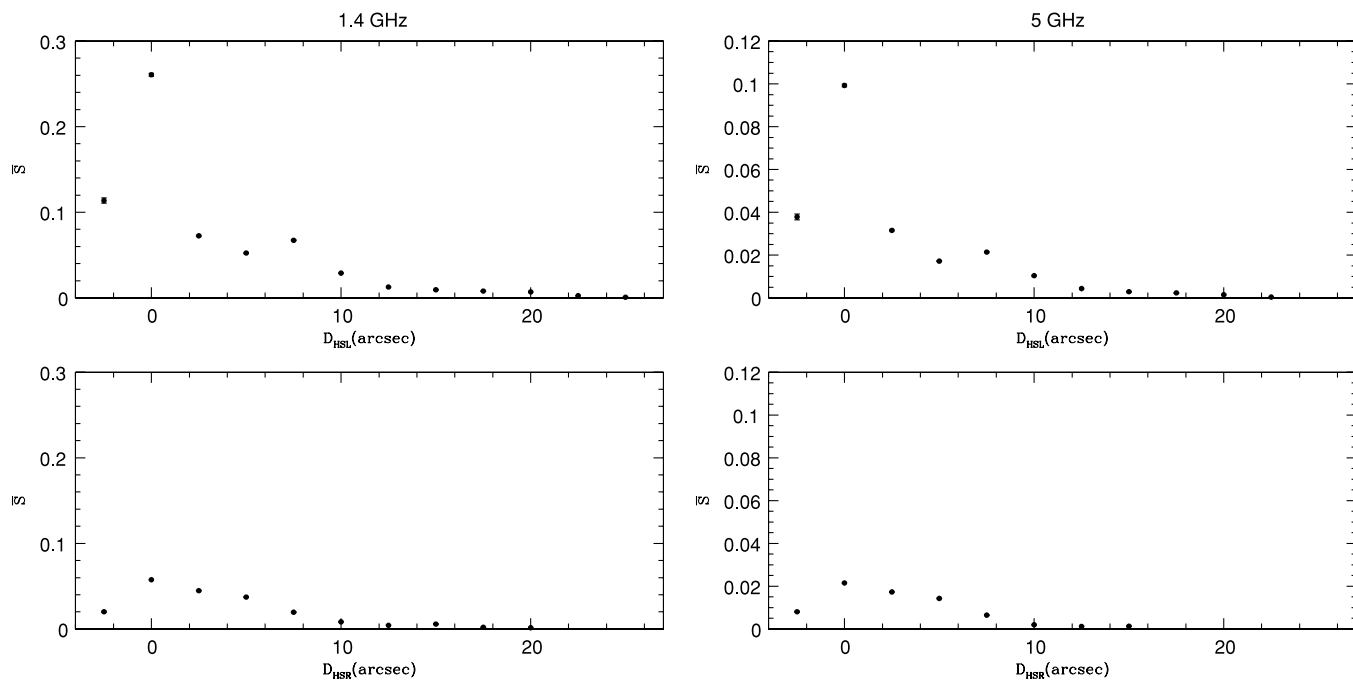


**Figure 98.** 3C169.1 average surface brightness in units of  $\text{Jy beam}^{-1}$  as a function of distance from the hot spot at 1.4 and 5 GHz (left and right panels, respectively) for the left- and right-hand sides of the source (top and bottom panels, respectively).

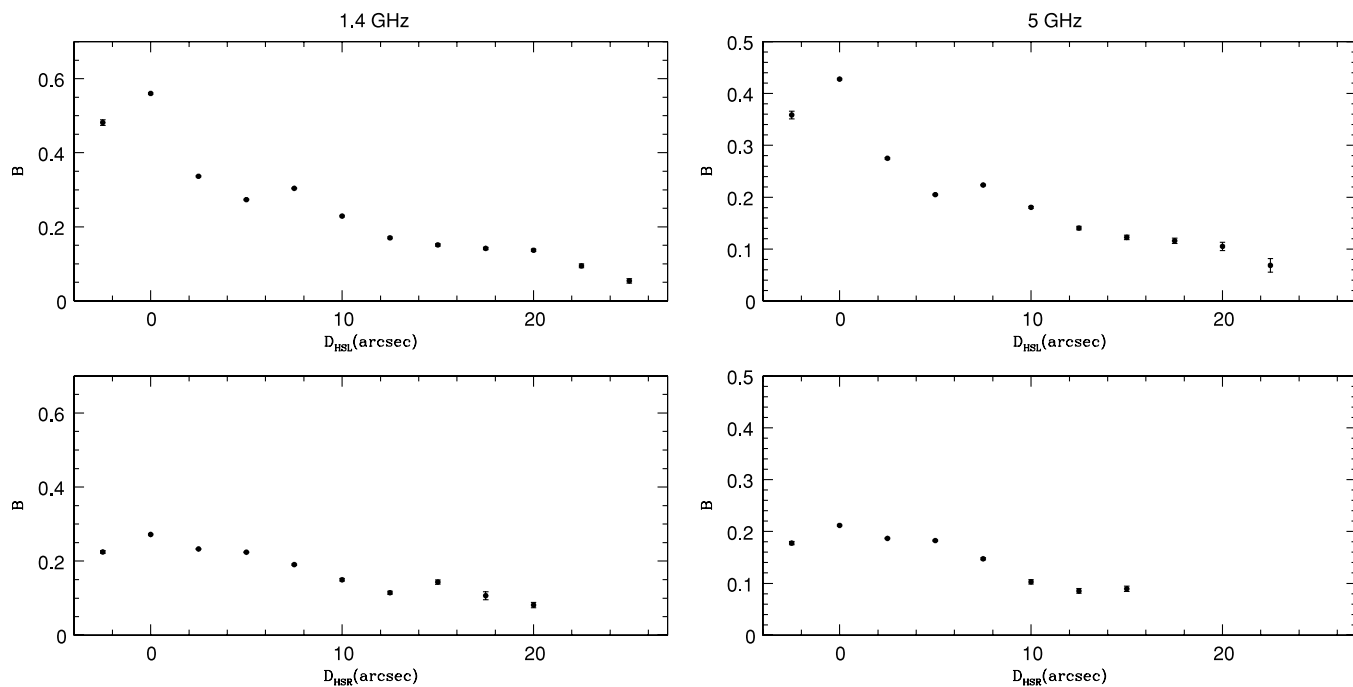


**Figure 99.** 3C169.1 minimum-energy magnetic field strength as a function of distance from the hot spot at 1.4 and 5 GHz (left and right panels, respectively) for the left- and right-hand sides of the source (top and bottom panels, respectively). The normalization is given in Table 1. The flat magnetic field strength across the right-hand side of the source is caused by the weak hot spot on that side.

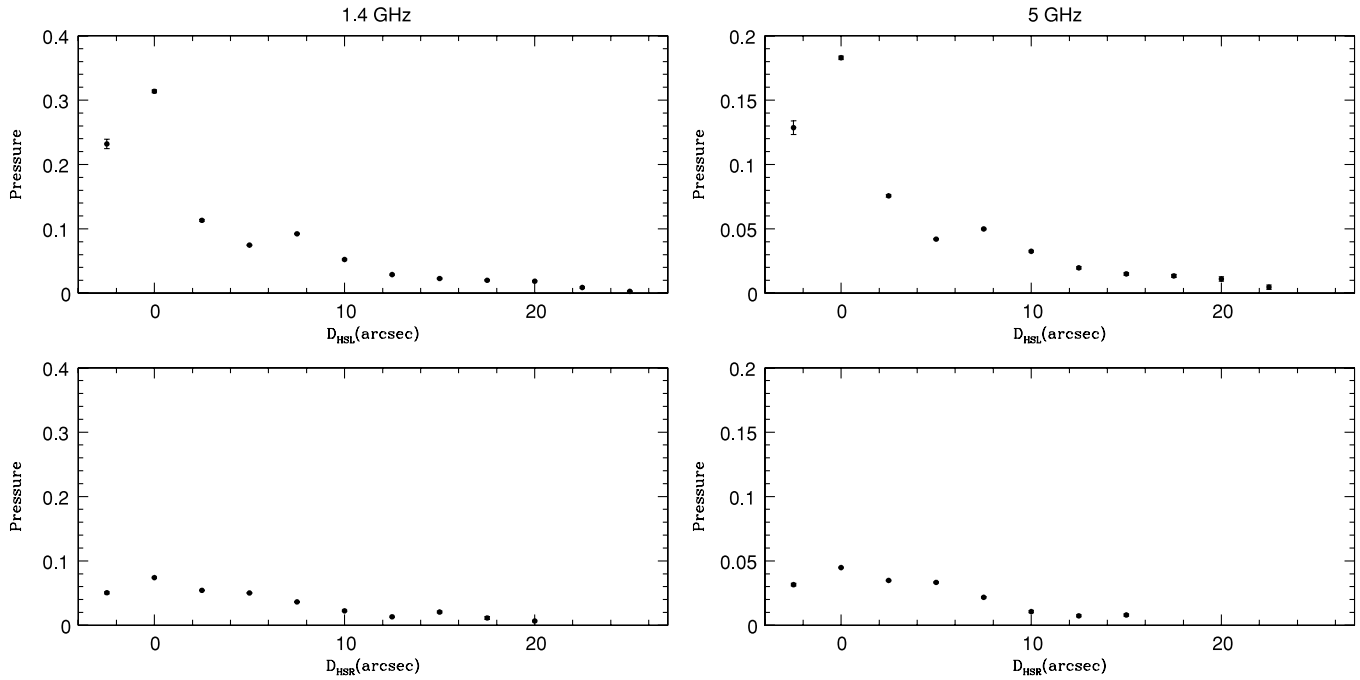


**Figure 100.** 3C169.1 minimum-energy pressure as a function of distance from the hot spot at 1.4 and 5 GHz (left and right panels, respectively) for the left- and right-hand sides of the source (top and bottom panels, respectively), as in Figure 12. The normalization is given in Table 1. The flat pressure profile across the right-hand side of the source is caused by the weak hot spot on that side of the source.

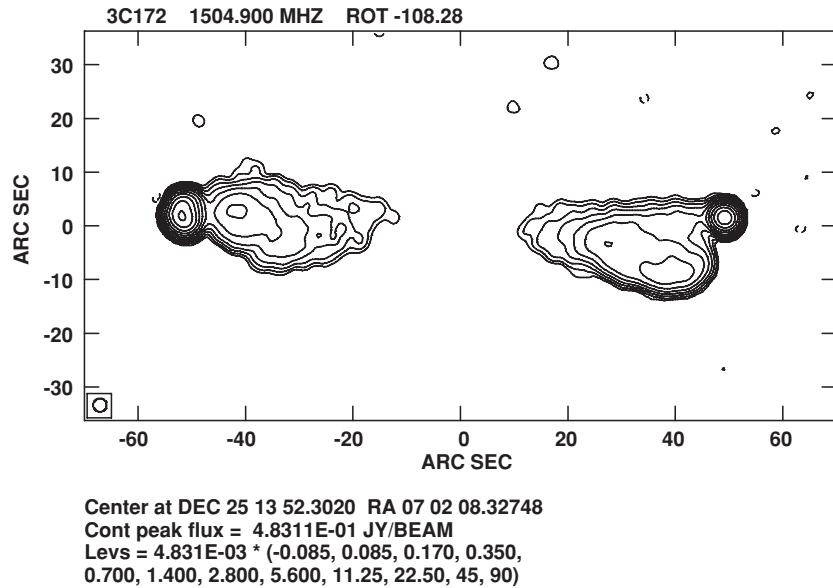


**Figure 101.** 3C172 at 1.4 GHz and 2'' resolution rotated by 108°28 clockwise, as in Figure 1.

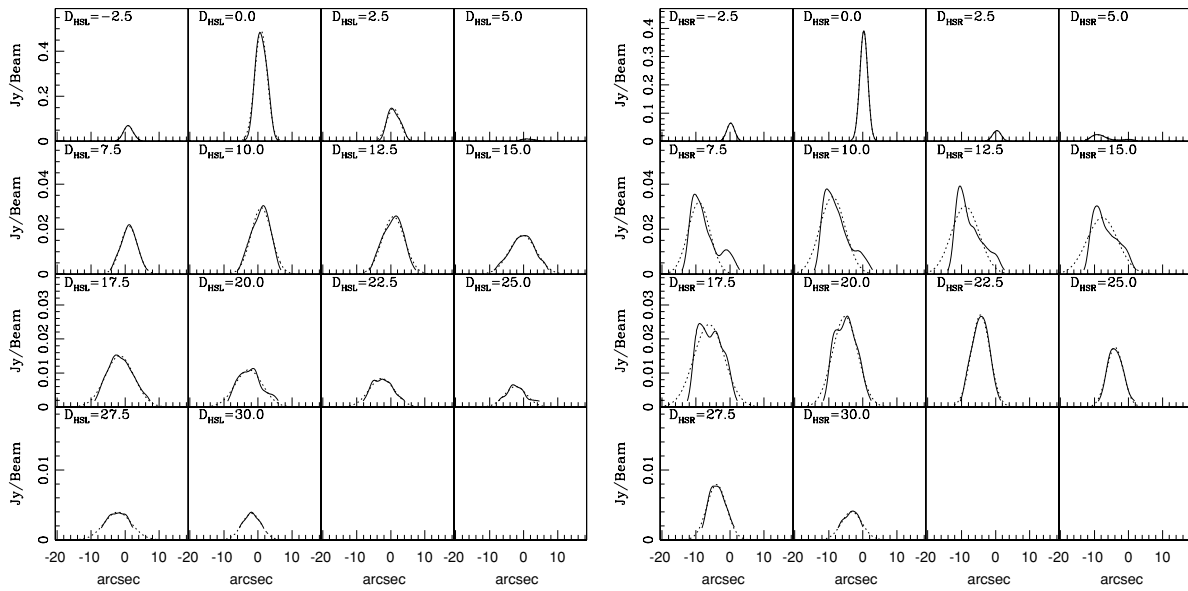


**Figure 102.** 3C172 surface brightness (solid line) and best-fit Gaussian (dotted line) for each cross-sectional slice of the radio bridge at 1.4 GHz, as in Figure 2. A Gaussian provides an excellent description of the surface brightness profile of each cross-sectional slice.

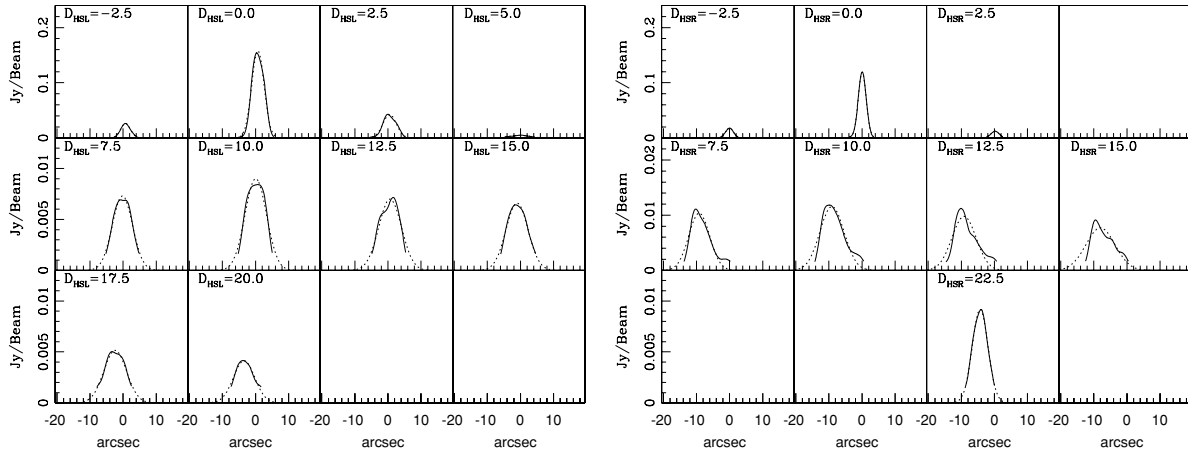


**Figure 103.** 3C172 surface brightness (solid line) and best-fit Gaussian (dotted line) for each cross-sectional slice of the radio bridge at 5 GHz, as in Figure 102 but at 5 GHz. Results obtained at 5 GHz are nearly identical to those obtained at 1.4 GHz.

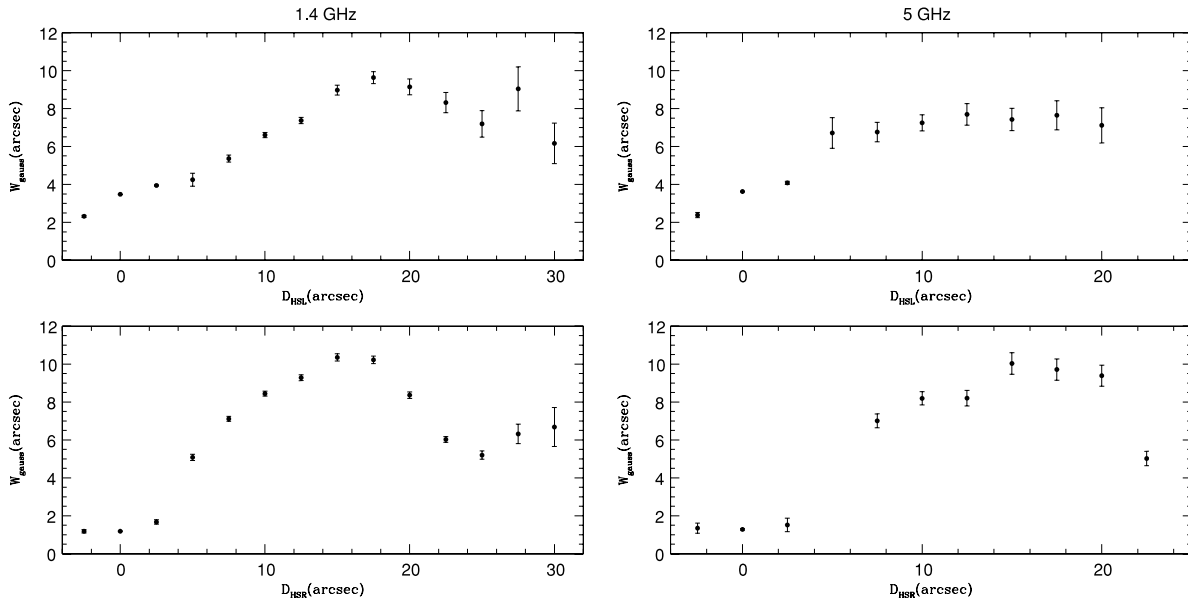


**Figure 104.** 3C172 Gaussian FWHM as a function of distance from the hot spot at 1.4 and 5 GHz (left and right panels, respectively) for the left- and right-hand sides of the source (top and bottom panels, respectively), as in Figure 4. The right- and left-hand sides of the source are fairly symmetric. Similar results are obtained at 1.4 and 5 GHz.

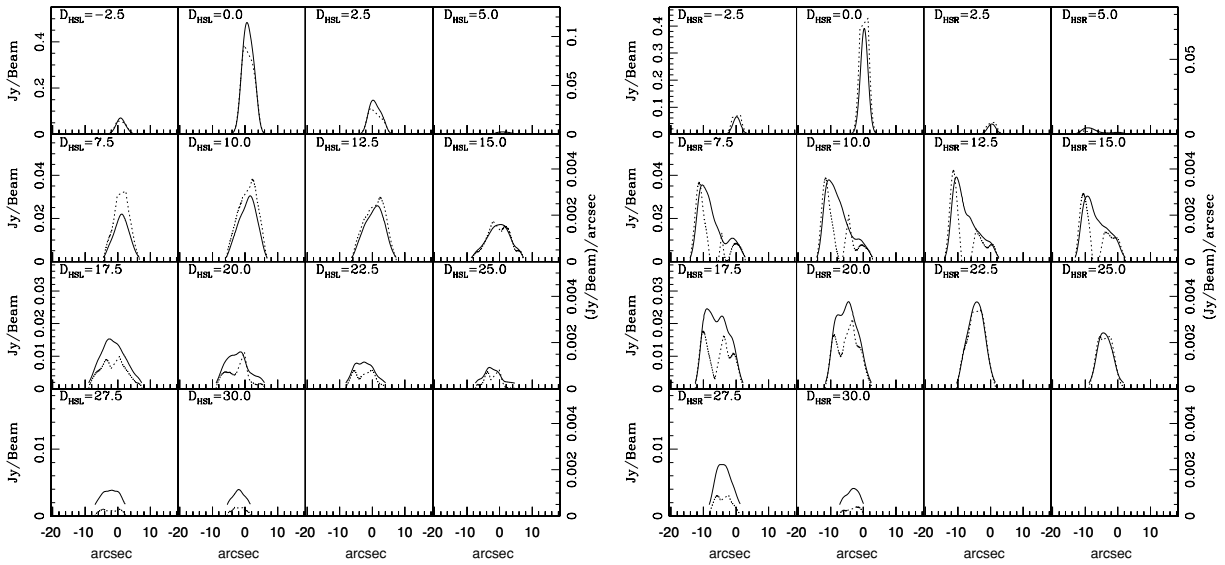


**Figure 105.** 3C172 emissivity (dotted line) and surface brightness (solid line) for each cross-sectional slice of the radio bridge at 1.4 GHz, as in Figure 5. A constant volume emissivity per slice provides a reasonable description of the data over most of the source.

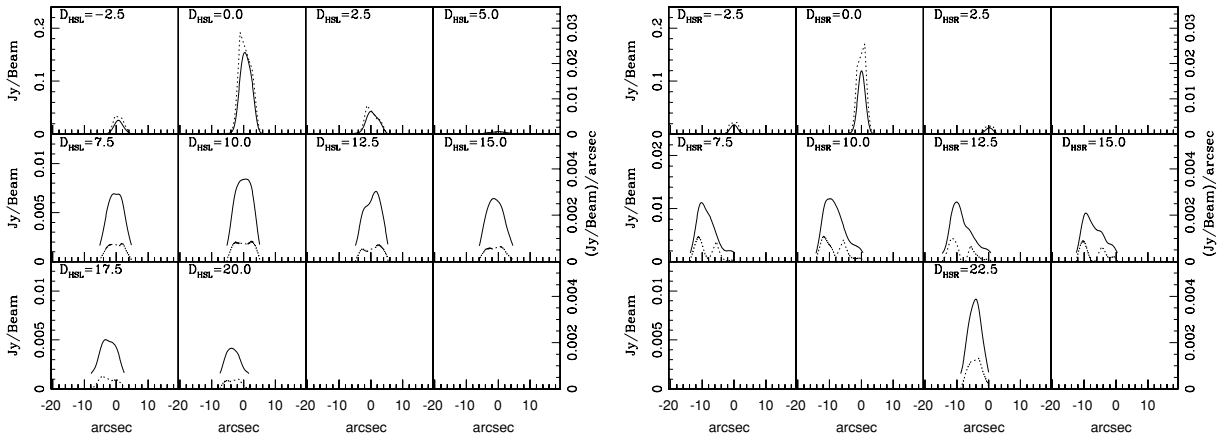


**Figure 106.** 3C172 emissivity (dotted line) and surface brightness (solid line) for each cross-sectional slice of the radio bridge at 5 GHz, as in Figure 105 but at 5 GHz. Results obtained at 5 GHz are nearly identical to those obtained at 1.4 GHz.

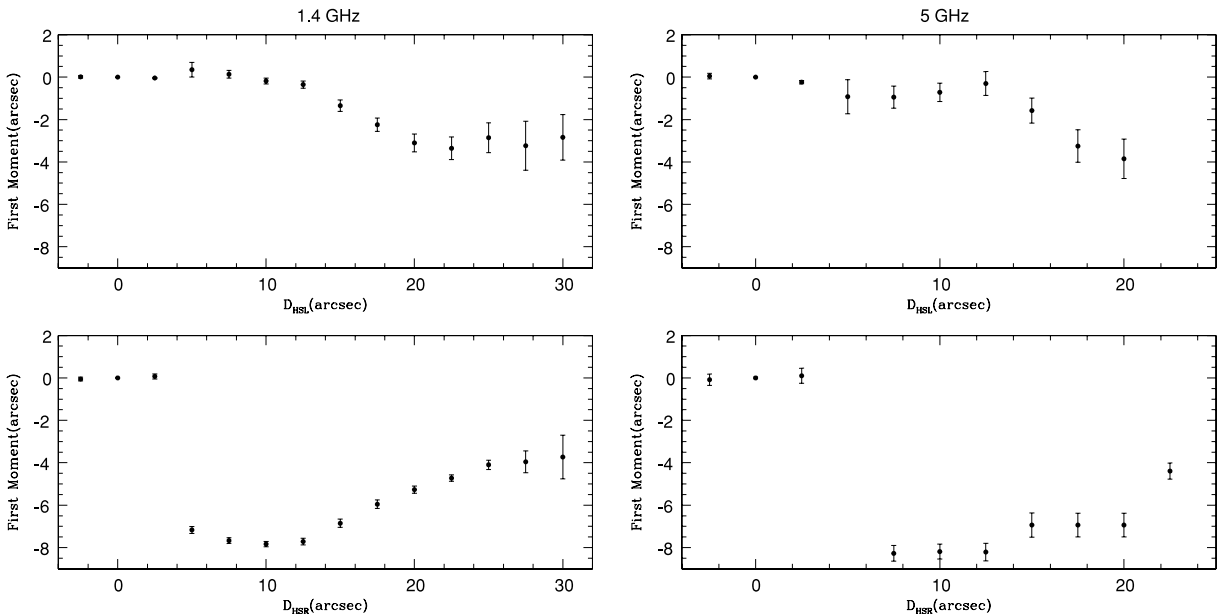


**Figure 107.** 3C172 first moment as a function of distance from the hot spot at 1.4 GHz and 5 GHz (left and right panels, respectively) for the left- and right-hand sides of the source (top and bottom, respectively).

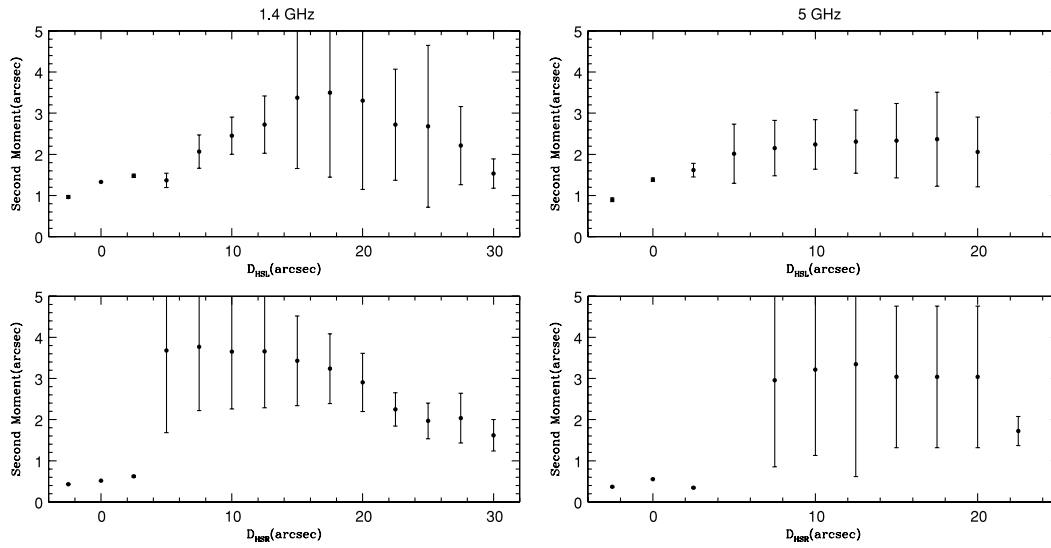


**Figure 108.** 3C172 second moment as a function of distance from the hot spot at 1.4 GHz and 5 GHz (left and right panels, respectively) for the left and right sides of the source (top and bottom panels, respectively).

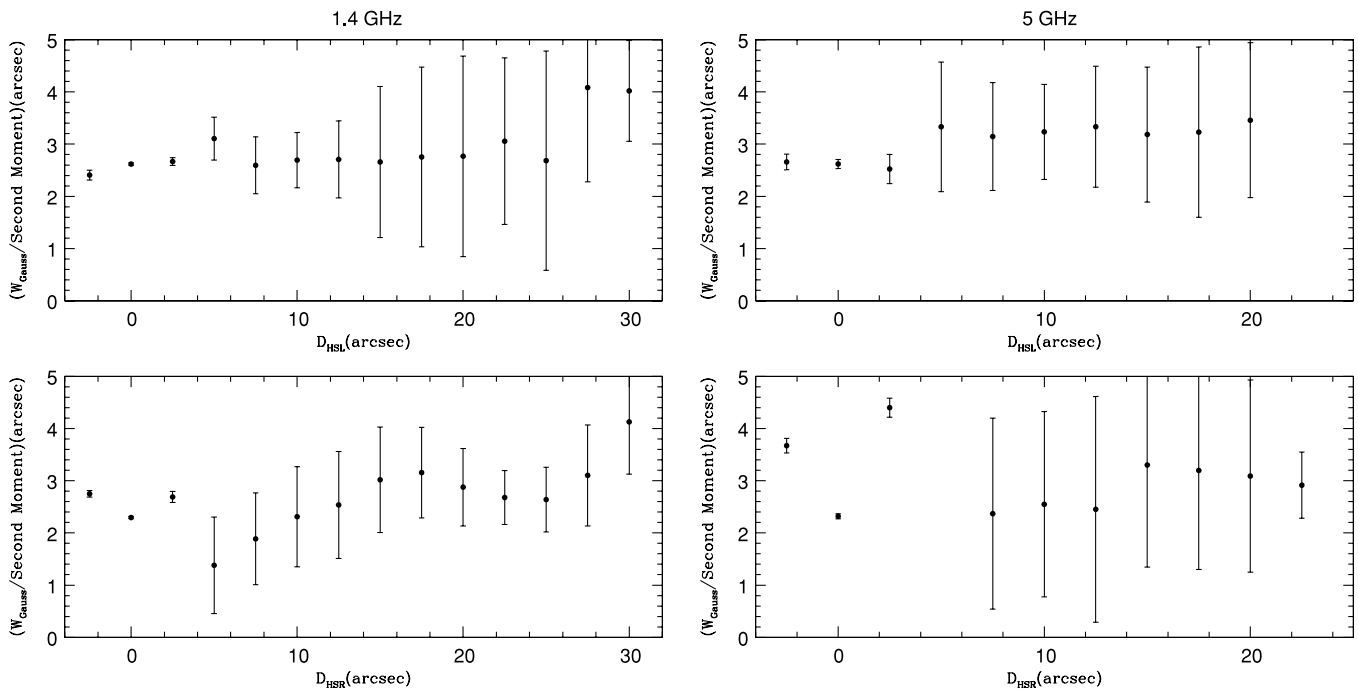


**Figure 109.** 3C172 ratio of the Gaussian FWHM to the second moment as a function of distance from the hot spot at 1.4 and 5 GHz (left and right panels, respectively) for the left- and right-hand sides of the source (top and bottom panels, respectively). The value of this ratio is fairly constant for each side of the source, and has a value of about 2.5. Similar results are obtained at 1.4 and 5 GHz.

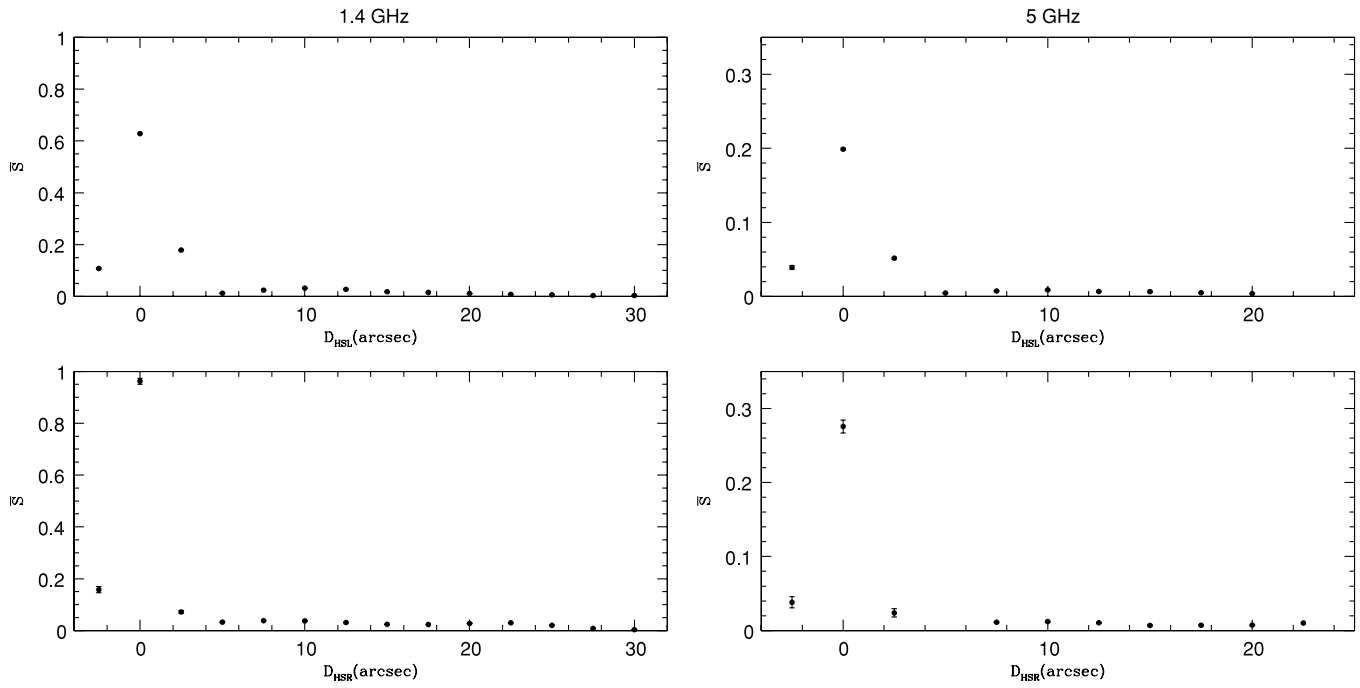


**Figure 110.** 3C172 average surface brightness in units of  $\text{Jy beam}^{-1}$  as a function of distance from the hot spot at 1.4 and 5 GHz (left and right panels, respectively) for the left- and right-hand sides of the source (top and bottom panels, respectively).

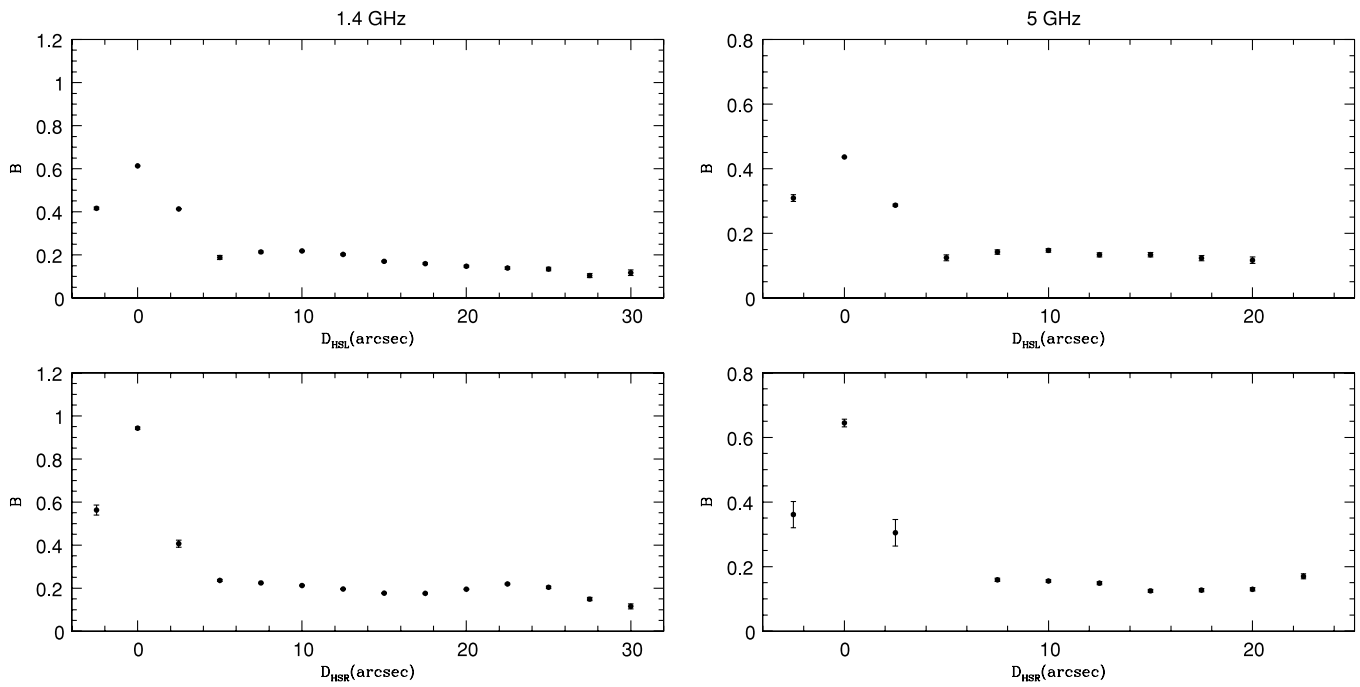


**Figure 111.** 3C172 minimum-energy magnetic field strength as a function of distance from the hot spot at 1.4 and 5 GHz (left and right panels, respectively) for the left- and right-hand sides of the source (top and bottom panels, respectively). The normalization is given in Table 1.

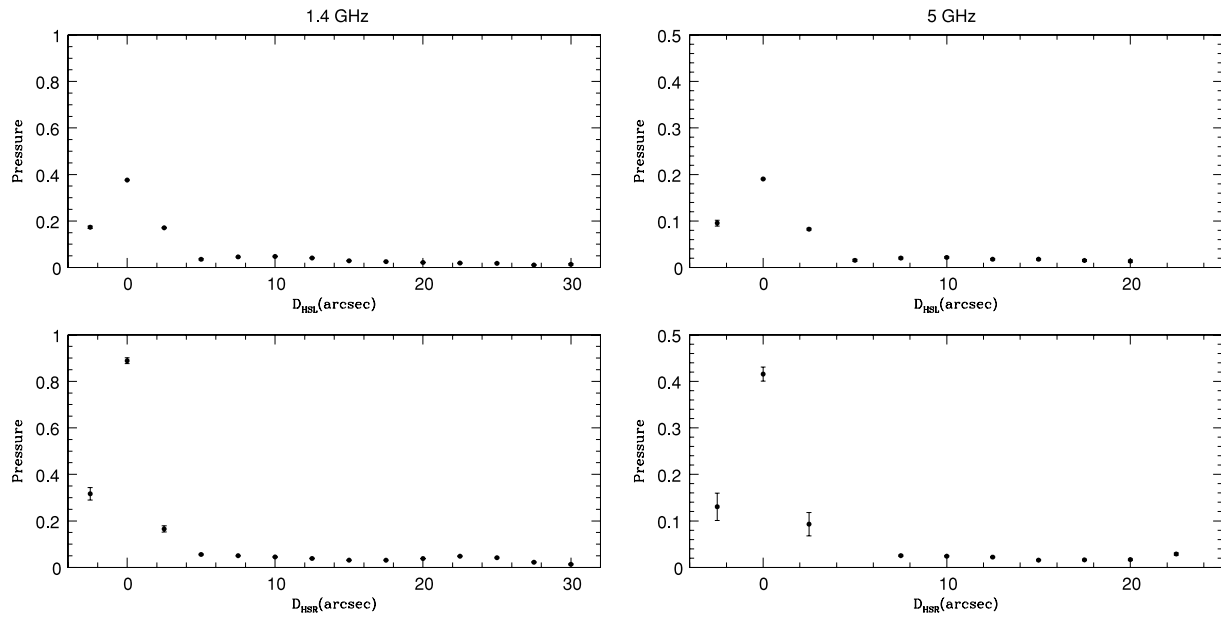


**Figure 112.** 3C172 minimum-energy pressure as a function of distance from the hot spot at 1.4 and 5 GHz (left and right panels, respectively) for the left- and right-hand sides of the source (top and bottom panels, respectively), as in Figure 12. The normalization is given in Table 1.

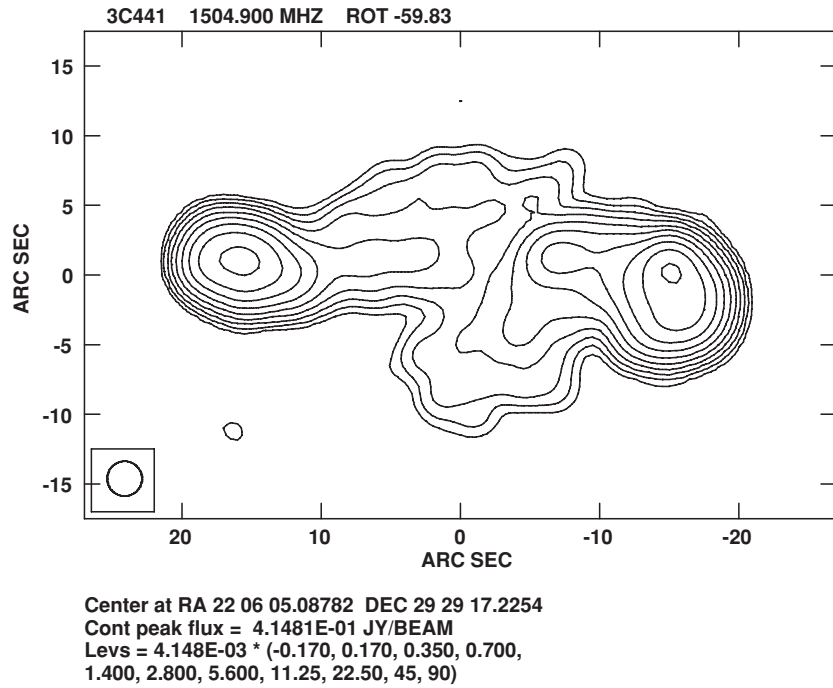


**Figure 113.** 3C441 at 1.4 GHz and 2.5 resolution rotated by 59.83 clockwise, as in Figure 1.

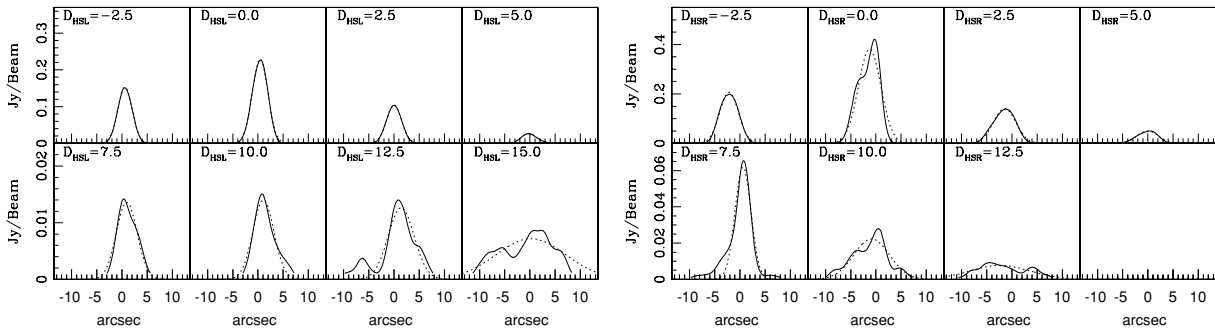


**Figure 114.** 3C441 surface brightness (solid line) and best-fit Gaussian (dotted line) for each cross-sectional slice of the radio bridge at 1.4 GHz, as in Figure 2. A Gaussian provides an excellent description of the surface brightness profile of each cross-sectional slice.

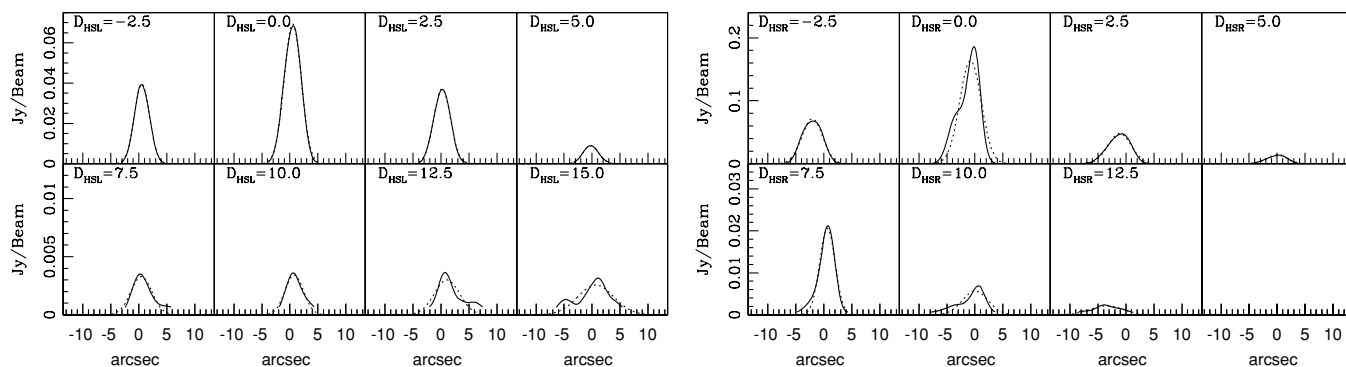


**Figure 115.** 3C441 surface brightness (solid line) and best-fit Gaussian (dotted line) for each cross-sectional slice of the radio bridge at 5 GHz, as in Figure 114 but at 5 GHz. Results obtained at 5 GHz are nearly identical to those obtained at 1.4 GHz.

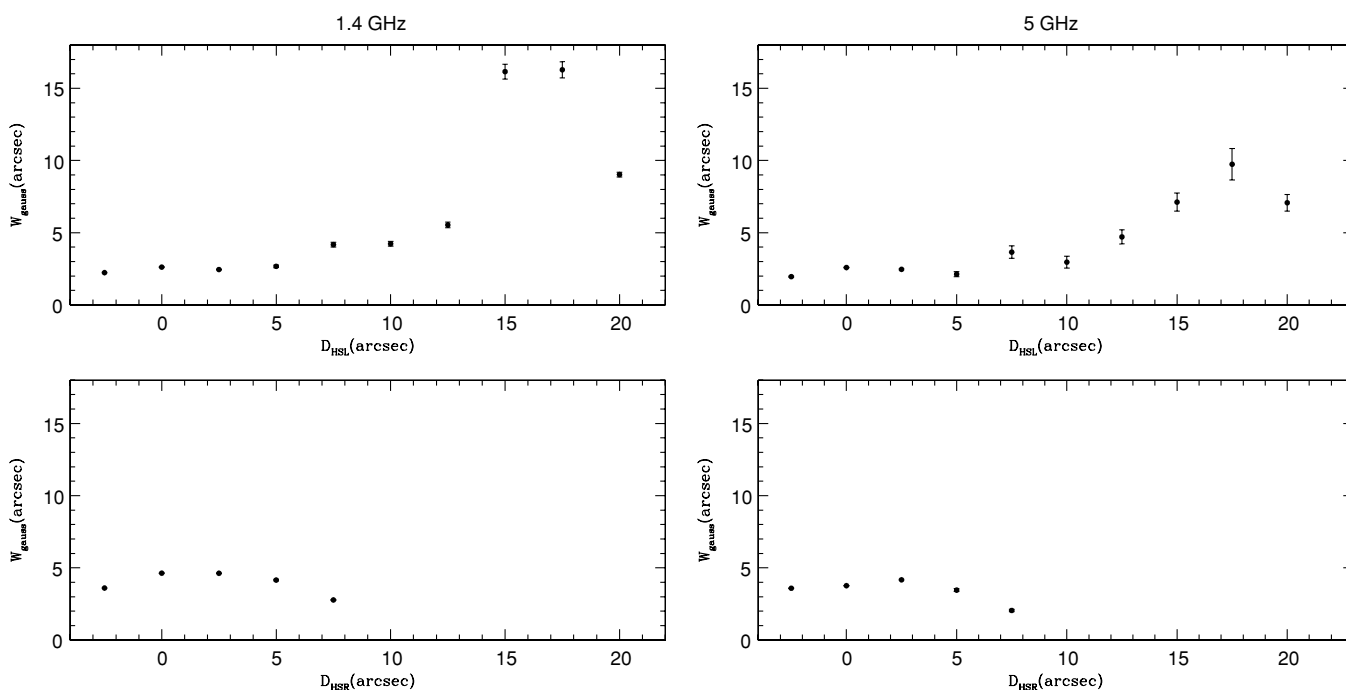


**Figure 116.** 3C441 Gaussian FWHM as a function of distance from the hot spot at 1.4 and 5 GHz (left and right panels, respectively) for the left- and right-hand sides of the source (top and bottom panels, respectively), as in Figure 4. The right- and left-hand sides of the source are somewhat symmetric. Similar results are obtained at 1.4 and 5 GHz.

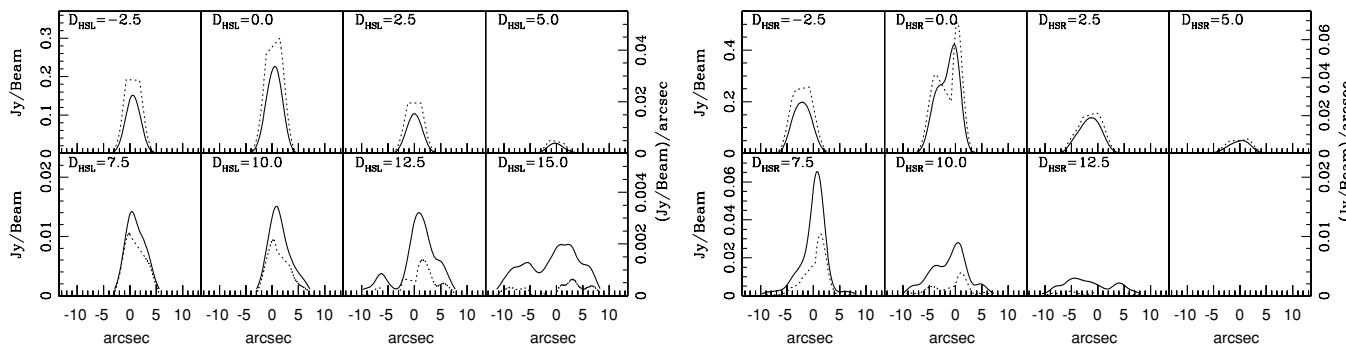


**Figure 117.** 3C441 emissivity (dotted line) and surface brightness (solid line) for each cross-sectional slice of the radio bridge at 1.4 GHz, as in Figure 5. A constant volume emissivity per slice provides a reasonable description of the data over most of the source.

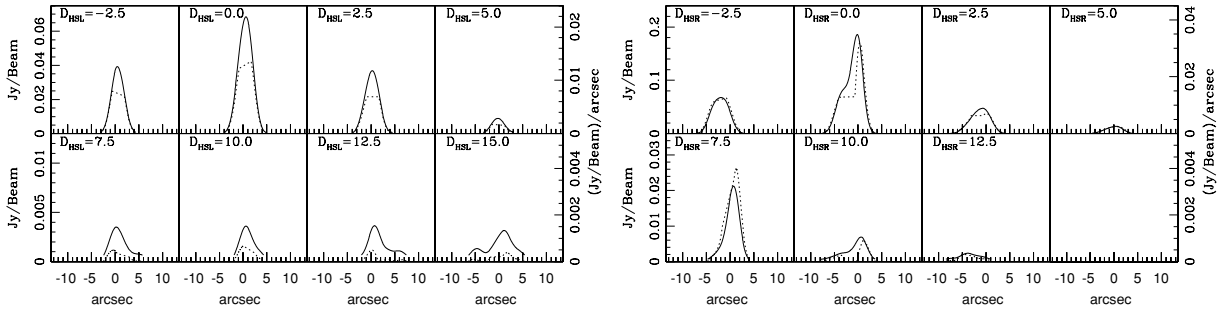


**Figure 118.** 3C441 emissivity (dotted line) and surface brightness (solid line) for each cross-sectional slice of the radio bridge at 5 GHz, as in Figure 117 but at 5 GHz. Results obtained at 5 GHz are nearly identical to those obtained at 1.4 GHz.

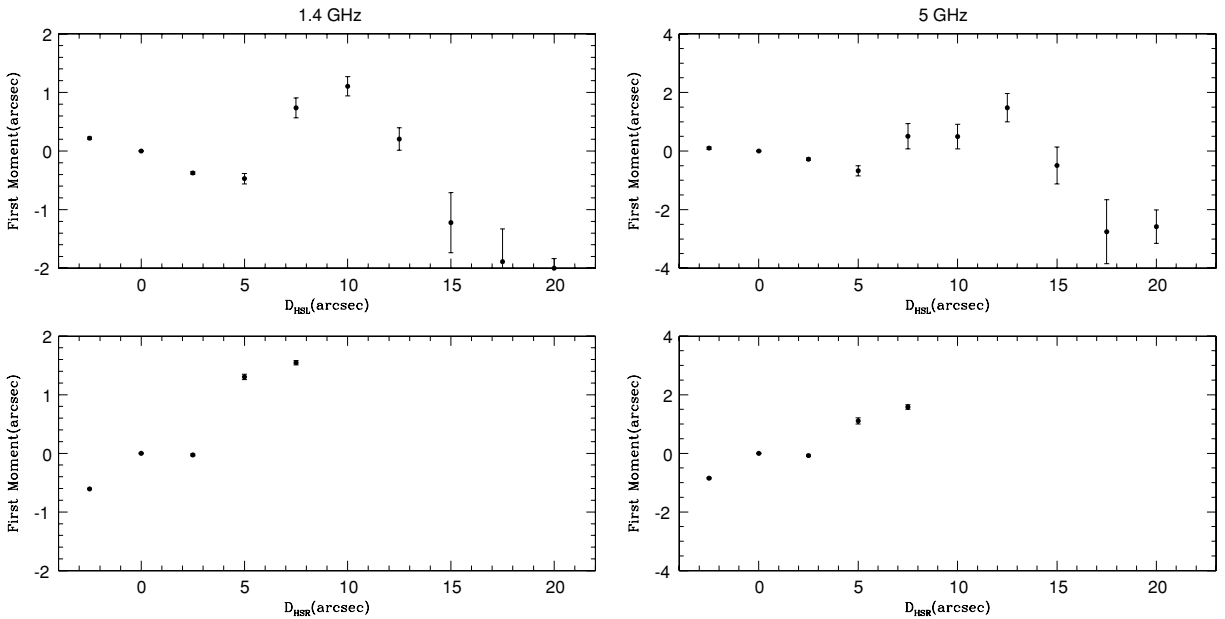


**Figure 119.** 3C441 first moment as a function of distance from the hot spot at 1.4 GHz and 5 GHz (left and right panels, respectively) for the left- and right-hand sides of the source (top and bottom, respectively).

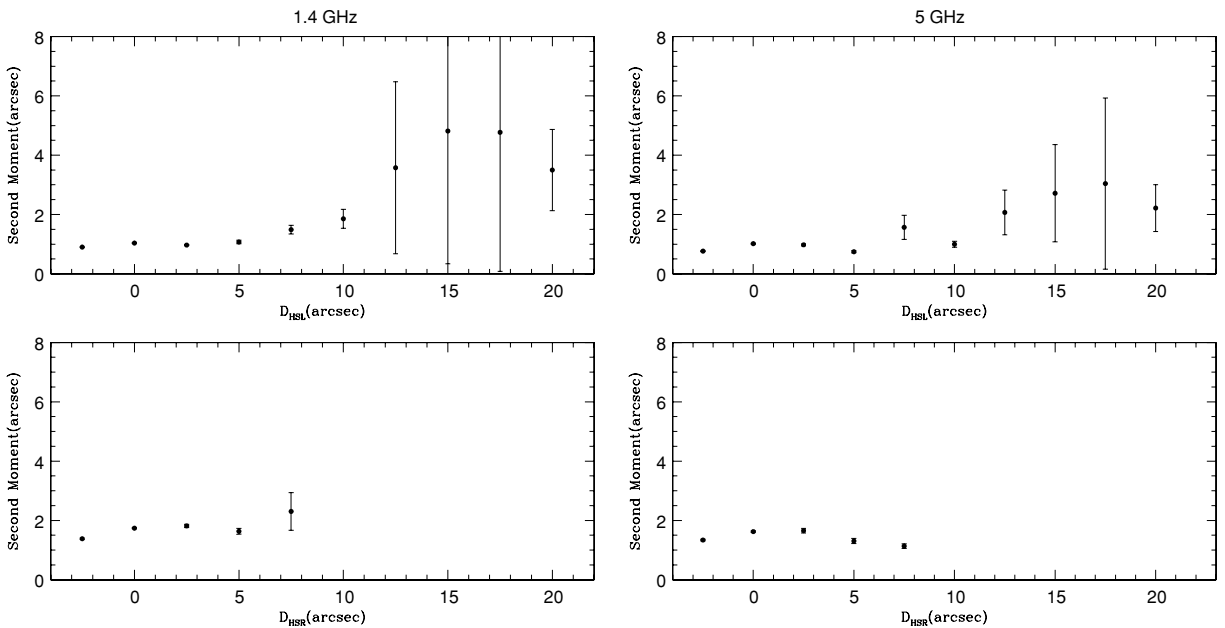


**Figure 120.** 3C441 second moment as a function of distance from the hot spot at 1.4 GHz and 5 GHz (left and right panels, respectively) for the left and right sides of the source (top and bottom panels, respectively).

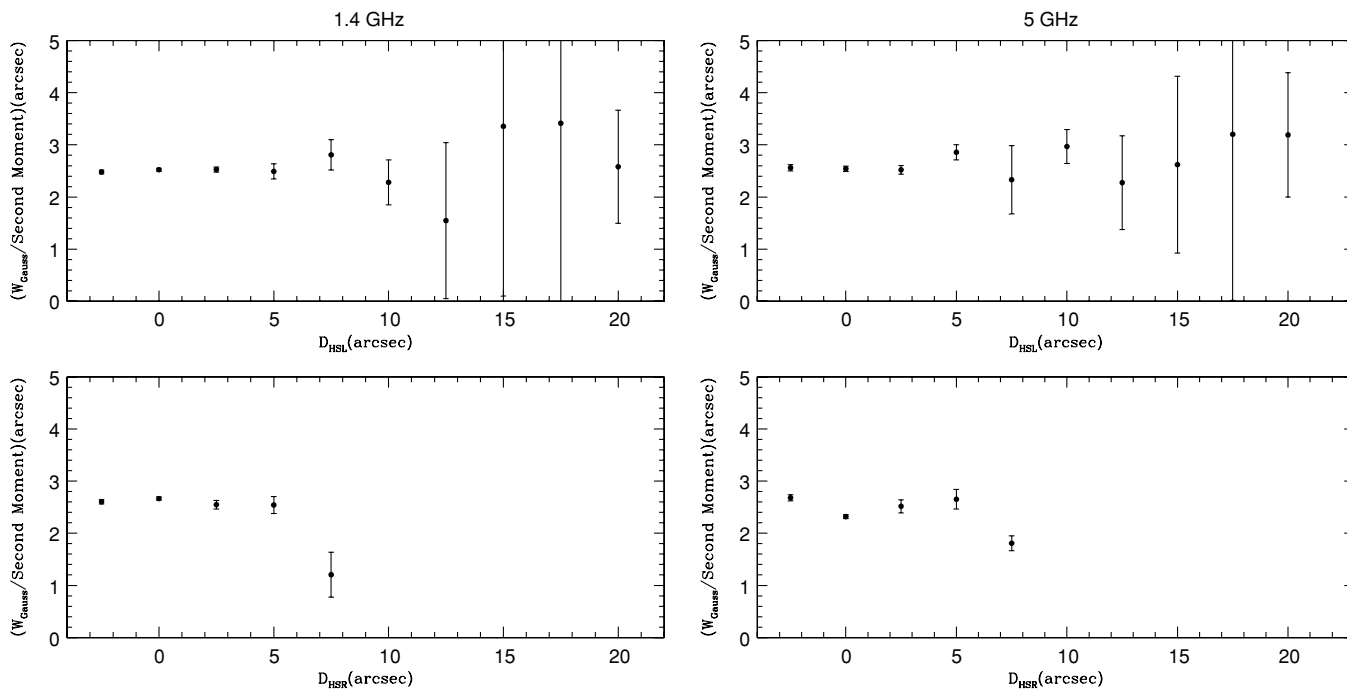


**Figure 12.1.** 3C441 ratio of the Gaussian FWHM to the second moment as a function of distance from the hot spot at 1.4 and 5 GHz (left and right panels, respectively) for the left- and right-hand sides of the source (top and bottom panels, respectively). The value of this ratio is fairly constant for each side of the source, and has a value of about 2.5. Similar results are obtained at 1.4 and 5 GHz.

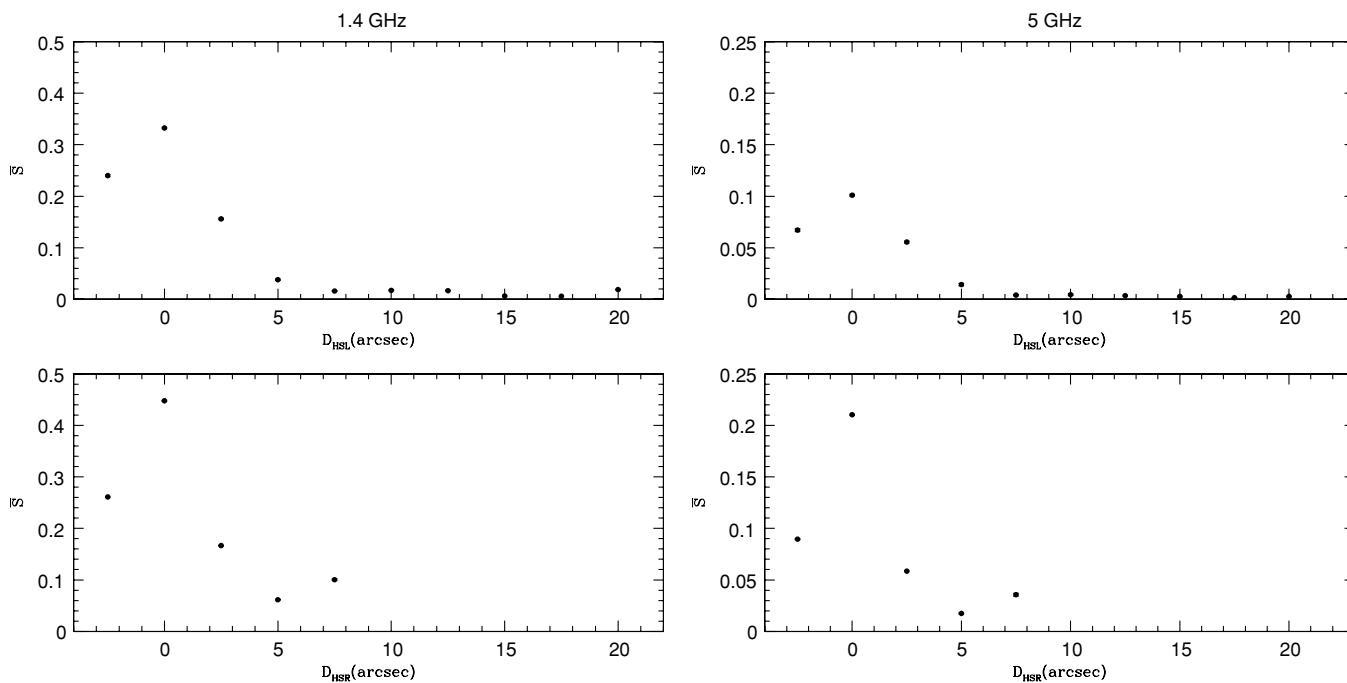


**Figure 12.2.** 3C441 average surface brightness in units of  $\text{Jy beam}^{-1}$  as a function of distance from the hot spot at 1.4 and 5 GHz (left and right panels, respectively) for the left- and right-hand sides of the source (top and bottom panels, respectively).

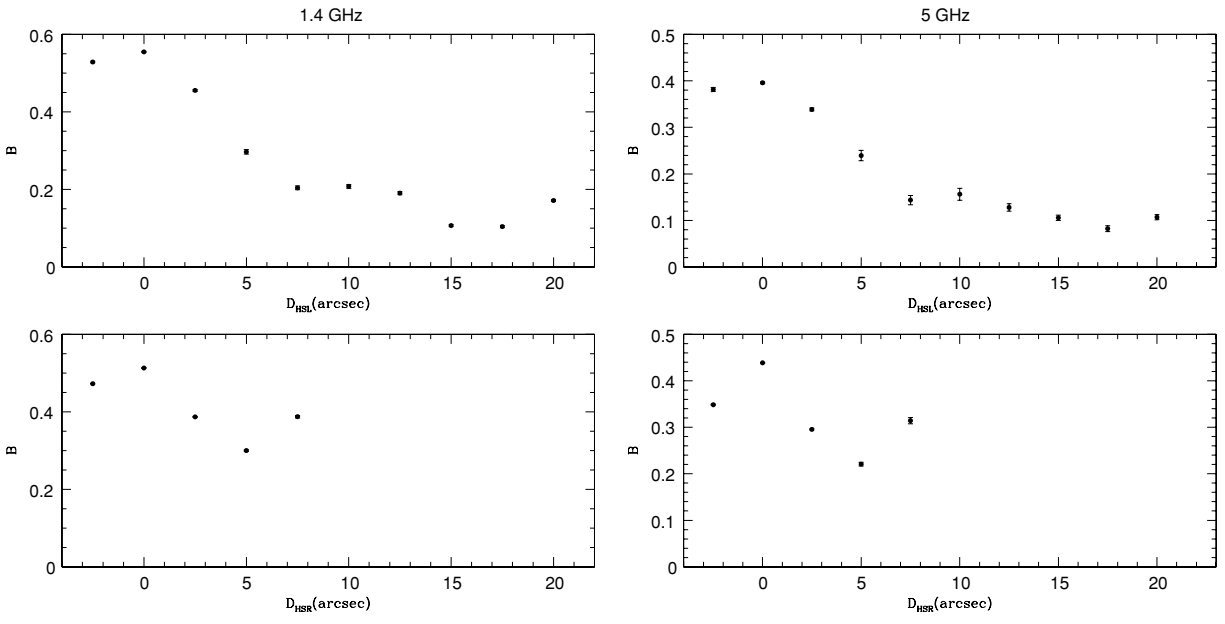


**Figure 123.** 3C441 minimum-energy magnetic field strength as a function of distance from the hot spot at 1.4 and 5 GHz (left and right panels, respectively) for the left- and right-hand sides of the source (top and bottom panels, respectively). The normalization is given in Table 1.

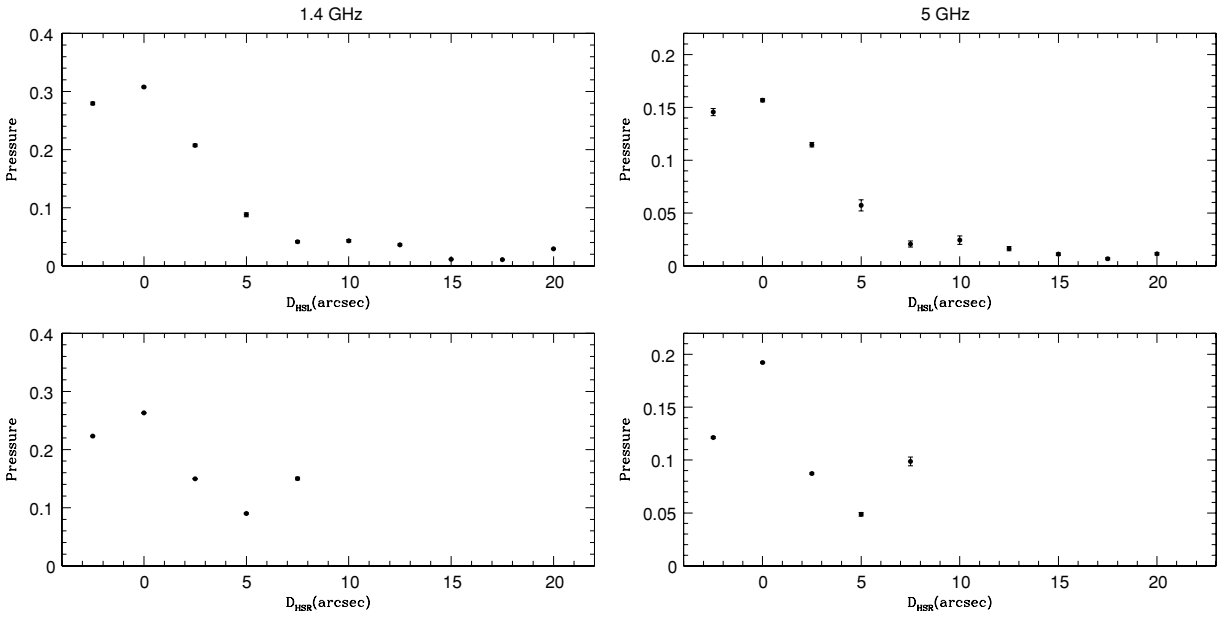


**Figure 124.** 3C441 minimum-energy pressure as a function of distance from the hot spot at 1.4 and 5 GHz (left and right panels, respectively) for the left- and right-hand sides of the source (top and bottom panels, respectively), as in Figure 12. The normalization is given in Table 1.

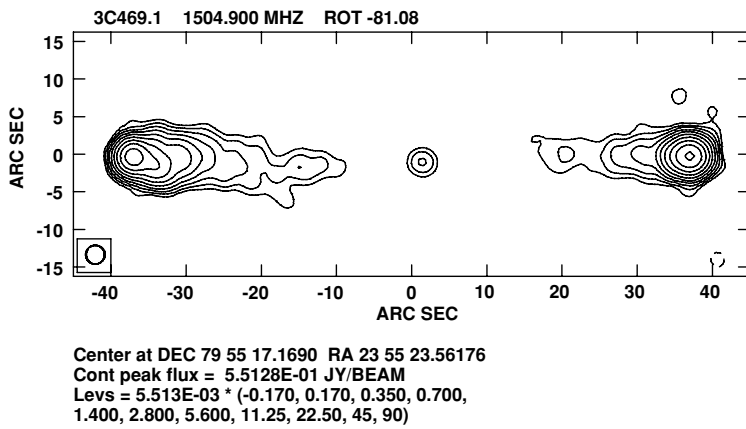


**Figure 125.** 3C469.1 at 1.4 GHz and 2'' resolution rotated by 81°08 clockwise, as in Figure 1.

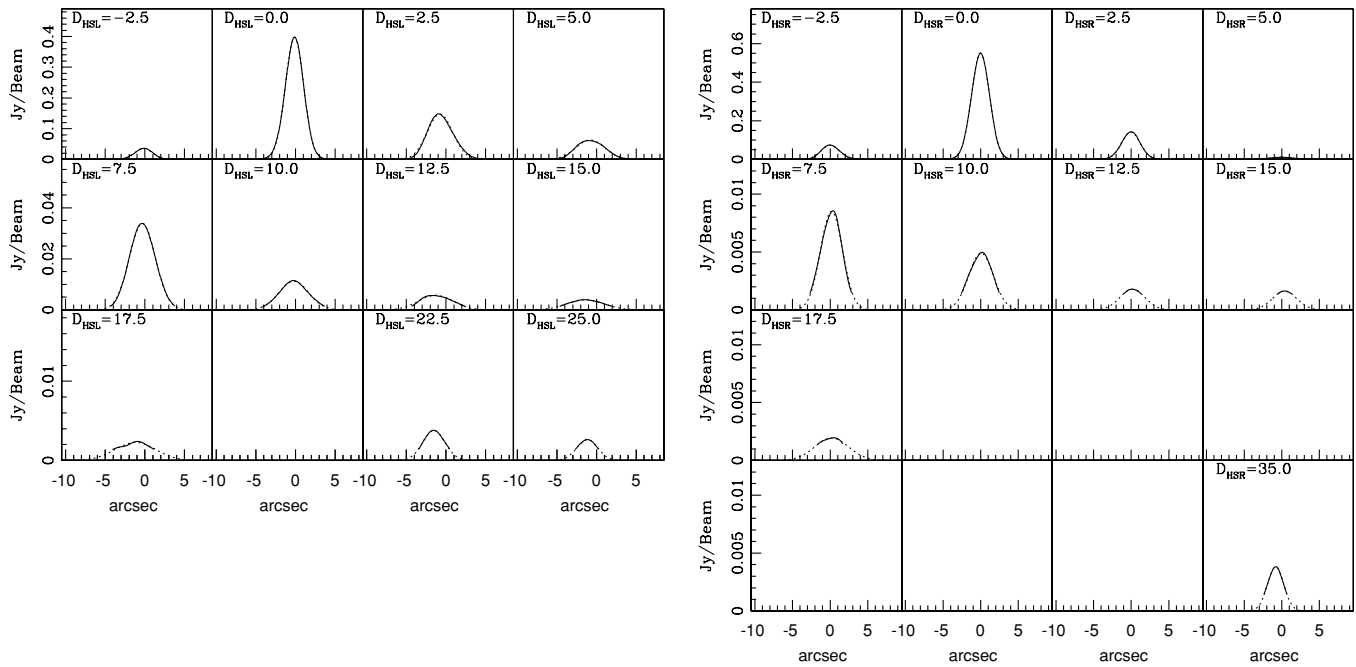


**Figure 126.** 3C469.1 surface brightness (solid line) and best-fit Gaussian (dotted line) for each cross-sectional slice of the radio bridge at 1.4 GHz, as in Figure 2. A Gaussian provides an excellent description of the surface brightness profile of each cross-sectional slice.

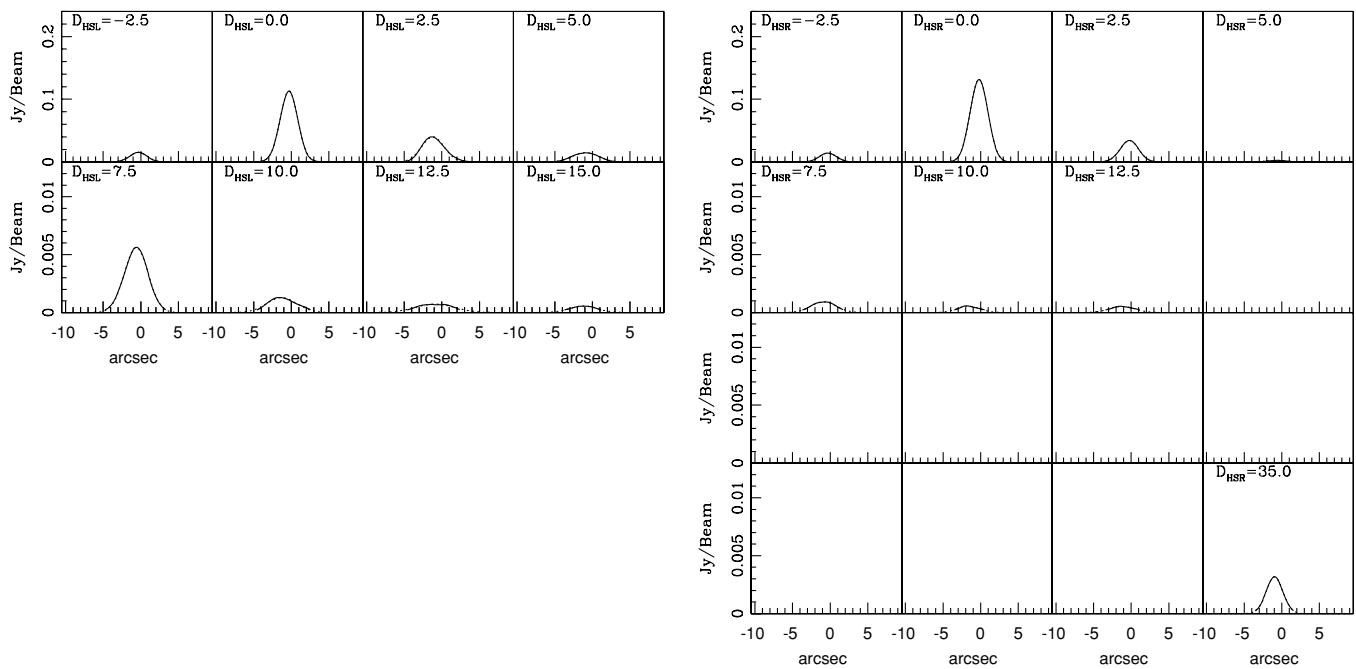


**Figure 127.** 3C469.1 surface brightness (solid line) and best-fit Gaussian (dotted line) for each cross-sectional slice of the radio bridge at 5 GHz, as in Figure 126 but at 5 GHz. Results obtained at 5 GHz are nearly identical to those obtained at 1.4 GHz.

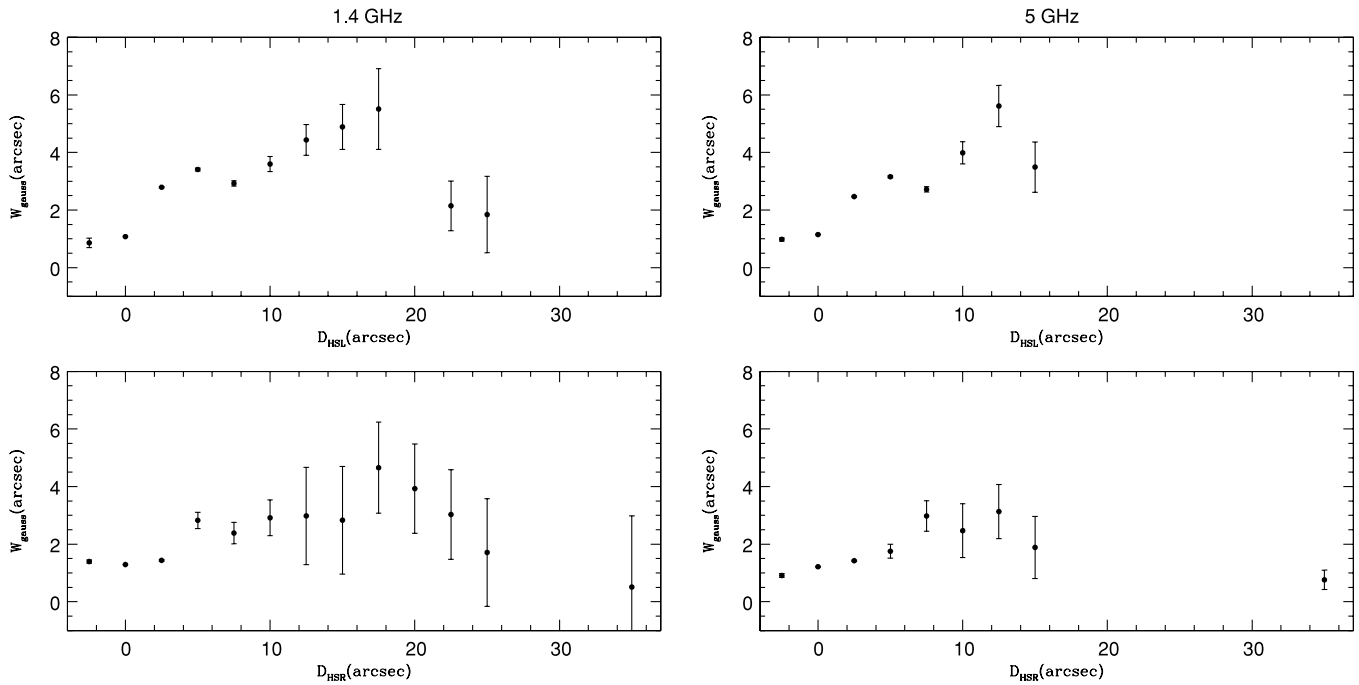


**Figure 128.** 3C469.1 Gaussian FWHM as a function of distance from the hot spot at 1.4 and 5 GHz (left and right panels, respectively) for the left- and right-hand sides of the source (top and bottom panels, respectively), as in Figure 4. The right- and left-hand sides of the source are somewhat symmetric. Similar results are obtained at 1.4 and 5 GHz.

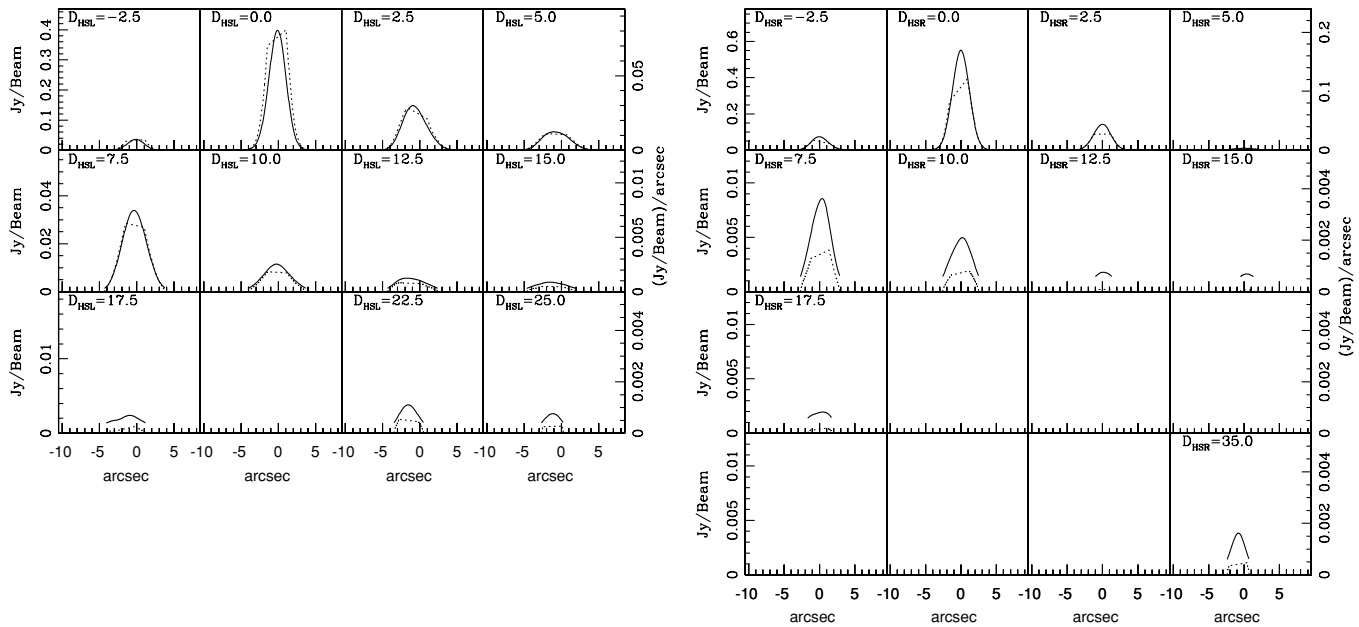


**Figure 129.** 3C469.1 emissivity (dotted line) and surface brightness (solid line) for each cross-sectional slice of the radio bridge at 1.4 GHz, as in Figure 5. A constant volume emissivity per slice provides a reasonable description of the data over most of the source.

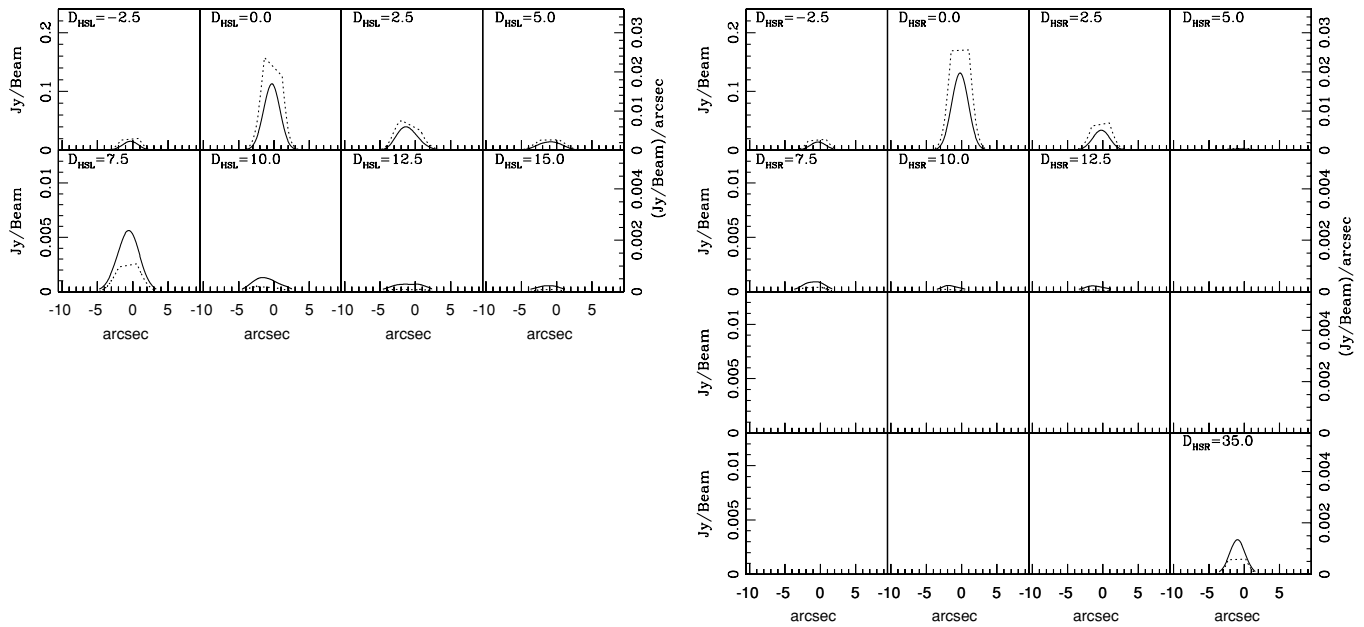


**Figure 130.** 3C469.1 emissivity (dotted line) and surface brightness (solid line) for each cross-sectional slice of the radio bridge at 5 GHz, as in Figure 129 but at 5 GHz. Results obtained at 5 GHz are nearly identical to those obtained at 1.4 GHz.

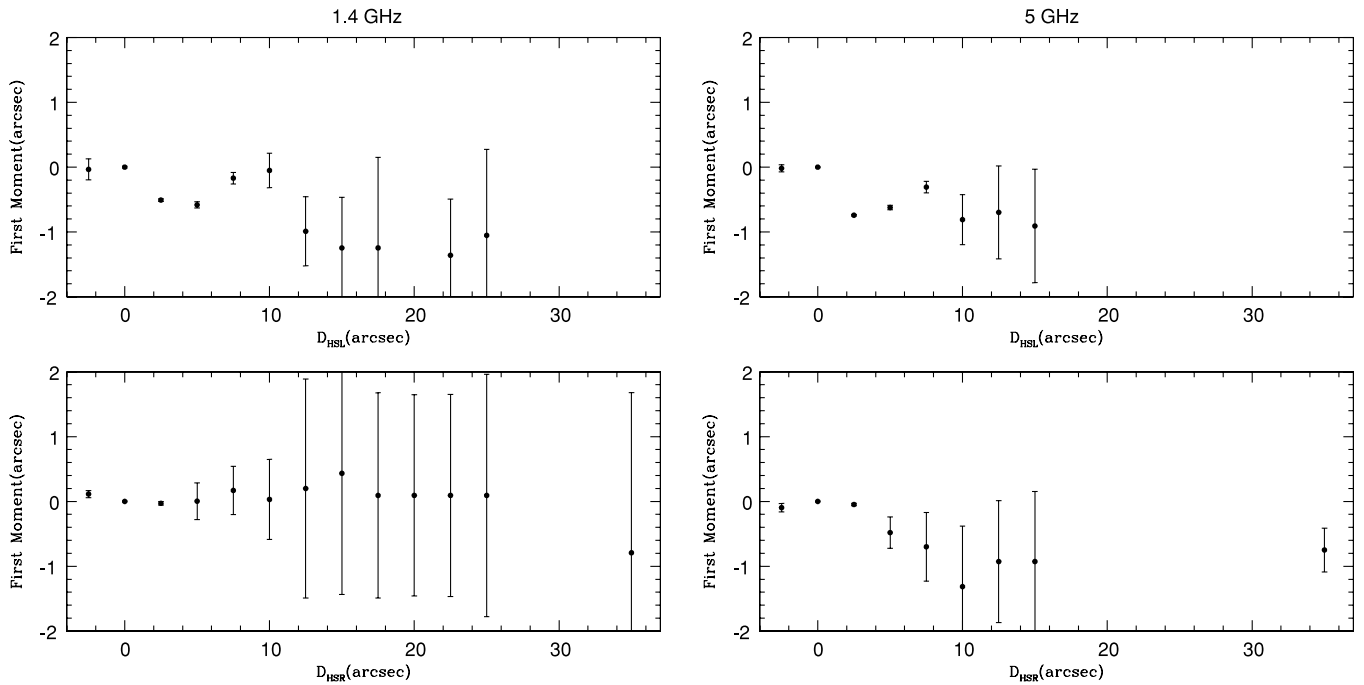


**Figure 131.** 3C469.1 first moment as a function of distance from the hot spot at 1.4 GHz and 5 GHz (left and right panels, respectively) for the left- and right-hand sides of the source (top and bottom, respectively).

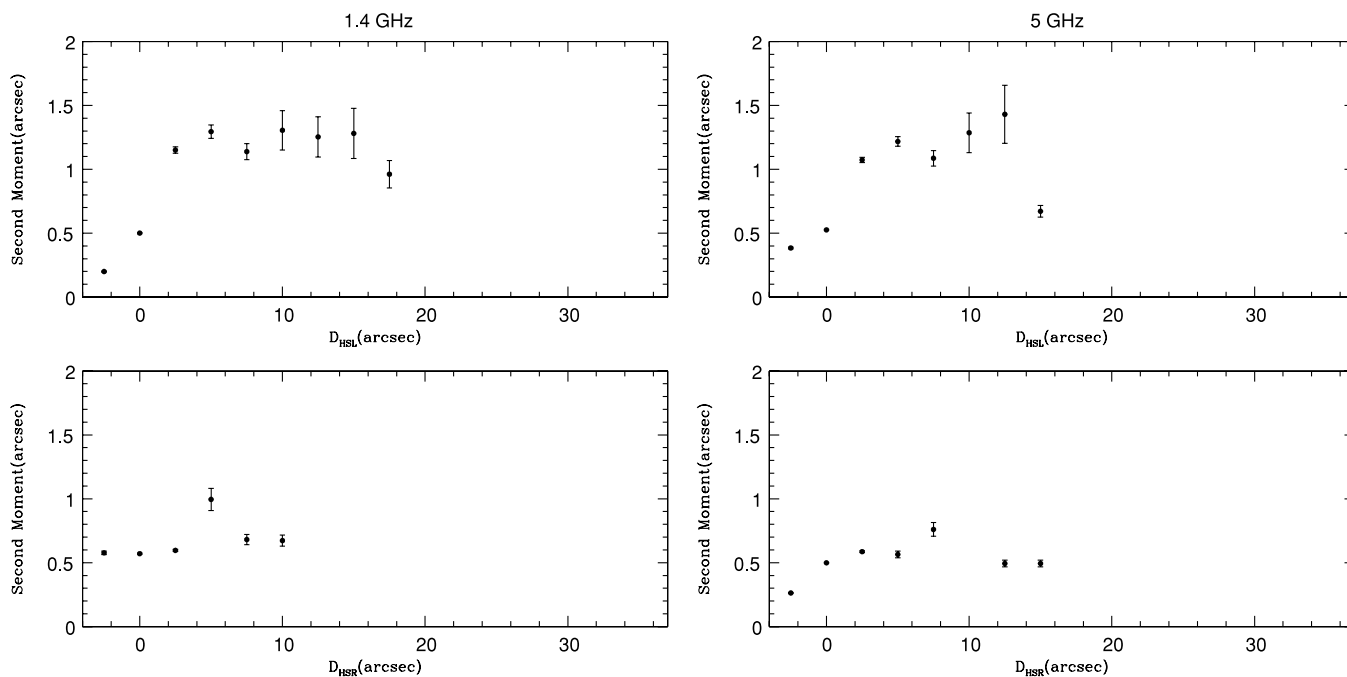


**Figure 132.** 3C469.1 second moment as a function of distance from the hot spot at 1.4 GHz and 5 GHz (left and right panels, respectively) for the left and right sides of the source (top and bottom panels, respectively).

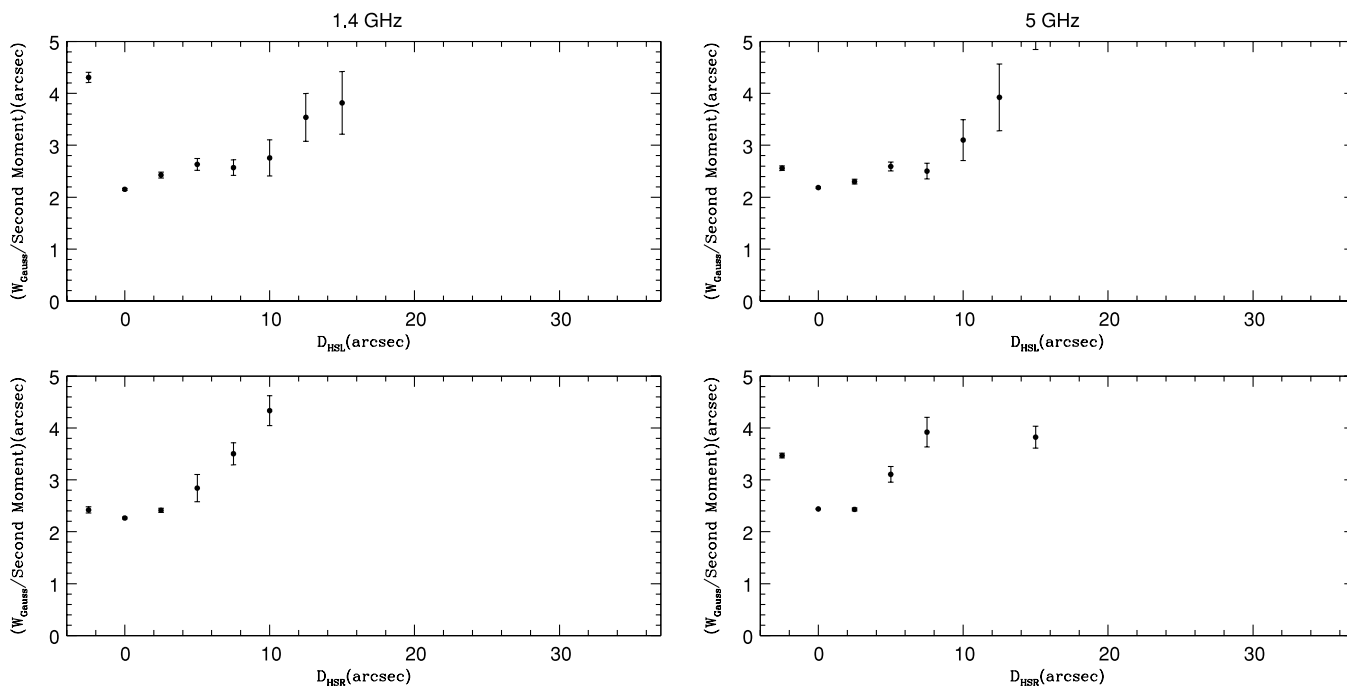


**Figure 133.** 3C469.1 ratio of the Gaussian FWHM to the second moment as a function of distance from the hot spot at 1.4 and 5 GHz (left and right panels, respectively) for the left- and right-hand sides of the source (top and bottom panels, respectively). The value of this ratio shifts across each side of the source, and has a value of about 2–3. Similar results are obtained at 1.4 and 5 GHz.

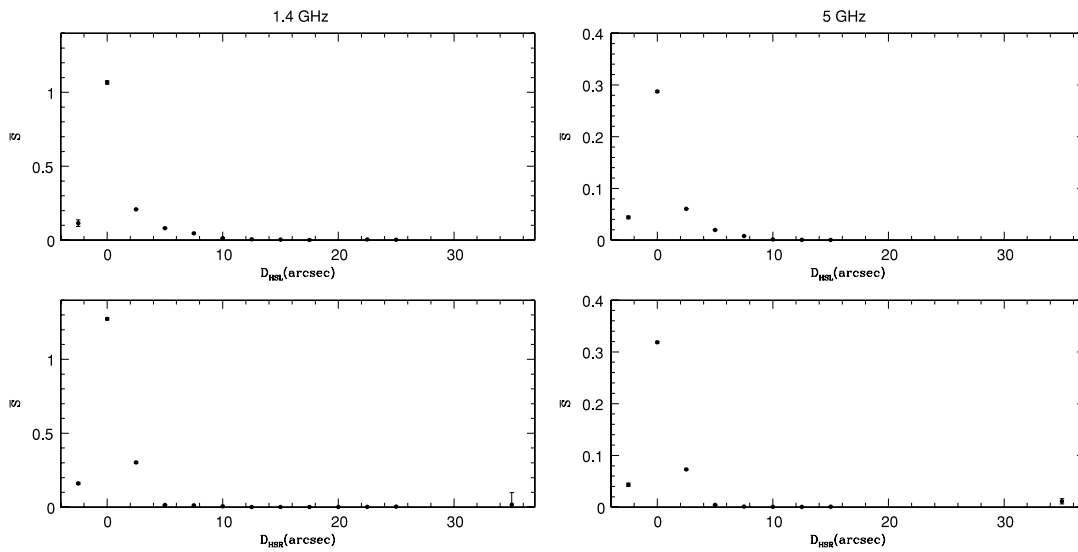


**Figure 134.** 3C469.1 average surface brightness in units of  $\text{Jy beam}^{-1}$  as a function of distance from the hot spot at 1.4 and 5 GHz (left and right panels, respectively) for the left- and right-hand sides of the source (top and bottom panels, respectively).

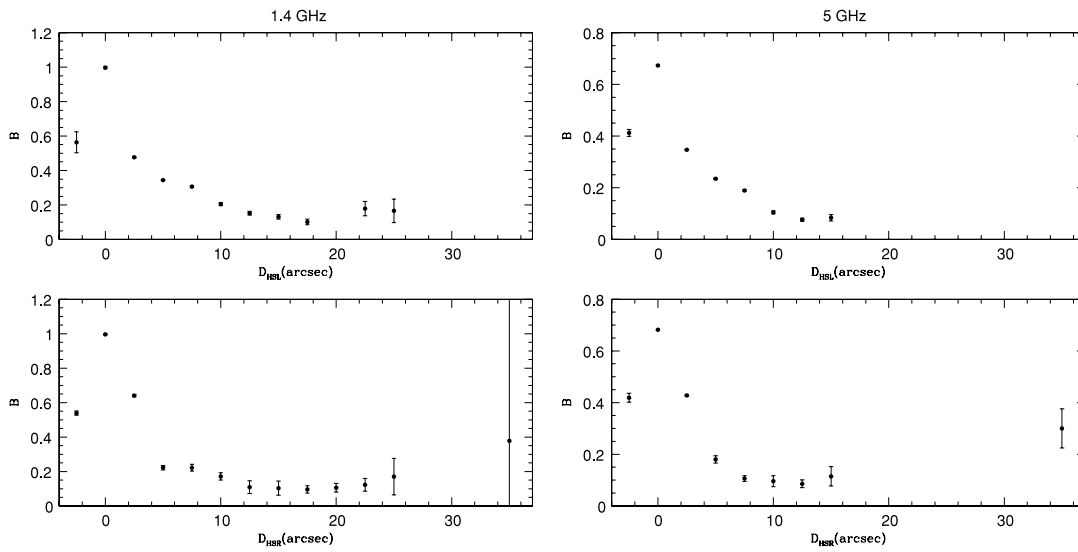


**Figure 135.** 3C469.1 minimum-energy magnetic field strength as a function of distance from the hot spot at 1.4 and 5 GHz (left and right panels, respectively) for the left- and right-hand sides of the source (top and bottom panels, respectively). The normalization is given in Table 1.

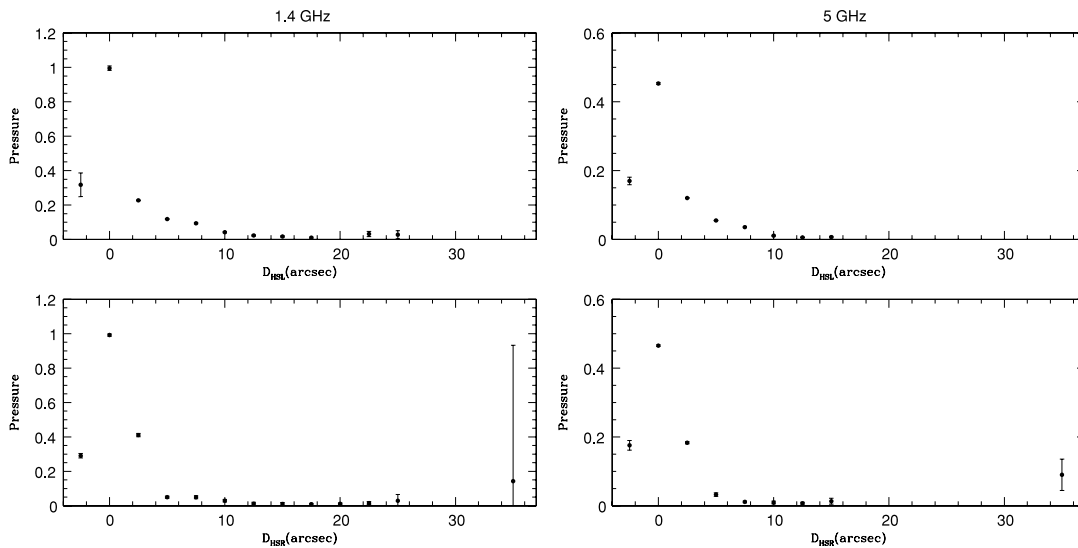


**Figure 136.** 3C469.1 minimum-energy pressure as a function of distance from the hot spot at 1.4 and 5 GHz (left and right panels, respectively) for the left- and right-hand sides of the source (top and bottom panels, respectively), as in Figure 12. The normalization is given in Table 1.

1. Gaussian Fits: each cross-sectional slice was fit with a Gaussian and these Gaussian fits and the FWHM of the Gaussian,  $W_G$ , were studied as a function of distance from the hot spot. A Gaussian provides a very good description of the surface brightness profile for most slices. The lobe width  $W_G$  as a function of distance from the hot spot was very similar for each side of a given source, indicating a high degree of symmetry relative to the hot spot positions. This suggests that the properties of the ambient medium are symmetric about the source center and the properties of the twin jets at any given time are quite similar.

Many of the widths first increase and then decrease with distance from the hot spot. The position of the local maxima seems to be related to the pressure profile of the source and is sometimes related to the properties of the radio emissivity.

2. Radio Emissivity: the radio emissivity,  $\epsilon_v$ , may be obtained by noting  $\epsilon_v \propto S_v/l$ , where  $S_v$  is the radio surface brightness and  $l$  is the path length, and assuming that at a given distance  $r$  from the slice center the emissivity is constant over a thin semi-circular shell at radius  $r$ . By starting at the top or bottom of the slice and stepping in, the emissivity may be obtained at each distance  $r$  for the top and bottom halves of the slice. The results obtained for the top and bottom halves are independent. For most slices, the emissivity near the center of the slice is continuous, indicating that the emissivity obtained there by stepping in from the top and bottom of the source match, and suggesting that the assumption of semi-cylindrical symmetry is valid for that slice.

The emissivities of many slices are fairly flat, indicating a region of constant emissivity. Some of the slices indicate an “edge-peaked” emissivity that can include a minimum emissivity near the source center. When these are detected, the slices seem to be located near the local maxima of the radio bridge width. Taken at face value, they suggest that the pressure of the slice is a minimum at the slice center and larger near the edge of the slice since the pressure goes roughly as the square root of the emissivity. This is the type of behavior expected as pressure waves carry information about the pressure of the external medium into the relativistic fluid. No signature of a jet-like feature that could produce a central peak of an emissivity profile that propagates through adjacent slices is seen.

3. The First Moment: the first moment of each slice was obtained and studied as a function of distance from the hot spot. A first moment of zero would indicate that the surface brightness peak of each slice lies along the symmetry axis of the source. The first moment is found to wander from zero by very small amounts: typically less than  $1''$ – $2''$  over distances of about  $10''$ – $20''$ . The first moment may be taken as an indication of the location of the hot spot at an earlier stage of the source lifetime. Deviations of the first moment from the current symmetry axis of the source could be caused by actual deviations of the location of the hot spot from the current symmetry axis, or by many other processes. One such process is the motion of the source relative to the ambient gas. Measurements of the deviations of the first moment from zero were used to place bounds on the velocity of the source relative to the ambient gas in the direction perpendicular to the source symmetry axis, and the results suggest that this velocity must be less than or equal to about  $10^3 \text{ km s}^{-1}$  or so. Measurements of the first moment can also be used to place limits on the angle over

which the outflow axis could have shifted relative to the ambient gas, and the results suggest that this angle must be less than a few to 10 degrees.

4. The Second Moment: the second moment was obtained and compared with the Gaussian width. The two were found to indicate a similar source shape since their ratio is fairly constant. The value of this ratio is typically close to what is expected for the emissivity profiles obtained.

5. Mean Surface Brightness, Magnetic Field Strength, and Pressure: average values of the surface brightness, minimum-energy magnetic field strength, and pressure were obtained for each slice. The surface brightness peaks at the location of the hot spot, and remains fairly constant across the rest of the source. The magnetic field strength and pressure also peak at the hot spot, and decrease in value as the distance from the hot spot increases. At some distance from the hot spot they seem to reach a roughly constant value and remain fairly constant for distances greater than this, suggesting that equilibrium is being approached or reached. Interestingly, the pressures seem to level off at a distance from the hot spot that is located just before the local maxima of the bridge width.

The results obtained may be interpreted as the response of the system to the large pressure difference between the hot spot and the ambient gas, as discussed in Sections 2.2 and 2.5. In the rest frame of the hot spot, the problem is somewhat like that of an outflow entering a region of low external pressure, which has been explored for a relativistic fluid by Königl (1980) and Daly & Marscher (1988). The fluid expands in the lateral direction as information about the external pressure propagates into the relativistic fluid. At the point of maximal expansion, the pressure is a minimum near the symmetry axis of the source, and is largest at the source edges. In the ideal case studied by Königl and Daly & Marscher, this pattern continues, but in the sources studied here, the data suggest that pressure waves are able to bring the source into rough pressure equilibrium downstream of this location for most of the sources studied.

This work was supported in part by U.S. National Science Foundation grant AST-0507465 (R.A.D.). The National Radio Astronomy Observatory is a facility of the National Science Foundation operated under cooperative agreement by Associated Universities, Inc. This research has made use of the NASA/IPAC Extragalactic Database (NED) which is operated by the Jet Propulsion Laboratory, California Institute of Technology, under contract with the National Aeronautics and Space Administration.

## REFERENCES

- Alexander, P. 1987, *MNRAS*, **225**, 27  
 Alexander, P., & Leahy, J. P. 1987, *MNRAS*, **225**, 1  
 Best, P. N., Longair, M. S., & Rottgering, H. J. A. 1997, *MNRAS*, **286**, 785  
 Blundell, K. M., Rawlings, S., & Willott, C. J. 1999, *AJ*, **117**, 677  
 Burbidge, G. R. 1956, *ApJ*, **124**, 416  
 Carilli, C. L., Perley, R. A., Dreher, J. W., & Leahy, J. P. 1991, *ApJ*, **383**, 554  
 Carvalho, J. C., Daly, R. A., Mory, M. P., & O’Dea, C. P. 2005, *ApJ*, **620**, 126  
 Courant, R., & Friedrichs, K. O. 1948, *Supersonic Flow and Shock Waves* (New York: Wiley Interscience)  
 Daly, R. A., Djorgovski, S. G., Freeman, K. A., Mory, M. P., O’Dea, C. P., Kharb, P., & Baum, S. A. 2008, *ApJ*, **677**, 1  
 Daly, R. A., & Marscher, A. P. 1988, *ApJ*, **334**, 539  
 Daly, R. A., Mory, M. P., O’Dea, C. P., Kharb, P., Baum, S. A., Guerra, E. J., & Djorgovski, S. G. 2009, *ApJ*, **691**, 1058

- Eilek, J. A., Melrose, D. B., & Walker, M. A. 1997, *ApJ*, **483**, 282
- Fanaroff, B. L., & Riley, J. M. 1974, *MNRAS*, **167**, 31P
- Goodlet, J. A., Kaiser, C. R., Best, P. N., & Dennett-Thorpe, J. 2004, *MNRAS*, **347**, 508
- Guerra, E. J., Daly, R. A., & Wan, L. 2000, *ApJ*, **544**, 659
- Jamrozy, M., Konar, C., Machalski, J., & Saikia, D. J. 2008, *MNRAS*, **385**, 1286
- Kaiser, C. R. 2000, *A&A*, **362**, 447
- Kharb, P., O'Dea, C., Baum, S., Daly, R., Mory, M., Donahue, M., & Guerra, E. 2008, *ApJS*, **174**, 74
- Konar, C., Hardcastle, M. J., Croston, J. H., & Saikia, D. J. 2009, *MNRAS*, **400**, 480
- Königl, A. 1980, *Phys. Fluids*, **23**, 1083
- Leahy, J. P., Muxlow, T. W. B., & Stephens, P. W. 1989, *MNRAS*, **239**, 401
- Leahy, J. P., & Williams, A. G. 1984, *MNRAS*, **210**, 929
- Liu, R., Pooley, G., & Riley, J. M. 1992, *MNRAS*, **257**, 545
- Machalski, J., Chyzy, K. T., Stawarz, L., & Koziel, D. 2007, *A&A*, **462**, 43
- Mack, K.-H., Klein, U., O'Dea, C. P., Willis, A. G., & Saripalli, L. 1998, *A&A*, **329**, 431
- Miley, G. K. 1980, *ARA&A*, **18**, 165
- Murgia, M., Fanti, C., Fanti, R., Gregorini, L., Klein, U., Mack, K.-H., & Vigotti, M. 1999, *A&A*, **345**, 769
- Myers, S. T., & Spangler, S. R. 1985, *ApJ*, **291**, 52
- Napier, P. J., Thompson, A. R., & Ekers, R. D. 1983, *IEEE Proc.*, **71**, 1295
- O'Dea, C., Daly, R., Freeman, K. A., Kharb, P., & Baum, S. 2009, *A&A*, **494**, 471
- Owczarek, J. A. 1964, *Fundamentals of Gas Dynamics* (Scranton: International Textbook Co.)
- Parma, P., Murgia, M., Morganti, R., Capetti, A., de Ruiter, H. R., & Fanti, R. 1999, *A&A*, **344**, 7
- Scheuer, P. A. G. 1982, in *IAU Symp. 97, Extragalactic Radio Sources*, ed. D. S. Heeschen & C. M. Wade (Dordrecht: Kluwer), 163
- Tregillis, I. L., Jones, T. W., & Ryu, D. 2004, *ApJ*, **601**, 778